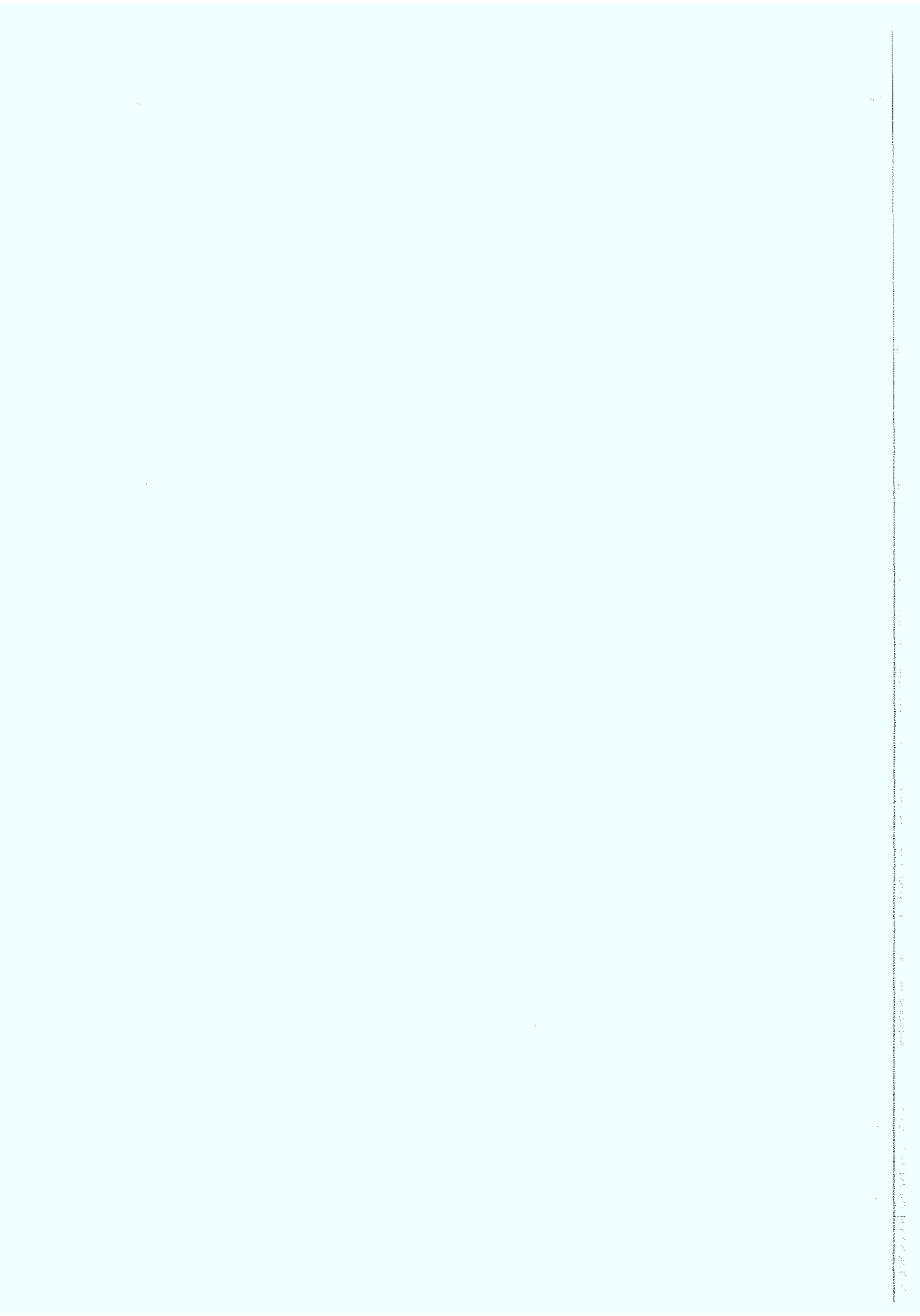
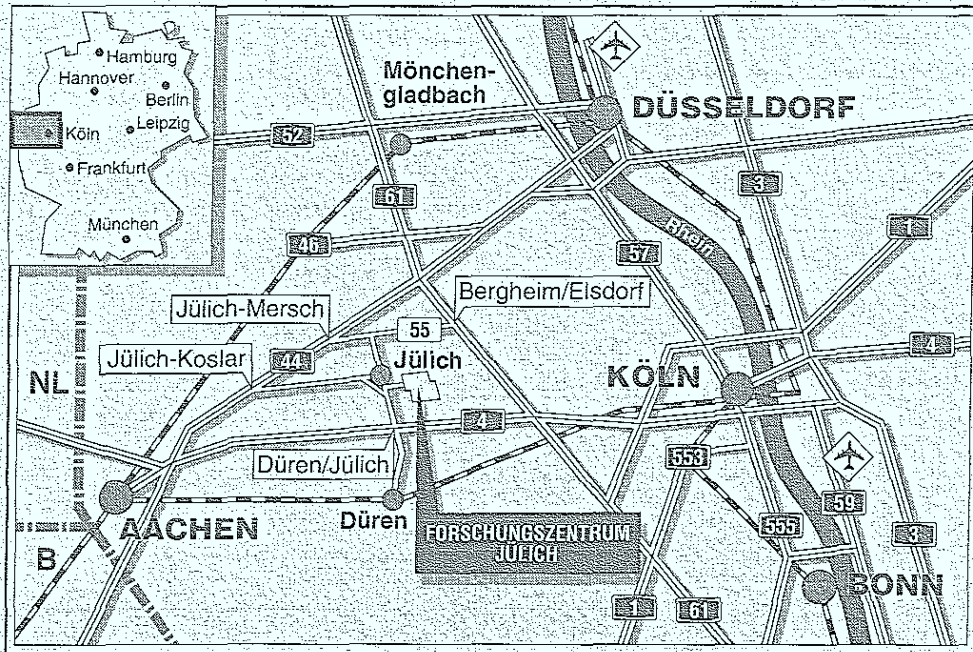


Institut für Festkörperforschung

**Near Infrared Microscopy a simple
but effective technique to analyze
microdefects in GaAs**

K. Sonnenberg und A. Altmann





Berichte des Forschungszentrums Jülich ; 2939

ISSN 0944-2952

Institut für Festkörperforschung Jül-2939

Zu beziehen durch : Forschungszentrum Jülich GmbH · Zentralbibliothek
D-52425 Jülich · Bundesrepublik Deutschland
Telefon : 024 61 / 61 - 61 02 · Telefax : 024 61 / 61 - 61 03 · Telex : 8 33 556-70 kfa d

Handwritten text, likely bleed-through from the reverse side of the page. The text is mostly illegible due to fading and bleed-through, but some words like "The" and "and" are visible.

Near Infrared Microscopy a simple but effective technique to analyze microdefects in GaAs

K. Sonnenberg und A. Altmann

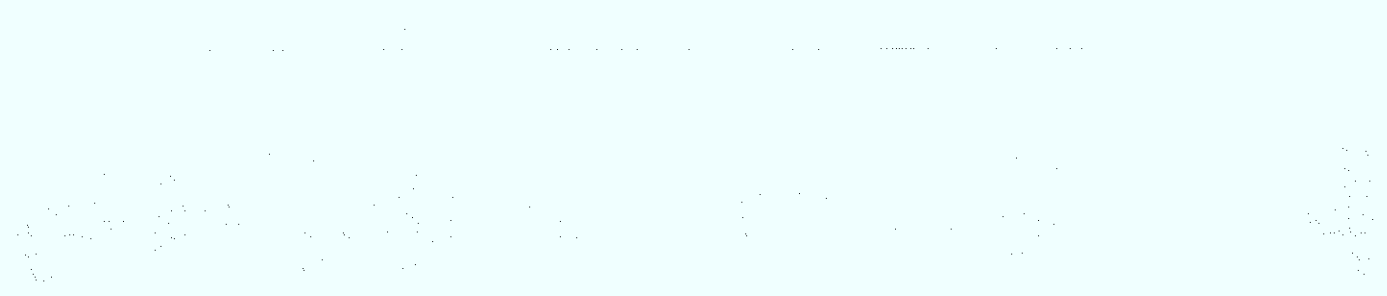


Figure 4: A graph showing the relationship between the number of nodes and the number of edges in a tree structure. The x-axis is labeled "Number of nodes" and the y-axis is labeled "Number of edges". The data points form a straight line passing through the origin, indicating a linear relationship where the number of edges is equal to the number of nodes minus one.

10/10/2023

Acknowledgement

One of the authors (K.S.) is very grateful to Prof. A.F. Witt for introducing him to NIR-microscopy. We thank Dr. J.L. Weyher for the good and productive cooperation during several month, Dr. P. Franzosi for performing x-ray-topography and Dr. O. Pätzold for the Ramanscattering measurement presented in the paper. We are also grateful to Prof. H. Wenzl for carefully reading of the manuscript.

Introduction

The purpose of this study is to investigate the effects of a new educational program on student performance. The program is designed to improve students' understanding of complex concepts through interactive learning methods. The study will compare the performance of students who participated in the program (experimental group) with those who did not (control group) over a period of six months. The data collected will be analyzed to determine if the program has a statistically significant impact on student learning outcomes.

1. Introduction
2. Experimental Methods
 - 2.1. Photoetching
 - 2.2. NIR-microscopy: Phase microscopy, Darkfield Technique, "Schlieren" microscopy, Polarisation microscopy, and Differential Interference Technique
 - 2.3. EBIC
3. Results and Discussion
 - 3.1. "Cottrell" atmosphere of dislocations in doped GaAs
 - 3.1.1. Interpretation of NIR-image contrast
 - 3.1.2. Interpretation of the difference in the refractive index between the "Cottrell" atmosphere and the surrounding matrix
 - 3.2. Application of phase microscopy
 - 3.2.1. Post growth annealing studies
 - 3.2.2. Glide processes during cooling of the crystals
 - 3.2.3. Growth striations:
 - (i) Contrast interpretation
 - (ii) Thermal annealing
 - 3.2.4. Te-doped GaAs
 - 3.3. Application of darkfield technique for undoped GaAs
 - 3.3.1. Dislocation structure in VB-crystals
 - (i) Configuration of dislocation lines
 - (ii) Dislocation cell structure
 - (iii) Lineage in VB-crystals
 - (iv) "Pseudo"-decoration precipitates
 - (v) Other decoration features
 - 3.3.2. Dislocation structure on twin-boundaries
 - 3.3.3. Influence of stoichiometry on As-precipitation
 - 3.4. Application of polarized light
 - 3.4.1. Birefringence contrast between crossed polarizers
 - 3.4.2. Differential interference contrast (DIC)-transmission mode

4. Conclusion

References

1. Introduction

The main structural microdefects in GaAs are point defects (native defects, dopants), dislocations, precipitates, and inhomogeneities of point defects. Microdefects are important because they directly affect the single crystal yield during the growth process and the properties of the crystal after growth. It has been shown [1] that the transition from single to polycrystalline growth is primarily caused by a local increase in the dislocation density near the crystal surface. When single GaAs crystals are used as substrate material for electronic devices microdefects significantly influence the device performance. Dislocations, for example, have a detrimental influence on the lifetime of minority carriers and the carriers mean free path; they degrade semiconductor lasers due to their role as nonradiative recombination centers [2]. It has also been shown that inhomogeneities in the substrate material are linked to fluctuation in the threshold voltage, V_{th} of field effect transistors, thus impeding the exploitation of large scale integrated circuits (LSI). Understanding the mechanism which are causing the formation of microdefects will help to find ways to reduce their number or to minimize their detrimental influence.

Several mechanisms for the nucleation of dislocations have been discussed in the literature. Because the entropy term of a dislocation is so much smaller than its energy, dislocations do not exist in thermodynamic equilibrium. The following heterogeneous nucleation mechanisms are possible:

- Surface damage such as scratches have been identified.
- Surface roughness which may form near the growth front due to loss of arsenic by evaporation have not been clearly identified but could be a major source for dislocations and could also play a role for initiating polycrystalline growth [3, 4].
- Chemical inhomogeneities resulting in the formation of misfit dislocation have been discussed as a possible reason for the formation of dislocation cells. Some evidence will be presented that this correlation is very unlikely.
- Second phase particles can generate dislocation by their volume misfit or by a differences in thermal expansion between particle and matrix [2].
- Agglomeration of point defects resulting in loop formation has also been discussed.

Although we know some possible nucleation mechanism for dislocation it is not clear which of them dominates during the growth of crystals.

The major effort in the present work was directed towards studying of inhomogeneities in the surrounding of dislocations due to their interaction with doping and native defects. Dislocation can

- act as nucleation sites for the formation of precipitates
- interact with doping and native defects to form Cottrellatmospheres and associated denuded zones
- react with native defects—As—interstitial or Ga—vacancies, respectively. As a result the dislocation perform a climbing step and Ga—vacancies or As—interstitials, respectively, are emitted. These reactions are driven by a substantial excess of arsenic

(probably $\gtrsim 5 \cdot 10^{18} \text{ cm}^{-3}$) present in most GaAs crystals. The emission of native defects through this mechanism seems to be responsible for the increase of EL-2 centers in the surrounding of dislocation [5].

Another source for inhomogeneities are growth striations the importance of which has not yet been fully recognized [6]. Inhomogeneities may also be due to denuded zones formed around large matrix precipitates as shown in the present work.

A possible way to minimize the effect of microdefects are post growth annealing treatments [8], which in the past, however, were mainly based on empirical knowledge. Scientifically based recipes for controlled annealing can only be obtained through an understanding of the defect reactions which are responsible for the generation of inhomogeneities. Annealing studies performed in the present work can help to understand the defect reactions by investigating their kinetics.

Microstructural studies have often been performed by

- (i) Photoetching (DSL) = Dilute Sirtl in Light. The etching rate is determined by the local concentration of holes reflecting the concentration of doping and native defects. The concentration and influence of various defects is often not known making it difficult to obtain a clear cut interpretation of the etching results. The great advantage of this method is its ability to resolve small variation in the defect concentrations.
- (ii) EBIC [9] and Ramanscattering [10] measurement which allow to determine the net ionized doping concentration ($N_D - N_A$). Raman scattering is also able to identify As-precipitates which are close to the surface [see also 11, 12, 35, 46].

The results presented in this paper have been mainly obtained by IR-microscopy. Photoetching-, EBIC-, and Ramanscattering techniques have also been used. Due to the high transparency of GaAs in the infrared it is possible to resolve microdefects also inside a relative thick ($\lesssim 5 \text{ mm}$) sample in contrast to the other three methods which are surface sensitive techniques. The capability of infrared microscopy to study also microdefects in the bulk of the sample is particularly important for post growth annealing studies. A comparison of the annealing effect on individual microdefects is not possible in surface-near areas, since a high temperature anneal inevitably causes damage on the surface of GaAs-samples.

For a few studies TEM- and X-ray topography have been employed. Photo- and catholuminescence were not used for the present investigation of microdefects. Spectroscopically resolved low temperature PL and CL would be able to provide additional information, for example, about distribution of doping atoms on donor and acceptor sites.

In this paper we will show that IR-microscopy is a simple and effective technique to study microdefects in GaAs. Its potential has not been fully recognized in the past. Since the image contrast for IR-microscopy can be affected by several material properties, it is mandatory to perform a careful assessment whether absorption - or refraction effects are dominating. This will be discussed in detail in the first section by comparing images of identical sample areas taken with different contrast techniques: Bright field, phase contrast and "Schlieren" contrast.

After proving that changes in the refractive index are dominating the image contrast, we will show that these changes are due to variations in the free charge carrier concentration, which can be imaged best by phase microscopy.

In the next section four examples are presented applying phase microscopy to study inhomogeneities in doped GaAs which was grown by the Vertical Bridgman technique: annealing studies in Si-doped material, glide processes taking place during cool-down of the crystal after growth, growth striations and their thermal stability upon annealing providing information about the diffusion of Si and some observations for Te-doped material.

In the third section we will discuss some applications of IR-dark field technique. This method can be employed to resolve precipitates in GaAs. Since dislocations are often decorated with As-precipitates the method also reveals the dislocation structure. Different decoration pattern and the associated dislocation structure present in VB-crystals will be discussed. Evidence will be presented that dislocation cell structures as well as dislocation lineage must be attributed to polygonisation effects after growth. The appearance of many decoration patterns indicates the importance of dislocation climb in GaAs. We will then discuss the dislocation structure of twin boundaries and finally describe the influence of stoichiometry.

Making use of the strong elasto-optical properties of III-V compounds, dislocation in these material can also be imaged by using birefringence contrast between crossed polarizers. Theoretical aspects and experimental results of this method have been discussed in many papers (see ref. 11, 13-33). In spite of the large effort the contrast interpretation still remains controversial. We shall compare our experimental results with the different models and we will present, for the first time images of dislocations obtained by differential interference contrast in transmission mode.

2. Experimental Methods

The majority of GaAs-crystals analyzed in the present paper were grown by the VB-Bridgman technique using quartz crucibles. The typical growth rate was about 4 mm/h. Results of undoped semiinsulating as well as Si- and Te-doped GaAs will be discussed. The doping concentration varied between $5 \cdot 10^{16}$ and $2 \cdot 10^{18} \text{ cm}^{-3}$. For more details of crystal growth see ref. [1]. For analyzing crystals by photoetching and IR-transmission-microscopy samples were prepared by mechano-chemical polishing with PA-7 solution. For IR-microscopy samples were polished on both sides (see also ref. [34] for more details).

In the following the main analyzing techniques photoetching, IR-microscopy and EBIC employed in the present work will be briefly discussed.

2.1 Photoetching

Photoetching is a simple and quick method to study microdefects in GaAs [for details see 7, 85]. It is, however, an indirect method because it reveals etch features which are due to the presence of defects but the defects themselves remain invisible. As a result and because photoetching is only a qualitative method the interpretation of etch features is not always straightforward. Some typical etch features discussed in the present paper are illustrated in figure 1.

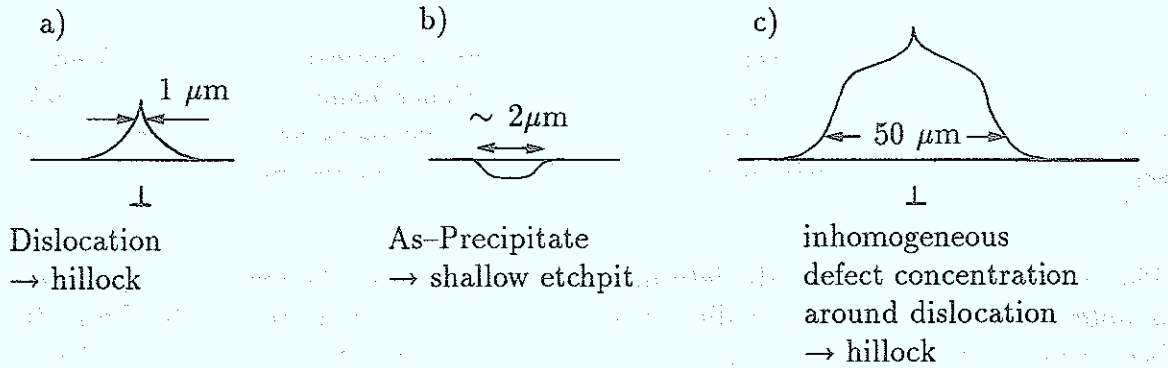


Fig. 1: Surface profiles of GaAs after photoetching of various defects.

Independent of the electrical properties of GaAs dislocations emerging at the sample surface are associated with a small hillock $\approx 1 \mu\text{m}$ wide and $\approx 200 \text{ nm}$ high. As-precipitates form shallow pits; their depth is related to the size of the precipitate, whereas the width is mainly determined by the duration of the etching process. Defect inhomogeneities around dislocation in Si-doped GaAs result in an increased etching rate as shown in figure 1c.

In the present paper we will discuss photoetching employing the Redox-etching system $\text{CrO}_3\text{-HF-H}_2\text{O}$, which is usually called DSL-etching i.e. Diluted Sirtl-like etchant used with light. Etching of semiconductors is electrochemical in nature because carriers (particular holes) are involved in the dissolution process. The availability of carriers at the semiconductor surface depends on the electronic structure of the material. In n-type semiconductors the bands bend upwards during electroless etching as illustrated in figure 2. During etching without illumination the holes are available from

- (i) GaAs: minority carriers separated by the electric field and concentrated close to the surface within the depletion layer width, W_{sc} and
- (ii) etching solution as a result of reduction of Cr^{VI} species according to the reaction

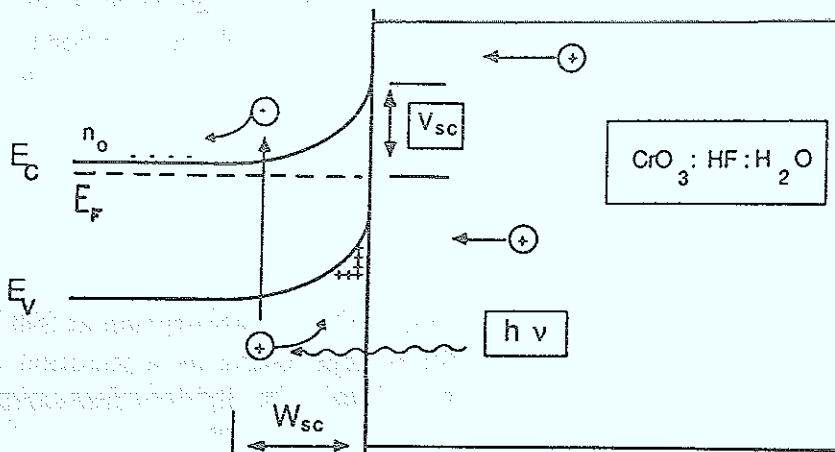
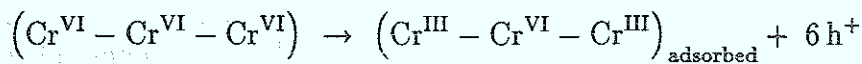
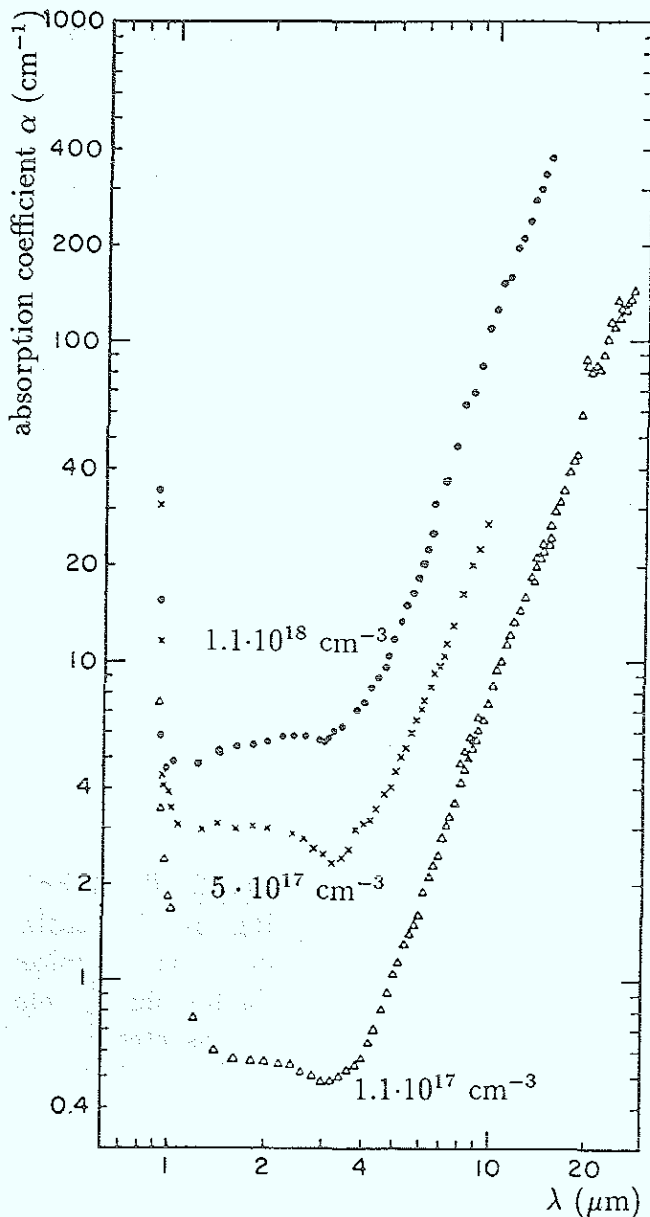


Fig. 2: Band bending at the surface of n-type semiconductor during electroless etching with $\text{CrO}_3\text{:HF:H}_2\text{O}$.

The passivating adsorbed layer containing chromium complexes is removed from the surface by HF, while holes are injected into the valence band to rupture the GaAs-bonds. When the surface is illuminated electron-hole pairs are generated and are separated in n-type material within the depletion layer increasing the overall rate of etching.

The selective etching is mainly determined by the width of the depletion layer which is different in the vicinity of a dislocation (see figure 1c) as compared to the matrix because of an inhomogeneous distribution of the doping concentration $N_D - N_A$. In semiinsulating material the variation of etch rates, especially when light is used, is attributed to the inhomogeneous distribution of the deep recombination centers. The nature of these defects is still not known in many cases. Increasing the concentration of recombination centers results in a decrease of holes for the surface reaction and decreases the etching rate.



2.2 Near Infrared (NIR) Microscopy

Because GaAs is highly transparent in the near infrared range even for highly doped material (see figure 3: $1 < \lambda < 4 \mu\text{m}$; $\alpha \leq 5 \text{ cm}^{-1}$) it appeared very interesting to employ NIR-microscopy for studying the microstructure of this material.

The absorption mechanism in the near infrared has been identified by E. Haga and K. Kimura [37] as due to intraconduction band transitions, i.e. to electron transition from the conduction band minimum (Γ_1) to higher valleys with different values in k-space. The absorption coefficient in the near infrared (plateau region) as a function of the free charge carrier concentration, \bar{n} can be described by

$$\alpha \approx 6 \cdot 10^{-18} \bar{n} [\text{cm}^{-1}] \quad (1)$$

Fig. 3: Optical absorption at 296 K for n-type GaAs as a function of wave length for different free carrier concentrations [36].

In contrast to TEM studies the high transparency in the infrared allows to screen very thick samples (≈ 5 mm). It is very convenient that commercially available microscopes can be used because their standard optics is sufficiently transparent in the near infrared. Also – as shown in figure 4 – CCD-TV-cameras are available which exhibit a sufficient sensitivity at least for the smaller wavelengths of the near infrared.

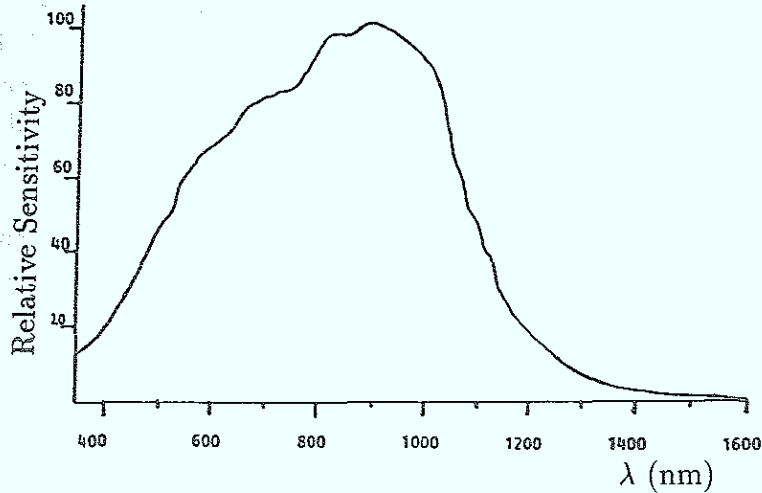


Fig. 4: Relative sensitivity of the TV-camera (KAPPA CF 100X) as a function of the wave length.

The high transparency of GaAs on the other hand is disadvantageous for imaging microstructural defects due to inhomogeneities in the absorption coefficient. If they are due to a variation in the free carrier concentration we can estimate the absorption contrast for bright field image conditions from equation (1).

$$K = \frac{I_O - I_S}{I_O + I_S} = \frac{e^{-\alpha_O d} - e^{-\alpha_S d}}{e^{-\alpha_O d} + e^{-\alpha_S d}} \approx -\frac{(\alpha_O - \alpha_S) \cdot d}{2} = \frac{-\Delta\alpha \cdot d}{2} = -3 \cdot 10^{-8} \cdot \Delta\bar{n} \cdot d \quad (2)$$

where I_O , I_S is the intensity of the object (O) and the surroundings (S), respectively and d is the thickness of the object with an absorption coefficient, α_O different from that, α_S of the surrounding. Assuming that the object becomes visible for $K \gtrsim 0.1$ and that d is roughly determined the focal depth of the microscope objective ($\approx 40 \mu\text{m}$) a bright field image can only resolve variations in the free carrier concentration of about 10^{19} cm^{-3} . Smaller variation of \bar{n} may be detectable, if d is not limited by the focal depth but rather by the thickness of the sample, e.g. by using diffused light illumination which, however is not possible for a microscope. Similar conditions have been used e.g. to determine the EL2-distribution which is correlated with the dislocation cell structure [38] or to measure the concentration of EL2 in the vicinity of single dislocations [39]¹ To draw quantitative conclusions from these studies it is, however, necessary that the defect structure is not varying over the thickness (\approx typically 1 mm) of the sample. Such a condition can hardly be fulfilled, particularly if the cell structure of a wafer is investigated. D.J. Carlson and A.F. Witt [40] measured the variations of the absorption coefficient due to growth striations. In this case the microstructure is homogeneous

¹Absorption due to native defects also gives rise to rather small absorption coefficients, i.e. one relies on large d -values for detecting small variation in defect concentrations.

and d was taken as the thickness of the sample. The imaging conditions in this case however, require d to be rather limited by roughly the focal depth of the microscope.

In addition to these difficulties the quantitative interpretation of bright field images (BF) is further complicated by the fact, that their contrast is not only determined by absorption effects but it can also be influenced (see next chapter) by variations in the refractive index n , as well as by gradients in n . This means that quantitative conclusions must be based on a very careful assessment; in particular, it is necessary to find out which of the above properties is responsible for the image contrast. This information cannot be obtained from BF-images only. An assessment will be presented in the next chapter for the inhomogeneous distribution of defects around dislocations in materials, most of which have been grown by the Vertical Bridgman technique [1]. This assessment will be based on a comparison of identical sample areas imaged by different contrast techniques: bright field, phase microscopy and "Schlieren" contrast (central dark ground contrast). Schlieren contrast microscopes are not commercially available. Details how to built this type of microscope will be discussed in the next chapter. The potential of phase microscopy for microstructural studies has not been fully recognized. Since most results in the present work will be based on this technique we shall explain it in more detail.

Phase microscopy:

The principle of phase microscopy is shown in figure 5 and 6.

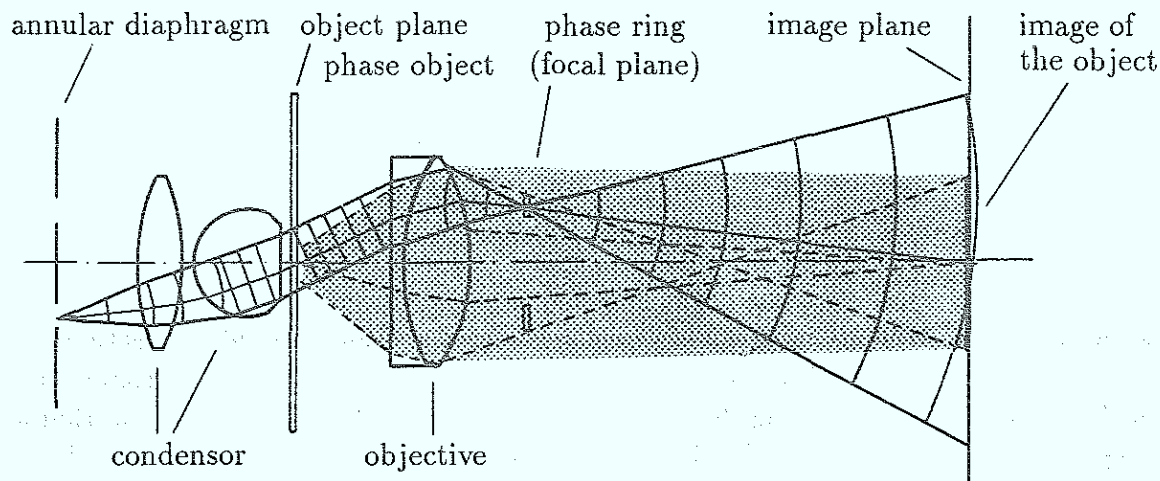


Fig. 5: Main components of a phase microscope: annular condenser diaphragm, condenser, phase object, objective, diffraction plate with phase ring located in the focal plane of the objective.

In this chapter we will only discuss the so-called "ideal Zernike" method [41, 42]. To understand the results presented in chapter 3, however, effects of the "Real Zernike"-method (see section 3.1.1) must be taken into account. The present discussion will be further restricted to object specimens which are characterized by variations in the refractive index and which exhibit a homogeneous absorption. The light wave emerging from the annular condenser diaphragm may be considered essentially as a plane wave when entering the object specimen. The object (zone of the specimen which exhibits a different refractive index) forms an obstacle in the path of the incident wave as a result

of which the wave is diffracted. The out-going wave can be considered as two waves, one undeviated (vector \vec{a}_1) and the other deviated (vector \vec{a}_2). Both add up to a wave which is slightly phase shifted (vector \vec{a}_0) by the object. The undeviated wave drawn as solid lines in figure 6a is focussed in the focal plane of the objective and spreads out

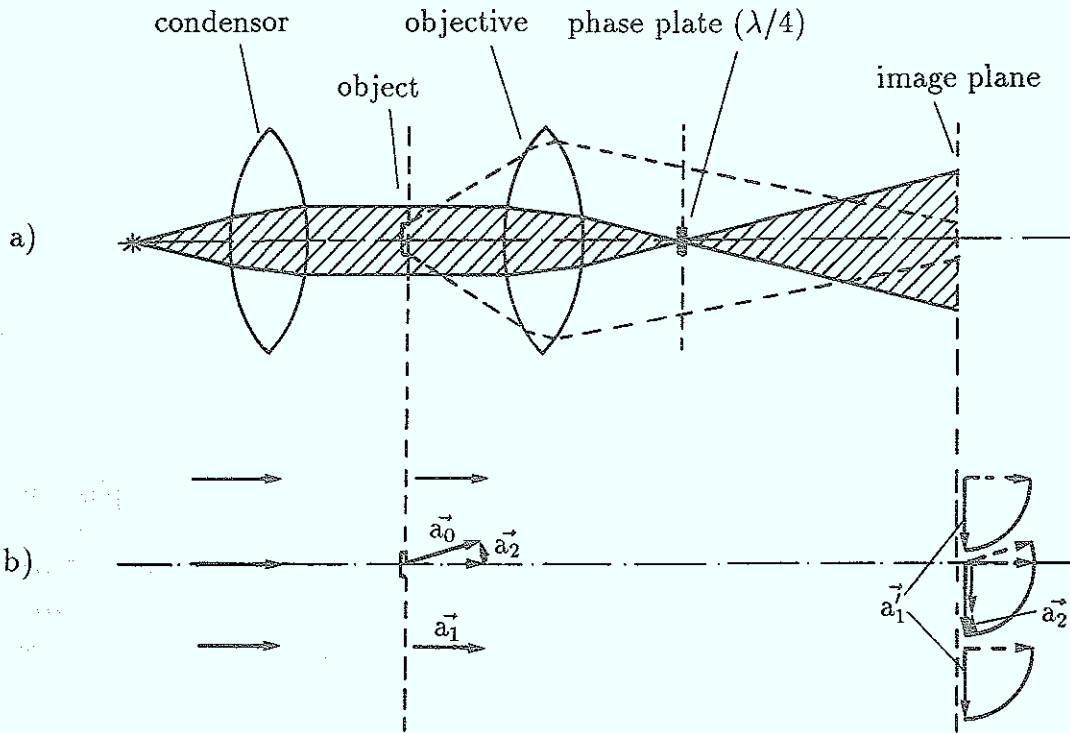


Fig. 6: a) Schematic diagram for phase contrast technique; b) Transformation of a phase shift φ into a variation of the wave amplitude.

over the image plane. It is phase shifted by 90° by passing through the phase plate located in the focal plane of the objective: The deviated wave is focussed in the image plane, but extends over the whole focal plane of the objective which means that it practically remains unaffected by the phase-ring. For small phase-shifts φ , \vec{a}'_1 and \vec{a}'_2 are almost parallel. The superposition of the deviated and undeviated wave therefore results in a change of the amplitude, which in turn creates the visible contrast. As indicated in figure 6b for a pos. φ (neg. φ) the object appears bright-(dark) on a darker (brighter) background if the phase-shift of the undeviated wave by the phase ring is $+90^\circ$ (-90°). The latter case is defined as "Positive Phase Contrast" since an object which is optically less dense (denser) than the surrounding material appears bright (dark).

In order to increase the image contrast most phase microscopes are using a phase ring which absorbs part of the undeviated light; this can be seen in figure 6b which shows that the relative change of the undeviated wave $|\vec{a}'_1|$ by superimposing $|\vec{a}_2|$ would be larger for higher absorption by the phase ring. If $|\vec{a}'_1| = t|\vec{a}_1|$ the intensity of the object and the surrounding can be easily calculated [41]. For positive phase contrast we obtain (see also figure 6)

$$I_{\text{Object}} = 2 + t^2 - 2(\cos \varphi + t \cdot \sin \varphi) \quad (3)$$

$$I_{\text{Surrounding}} = t^2 \quad (4)$$

$$K = \frac{I_o - I_s}{I_o + I_s} = \frac{1 - (\cos \varphi + t \sin \varphi)}{(\cos \varphi + t \sin \varphi) + 1 + t^2} \quad (5)$$

for small phase shifts φ

$$I_{\text{Object}} = t^2 - 2\varphi t + \dots \quad (6)$$

$$K = -\frac{\varphi}{t} \quad (7)$$

the contrast is proportional to the phase shift (in a first order approximation) and increases with the absorption of the phase ring.

Schlieren microscopy:

A “Schlieren” microscopy has been built by increasing the absorption of the phase ring till $t = 0$; i.e. to block off all undeviated light. Such a microscope ought to be particularly sensitive to gradients in n in the object specimen, since as indicated in figure 7 refracted light is not screened off by the opaque phase ring. Another possibility to generate an image contrast in a “Schlieren” microscope is due to light which is diffracted by small phase objects which would also be visible under phase contrast conditions ($t \neq 0$). This intensity in the “Schlieren” microscope can be calculated from equation (3) and (6), respectively for $t = 0$ [43]

$$I_{\text{Obj}} = 1 - \cos \varphi \quad (3a)$$

or for small phase shifts

$$I_{\text{Obj}} = \varphi^2 + \dots \quad (6a)$$

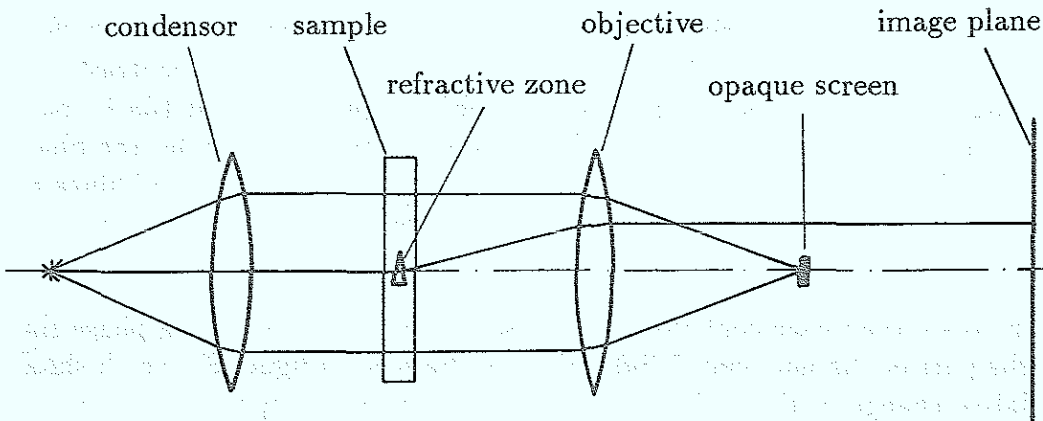


Fig. 7: Schematic diagram of a “Schlieren” microscope.

In contrast to phase microscopy which is sensitive to the first order of the phase shift (i.e. it can determine the sign of Δn ; compare Te and Si-doped GaAs) “Schlieren” microscopy can only detect quadratic term in φ and it is also less sensitive (see discussion in chapter 3).

Dark Field Technique:

Compared to phase microscopy the dark field technique has been employed much more widely for microstructural studies in GaAs. This is due to the fact that as grown material (without any post growth annealing) contains arsenic precipitates which become visible by this technique imaging the scattered light only. Since these precipitates are formed usually along dislocations (decoration precipitates [44, 45]) it is also possible to study the structure of these decorated dislocations. Since the majority of the precipitates are much smaller ($\approx 0.1 \mu\text{m}$) than the wavelength of the infrared light ($\approx 1 \mu\text{m}$) the scattered intensity can be described by Rayleigh theory

$$I_{\text{scattered}} \sim \frac{1}{\lambda^4} \bar{\alpha}^2 V^2 \sin^2 \Theta \quad (\text{Fig.8}); \quad \alpha = \frac{3\pi}{4} \frac{n^2 - 1}{n^2 + 1} \quad (8)$$

where V is the volume of the precipitate and Θ the angle between the electric field, \vec{E} of the polarized light and the scattering direction [46].

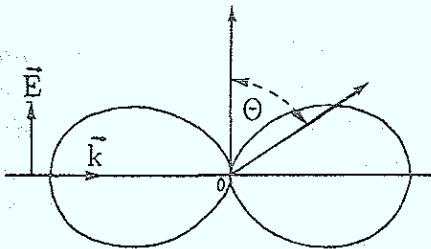


Fig. 8: Rayleigh intensity as a function of Θ .

Most groups e.g. [47], [48] are using a dark field illumination method which is known as the "Ultramikroskop" (see e.g. [49]) as shown in figure 9. The image is generated by

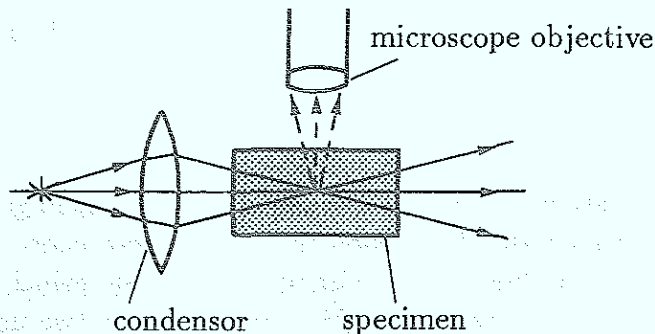


Fig. 9: Schematic diagram of the Ultramikroskop.

light which is scattered by the precipitates under $\approx 90^\circ$. To obtain a sufficient intensity the electric field of the polarized light must be perpendicular to the scattering direction (see equation (8)). Since lasers are usually employed for illuminating only a very small area of the sample, the image must be formed by a 2-dimensional scan of the laser across the sample. This technique is therefore known as Laser scanning tomography in the literature [47]. The image must be processed by a computer which also synchronizes the movement of a x-y-table necessary for the scanning of the laser. In the present work we are employing a much simpler conventional illumination technique as indicated in figure 10. A sample area corresponding to the field of view is illuminated by a 100 W light source through an annular diaphragm. The numerical aperture of the condenser and the objective are adjusted so that no direct light enters the microscope. Since the illuminated area covers the field of view an instantaneous image can be achieved without computer processing. In contrast to LST which requires a specially prepared surface

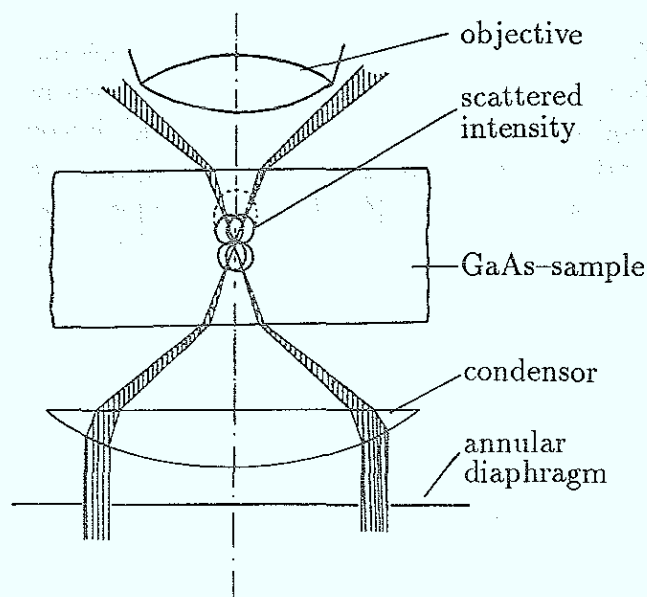


Fig. 10: Schematic diagram for a conventional dark field illumination.

for the illumination under 90° , wafers polished on both sides can be investigated in a nondestructive way by the present method. For investigating smaller size precipitates LST, however is superior because for the standard darkfield illumination dust and surface defects contribute considerably to an undesirable background illumination against which the defects to be studied are seen. Preliminary TEM-studies measuring the size of small matrix precipitates in GaAs [50] indicate that precipitates as small as 20 nm can be resolved by LST. The resolution of the present method is currently being investigated. Preliminary results indicate a value of ≈ 200 nm.

Note: Most of the dark field images presented in this paper show inverted (by electronic means of the CCD-camera) contrast, i.e. precipitates appear as black dots on a bright background. It was found that this helps improving the visibility of smaller precipitates.

Polarisation Microscopy

Dislocations become visible in a polarisation microscope because their stress field generates an optically anisotropic zone around the dislocation in an elsewhere isotropic crystal. For crossed polarizers this results in birefringence images. The basic principle of this method is illustrated in figure 11. The light wave, \vec{M} is split into the two normal modes M_1, M_2 for which the optical path is different in the anisotropic material. Because of the phase difference, θ developing between the two modes which interfere after passing through the analyzer, the intensity in the image plane is not zero but depends on the phase difference θ and the orientation of optical axis of the anisotropic material. The intensity has a maximum at $\varphi = 45^\circ$.

Differential interference contrast, DIC: (Nomarsky-technique)

This technique is usually employed to image surface reliefs (e.g. photoetched surface) in reflection mode. For transparent samples the method, however can also be used for transmitted light as illustrated in figure 12.

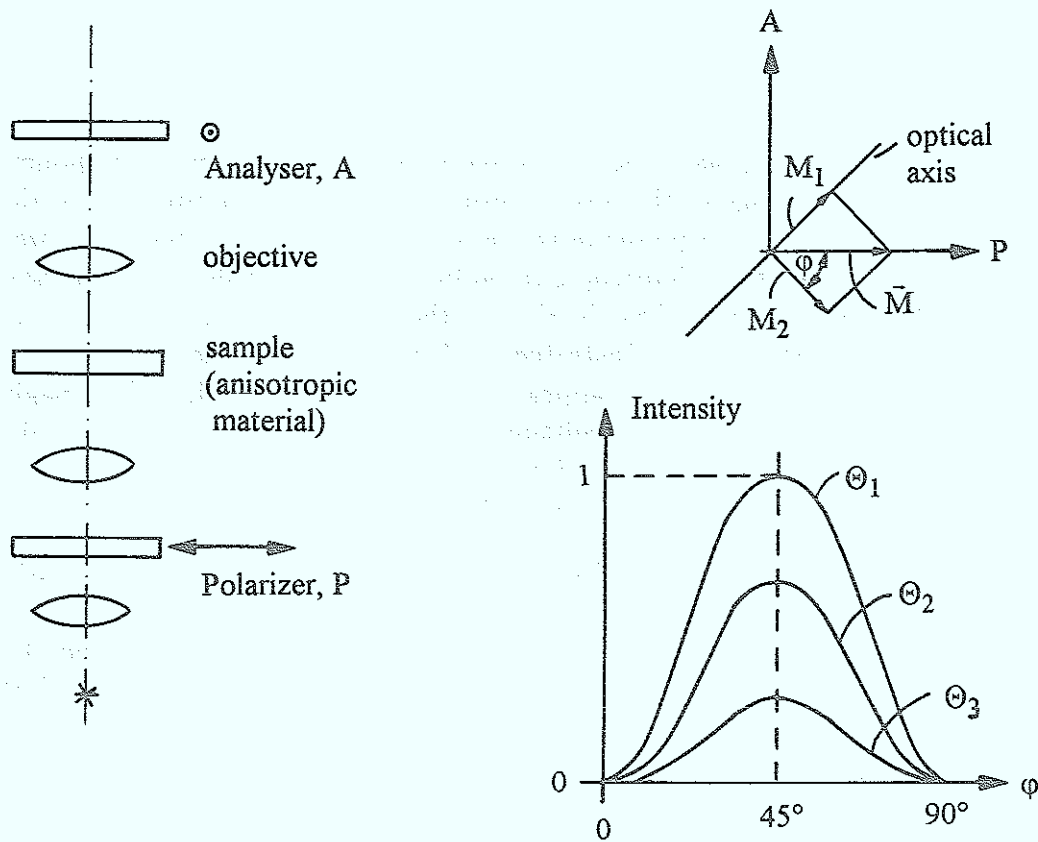


Fig. 11: Illustration of polarization microscopy (polarizer and analyser are polarizing filters with an efficiency of $\lesssim 10^{-4}$ for near IR-light).

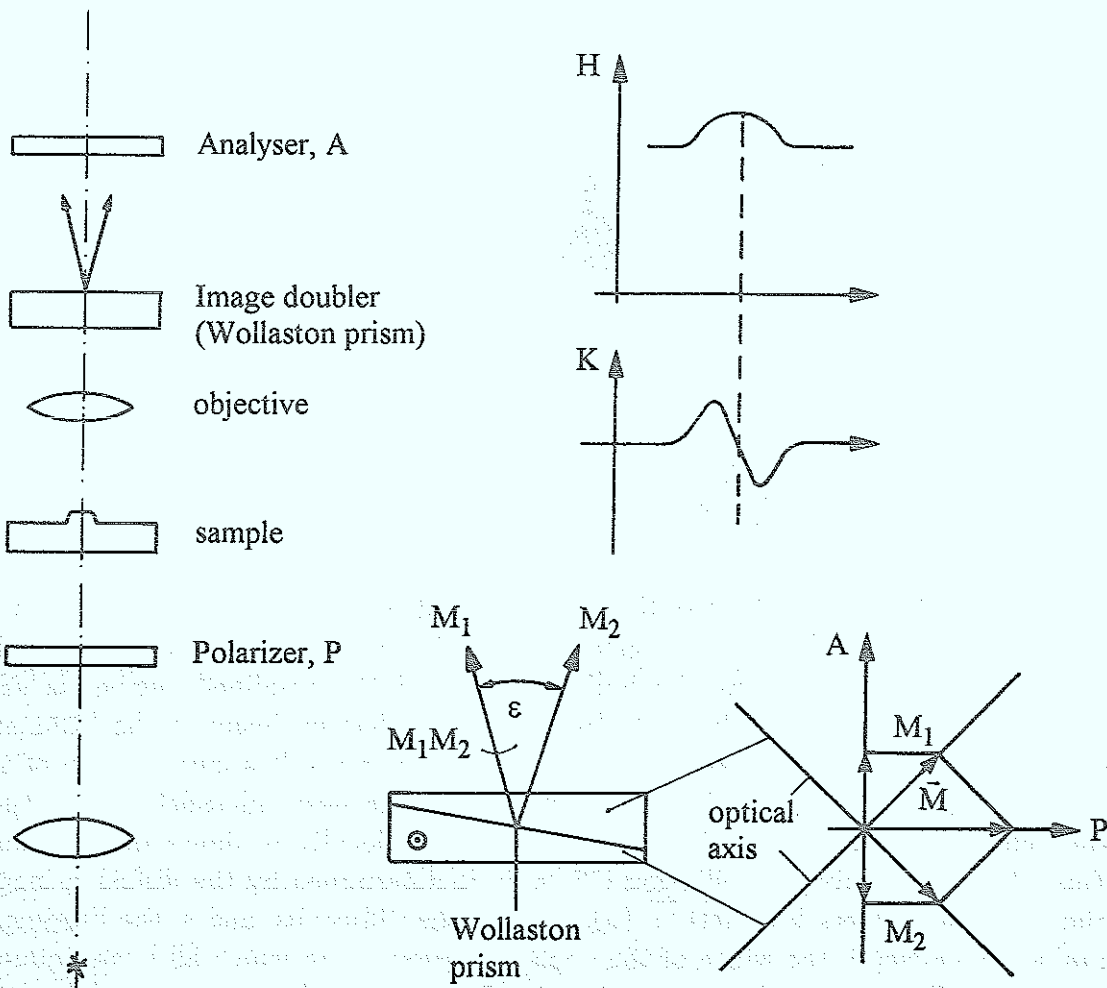


Fig. 12: Illustration of a DIC-microscope for transmission mode ($H = \text{height}$)

The DIC method employs a polarisation microscope with an additional component, which generates a double image of the object. Both images are superimposed so that light waves emitted from adjacent points of the object interfere. The distance between the points is of the order of the microscopic resolution. The phase difference between the two waves is therefore determined by the slope of the surface profile, i.e. the contrast becomes proportional to $\text{grad } H$ as illustrated in figure 12. This results in a light-shadow effect creating a 3-dimensional appearance of the surface relief. For imaging the surface of the sample the DIC-transmitting mode has no advantage compared to the reflecting mode. It could, however be important to reveal, e.g. variations of the refractive index, n within the crystal. An example will be discussed in section 3.4.2.

The image doubling is usually achieved by a so-called Wollaston prism which consists of two wedge shaped prisms made out of crystalline quartz. The optical axis of the two prisms are oriented perpendicular to each other. Polarized light with a 45° orientation to the optical axis is split into two waves with equal intensity. After passing through the Wollaston prisma the two waves propagate in slightly (ϵ) different direction generating a double image beyond the analyzer.

2.3 The electron beam induced current method (EBIC)

The method is widely used to image surface near microdefects of semiconductors by the scanning electron microscope, SEM [51, 52]. Figure 13 schematically shows the usual arrangement for EBIC observation in the SEM, when charge collection is performed

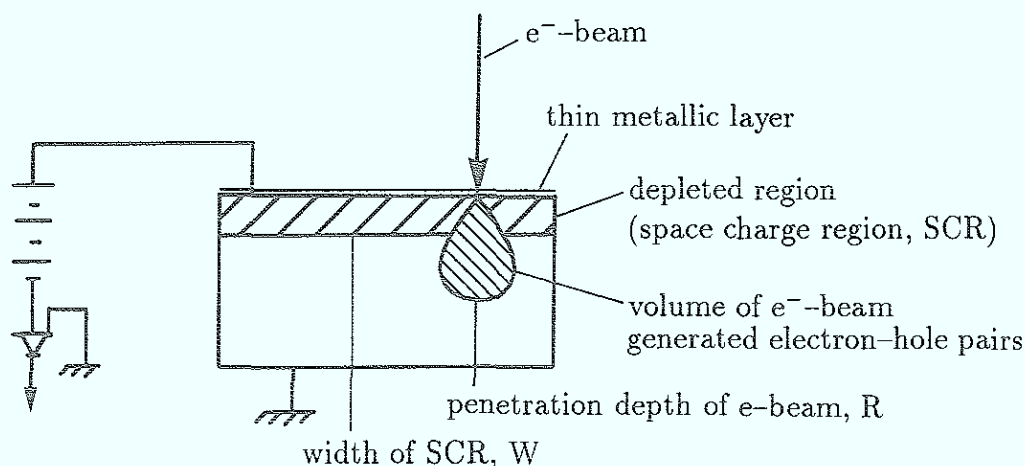


Fig. 13: Schematic diagram of the EBIC-method.

by a Schottky diode. The electron beam of the SEM penetrates the metallic layer of the Schottky diode and generates electron hole pairs up to a depth, R . These pairs are separated and collected by the built-in field and the amplified current is used to modulate the intensity of the SEM-monitor. The electron beam of the SEM and the monitor are performing a synchronized scan and as a result a current map of the semiconducting sample is obtained imaging the surface near microdefect structure. If the defect increases the carrier recombination rate locally it shows up as a dark feature. More generally the collection efficiency is determined by the diffusion length of the minority carriers $L = \sqrt{D \cdot \tau}$ (where D is the diffusivity and τ the lifetime of the minority carriers), the width of the depleted region, W in which all beam induced carriers are collected and the penetration depth, R of the electron beam. Electron-hole pairs which are generated outside the depleted region are not collected through

the electric field but must diffuse back to the Schottky barrier to contribute to the monitor signal. The width of the depleted region is given by

$$W^2 = \frac{2 \epsilon (V_o - V_b)}{e (N_D - N_A)} \quad (9)$$

where ϵ is the dielectric constant of the semiconductor, V_o the built in voltage, V_b the applied bias voltage and $N_D - N_A$ the net ionized impurity concentration.

The efficiency for the current can be calculated as a function of the e^- beam energy (which determines R), the diffusion length L and the width of the depletion region. Two examples are given in figure 14. By measuring the efficiency as a function of the e^- beam energy and comparing the results with calculated values in figure 14 the diffusion length and the depletion zone width can be determined. Equation (9) then allows to calculate the free carrier concentration $N_D - N_A$.

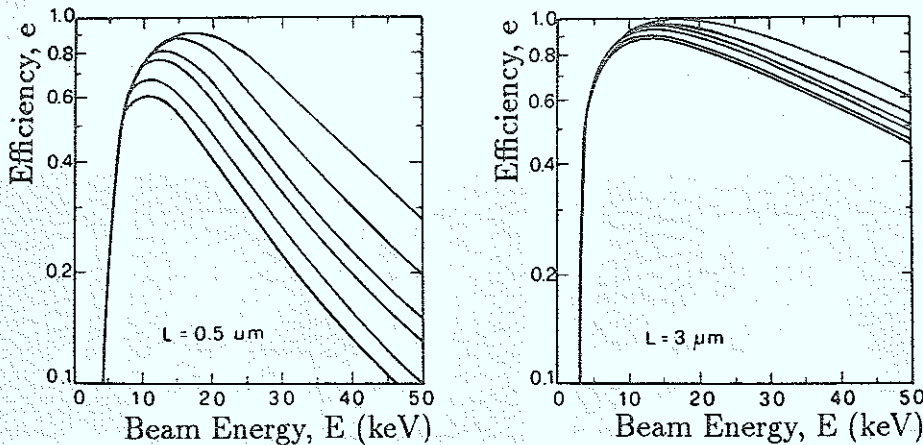


Fig. 14: EBIC efficiency dependence on the e^- beam energy, diffusion length L and the width of the depletion zone.

3. Results and Discussion

3.1 "Cottrell" atmosphere of Dislocations in Doped Material

In this section we will first present experiments which show that the NIR-image contrast of "Cottrell" atmospheres in doped material is mainly caused by the fact that the refractive index close to the dislocation is different from that in the surrounding material. We will then discuss evidence for a model in which this difference in the refractive index is attributed to a change in the free charge carrier concentration and we will show that the experimental results can be described by this model.

3.1.1 Interpretation of the NIR-image contrast:

Studying n-type doped GaAs with photoetching, [53] photoluminescence-[53], EBIC-[9] and Ramanscattering-[10] zones around dislocations extending up to a distance of about $100 \mu\text{m}$ have been found which exhibit a different etching rate, photoluminescence yield, EBIC-Current and a Ramanshift of phonon-coupled plasmon modes. Since the formation of these zones in doped samples have been attributed to the interaction of impurities with the dislocation they are usually associated [53, 9] with the term

Cottrellatmosphere. Although it will be shown in section 3.2 that the term Cottrellatmosphere is probably misleading in the present case, we will use it nevertheless in the following discussion for the sake of simplicity².

Figure 15 pictures such a “Cottrell” atmosphere after photoetching; the surface profile around the dislocation is raised since the etching rate is decreased because the width

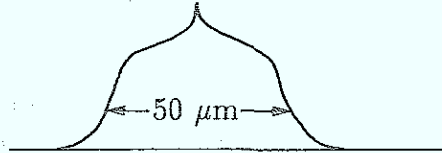


Fig. 15: Surface profile around a dislocation after photoetching of Si-doped GaAs.

of the space charge region $W \sim \frac{1}{\sqrt{N_D - N_A}}$ is smaller in this zone. In the present work it was found that “Cottrell” atmospheres can also be observed by NIR-microscopy.

An example for two different areas of a Te-doped material is shown in figure 16. The “Cottrell” atmosphere around the dislocation becomes visible because the optical properties differ from those in the surrounding material. In the following we will discuss the question whether the image contrast is caused by a variation in the absorption coefficient, α , in the refractive index, n or by gradients in the refractive index.

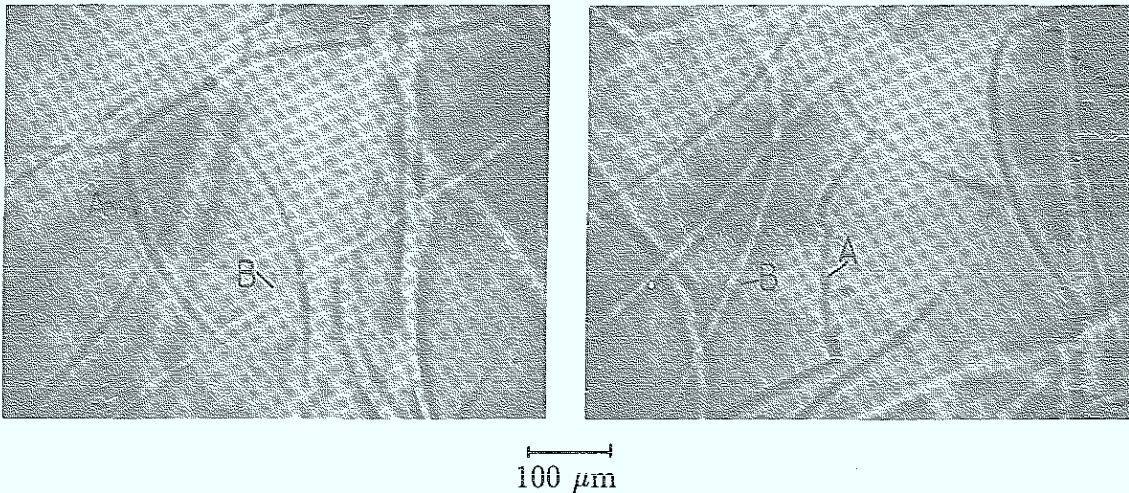


Fig. 16: Brightfield images of a Te-doped material grown by Vertical Bridgman-technique.

The fact that the images were taken under bright field condition points in the direction of the absorption coefficient. On the other hand the contrast of the “Cottrell” atmospheres is bright (B) in some and dark (A) in other cases. This result is presented again but more clearly in figure 17. The “Cottrell” atmosphere of a dislocation segment appears bright, a) (dark, c)) if the microscope is focussed on a plane which is closer to (further away from) the dislocation and focussing on the dislocation eliminates the contrast almost completely. Such a behaviour cannot be attributed to a variation of the absorption coefficient but must rather be correlated with the refractive index. As illustrated in figure 18 a “Cottrell” atmosphere with increased refractive

²To indicate those cases for which the term in fact is unreasonable it will be put between quotationmarks

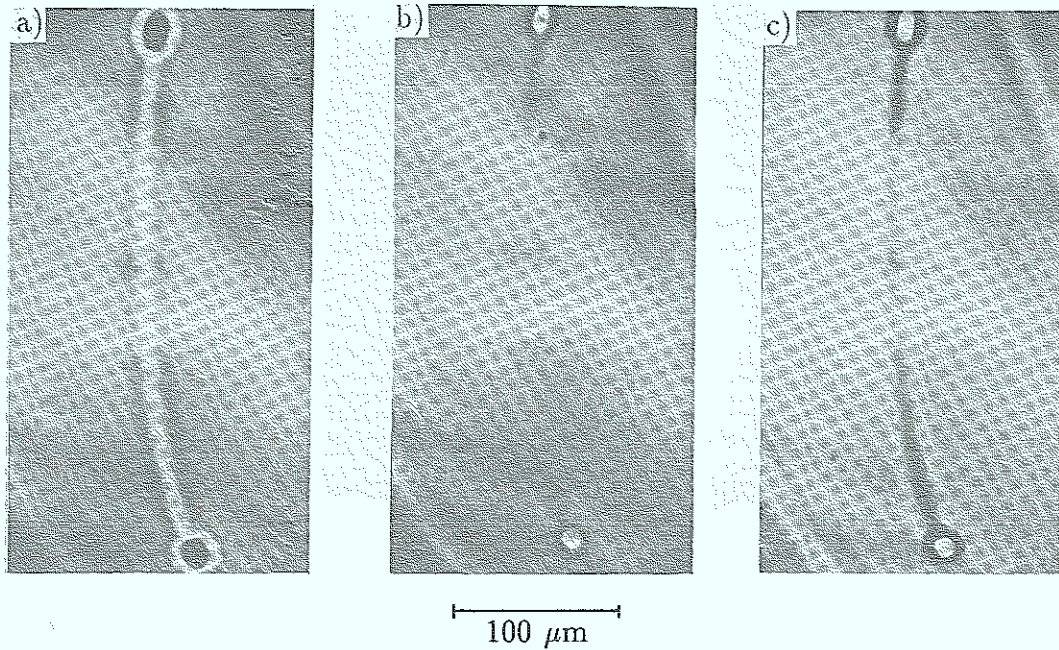


Fig. 17: "Cottrell" atmosphere of a dislocation segment close to the surface of a Te-doped sample. Figure a, b, c correspond to different focussing condition (a) closer, (b) in focus, (c) further away.

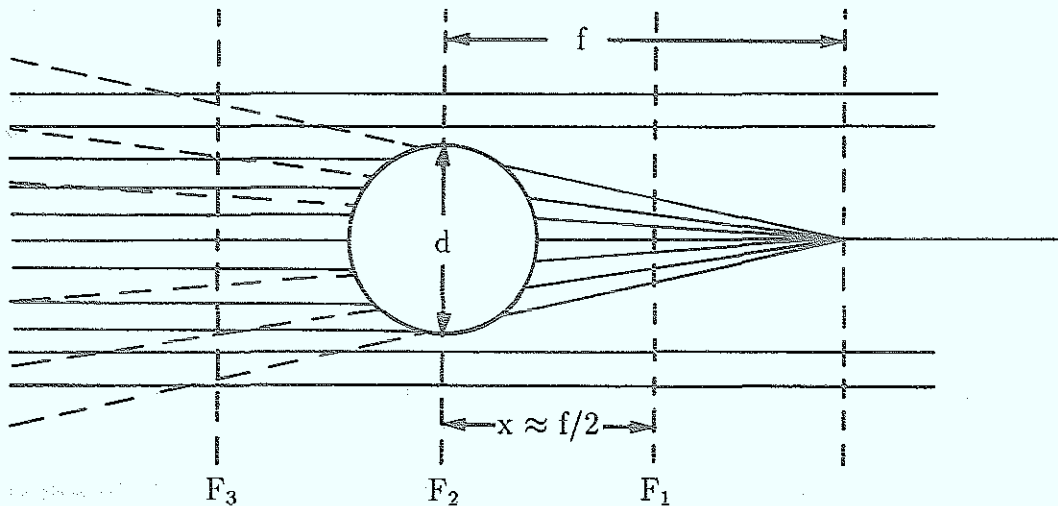


Fig. 18: Contrast generated by a converging lens under different focussing conditions.

index would basically generate the contrast of a converging cylindrical lens. Vanishing contrast when focussing on the centre of the lens (F_2 -plane) and bright (dark) center contrast with a dark (bright) halo for focussing on the F_1 (F_3)-planes. If the refractive index is decreased in the "Cottrell" atmosphere the contrast would be reversed for the same focussing conditions. This can be observed for Si-doped material as shown in figure 19 indicating that for Si-doped material, n is smaller in "Cottrell" atmosphere.

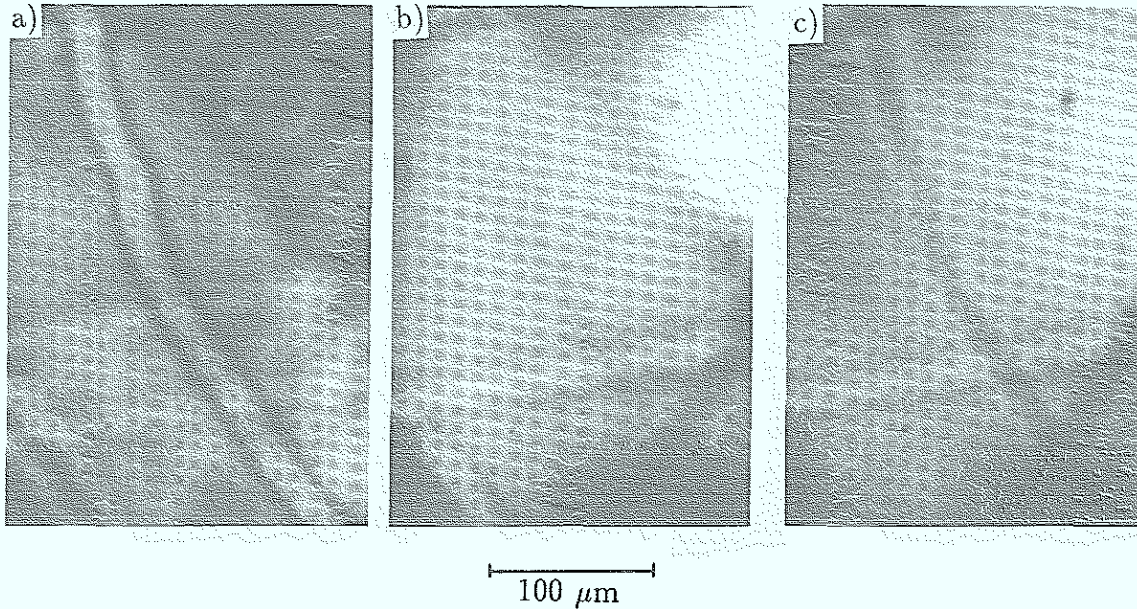


Fig. 19: "Cottrell" atmosphere of a dislocation segment close to the surface of a Si-doped sample. Figures a, b, c correspond to different focussing condition (a, further away; b, in focus; c, closer).

Assuming that the above interpretation of the bright field contrast is correct, the "focal length" of a "Cottrell" atmosphere can be estimated from figure 17 and 18 to about $80 \mu\text{m}$. This corresponds to a "refraction effect" $d/f \approx 0.04$. In figure 19 the "Cottrell" atmosphere extends over a larger area $d \approx 23 \mu\text{m}$ (this is due to a post growth annealing treatment which will be discussed in section 3.2.1) and the measured focal length is about $250 \mu\text{m}$. The "refraction effects" $d/f \approx 0.06$ is somewhat larger but of the same order of magnitude as for the Te-doped material. Using the expression for the focal length of a cylindrical lens as shown in figure 18, which is given by

$$f = -\frac{n \cdot d}{4\Delta n} \quad \text{see ref. [49 p. 66]} \quad (10)$$

the difference between the refractive indexes in the matrix and the "Cottrell" atmosphere can be estimated to $\Delta n \approx 0.03$ and 0.045 respectively.

As discussed in the previous section the "Schlieren" technique is particularly suited to make objects visible which give rise to refractive effects. In spite of the fact that the "Schlieren" microscope used in this work would be able to detect "refraction effect" at least on order of magnitude smaller than estimated above, "Cottrell" atmospheres do not generate any visible image contrast for similar illumination intensities as used for the bright field images in figure 16, 17 and 19. This indicates that the "refraction effects" and values for Δn estimated above are much too large³ or in other words that the image contrast in figure 16, 17 and 19 must be interpreted in a different way. Before presenting an alternative explanation for the bright field images of "Cot-

³This will be confirmed by the results from phase microscopy which find values for Δn almost two orders of magnitude smaller

trell" atmospheres the results of figure 20 will be briefly discussed. When increasing the illumination intensity by more than an order of magnitude the "Cottrell" atmosphere becomes also visible in the "Schlieren" microscope. This is probably due to the fact that this contrast technique – as discussed in the previous section – is also sensitive to phase objects, although only to higher order terms ($\varphi^2 \dots$). Higher illumination intensities are required for detecting these higher order effects.

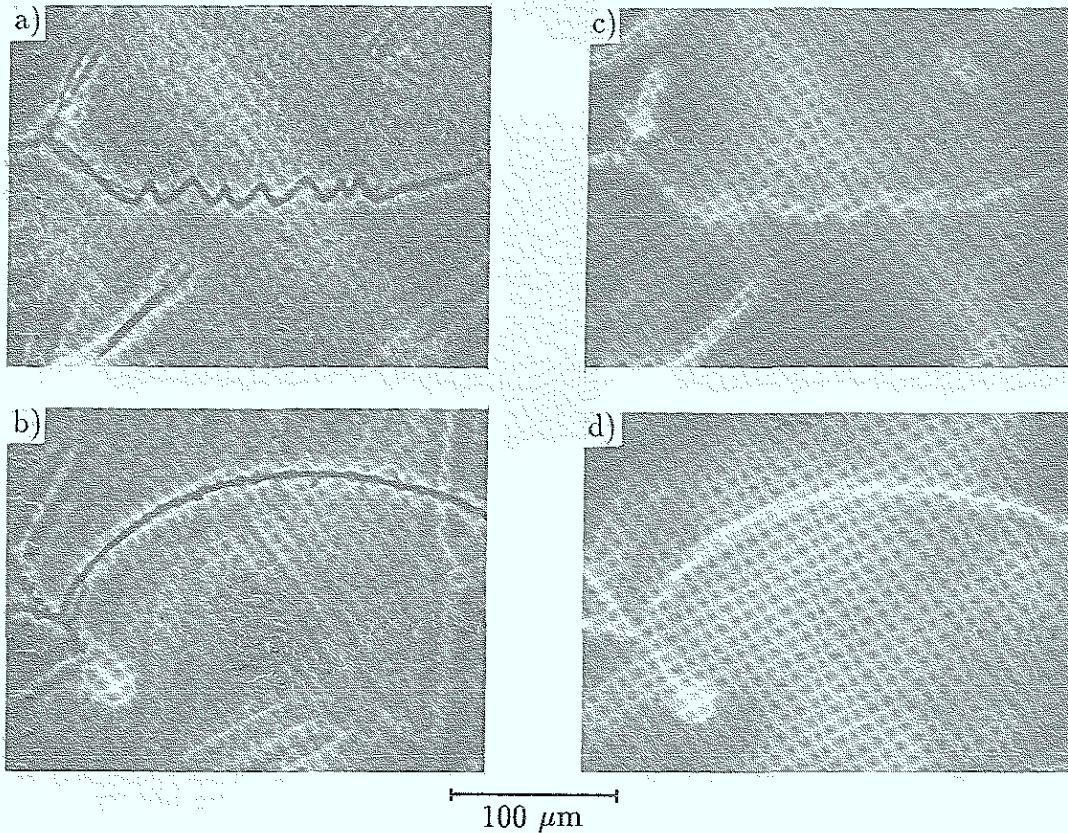


Fig. 20: Comparison of phase microscopy- and "Schlieren" images taken from identical sample areas: (Note: The illumination intensity for figure c) and d) is about an order of magnitude larger than in figure a), b)).

Returning back to the explanation of the bright field images of "Cottrell" atmosphere it is interesting to note that before the introduction of phase microscopy it was a well known fact to microscopists that small phase objects can be visible in ordinary microscopes. An example is given in figure 21, which shows a typical phase object (epithel cells) taken by phase microscopy and bright field contrast for different focussing conditions. A theoretical description of these effects has been given by H.H. Hopkins in [54] The visibility of small phase objects is largely due to the failure of real microscope objectives to collect all the light which is diffracted by the object, i.e. the missing part of the deviated light is responsible for the image contrast. Among earlier microscopists (see also [41, 42]) it was well known that the contrast could be made more pronounced by slight defocussing of the microscope as shown in figure 17, 19 and 21. The improved contrast is usually accompanied by a lower lateral resolution and an increase of adverse diffraction effects.

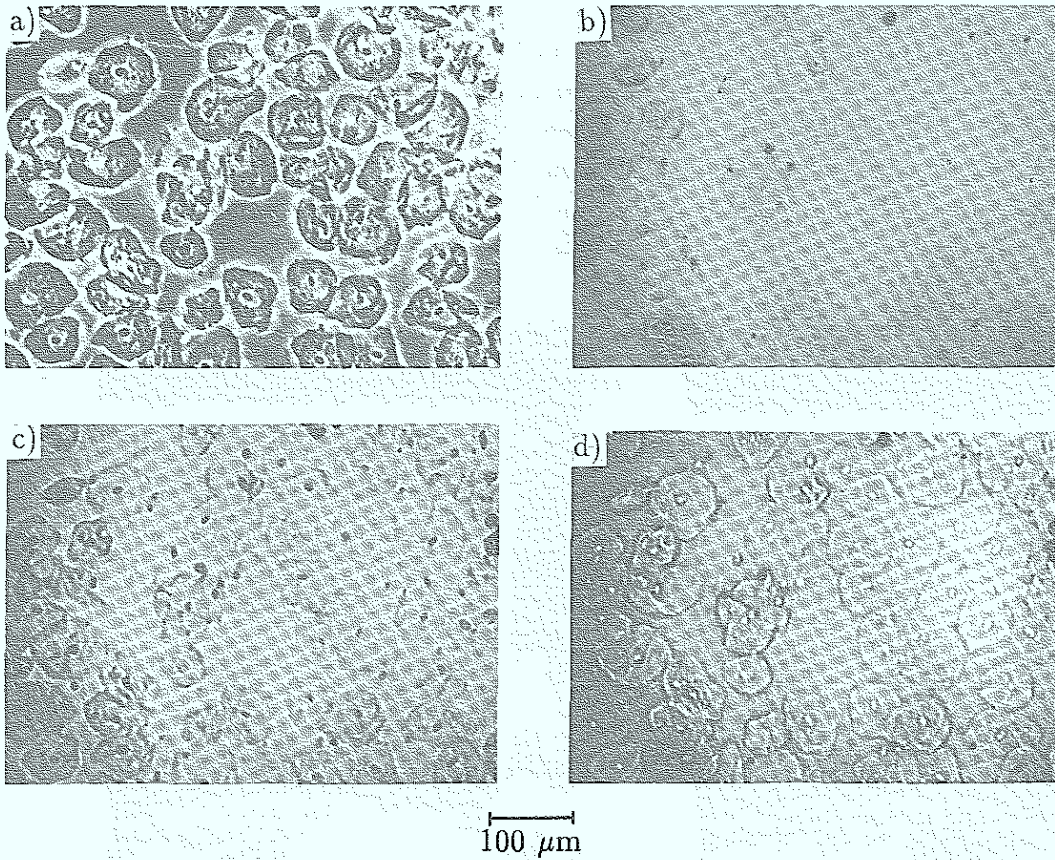


Fig. 21: Phase microscope (a) and bright field images (b: in focus; c: out of focus (close) d: out of focus (far)) of epithel cells.

The most pronounced image contrast of a phase object naturally can be obtained by phase microscopy (figure 21a). This is also the case for “Cottrell” atmospheres (see figure 22 and 23) again identifying them as pure phase objects. Strong absorption or refractive effects (or gradient in n) can be excluded from the previous discussion.

Whereas the “Cottrell” atmosphere in figure 22 remains almost invisible under bright field condition those parts which are out of focus (see dislocation segments A in figure 23) again show a stronger contrast. Since the microscope is equipped with a phase ring which creates a positive phase contrast the “Cottrell” atmosphere of Te-doped (Si-doped) GaAs must be optically denser (less dense) than the surrounding material. Employing equation (7) the difference in the refractive index, Δn can be roughly estimated if we assume that the image contrast in figures 22 and 23 is between 0.05 and 0.25.

$$\Delta n = \frac{K \cdot t}{2\pi} \cdot \frac{\lambda}{d} \quad (11)$$

where $t = 0.5$ and $d \approx 10 \mu\text{m}$ (width of the “Cottrell” atmosphere)

$$4 \cdot 10^{-4} < \Delta n < 2 \cdot 10^{-3}$$

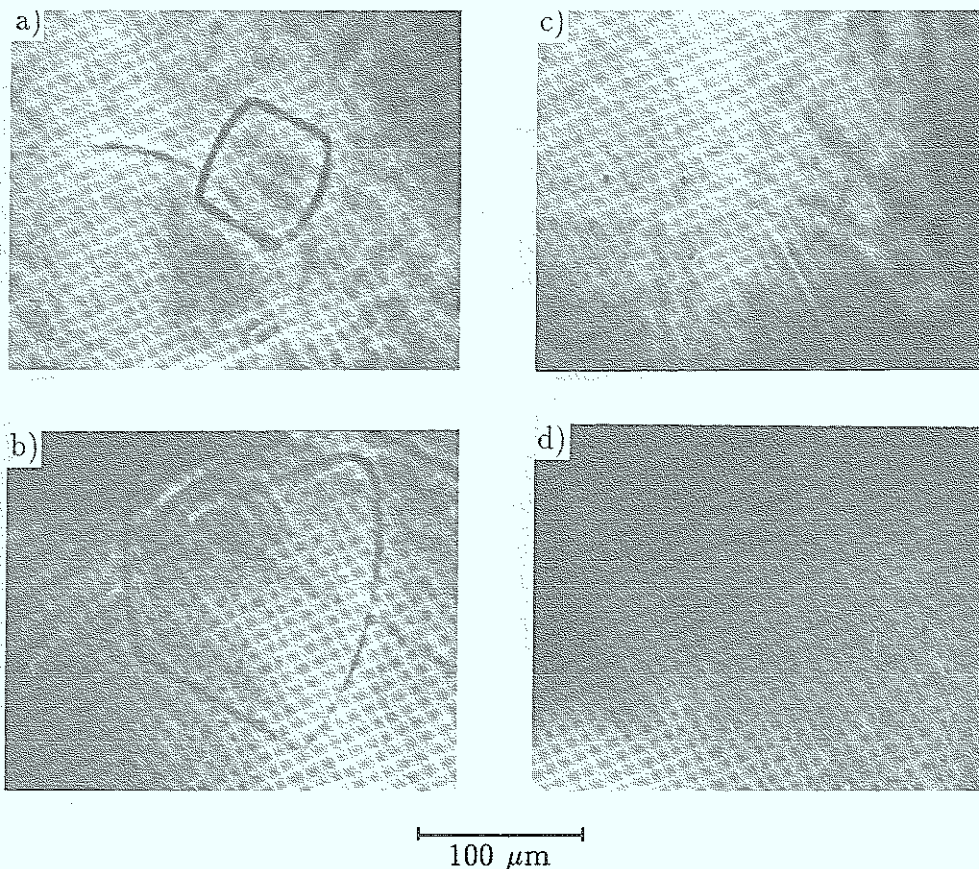


Fig. 22: Comparison of a phase microscope – and bright field image of the identical area in a Te-doped sample (Ph.C.: a, b; BF: c,d).

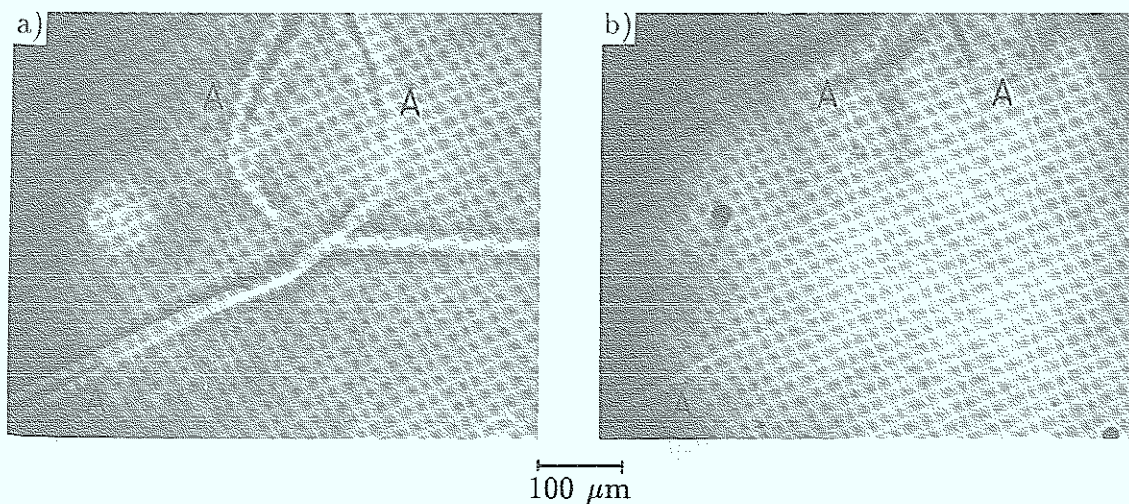


Fig. 23: Comparison of a phase microscope – (a) and bright field (b) image of the identical area in a Si-doped sample.

This means that Δn is one to two orders of magnitude smaller than from the earlier estimate which was based on a false interpretation of the bright field images. As a consequence the refraction effects generated by “Cottrell” atmospheres must be also much smaller ($d/f = \frac{4\Delta n}{n} \approx 10^{-3}$) explaining why no “Schlieren” image can be obtained under normal illumination condition as used for bright field – and phase microscopy.

Haloeffects of phase contrast images:

Haloeffects are well known among phase microscopists. The dark (bright) central contrast in figures 22a and 23a is accompanied by a bright (dark) halo. These effects would not exist for ideal phase contrast conditions as described in the previous chapter. Haloeffects are due to the fact that for real phase microscopy the phase ring has a finite extension (i.e. it is not infinitesimal small). As a result part of the deviated (diffracted by the phase object) light also passes through the phase plate, thereby receiving a phase shift of -90° s. For this reason Haloeffects are less pronounced for smaller phase objects because more light is diffracted by larger angles.

Theoretically it can be shown [41] that the distribution of the intensity generated by a phase object shown in figure 24a may differ from the ideal distribution (solid curve in figure 24b) in two respects. (Differences depend on the parameter $P = 2\pi \frac{Wd}{f\lambda}$, where W is the width of the phase ring, d the diameter of the phase object, f the focal length of the microscope objective and λ the wavelength of the light). The haloeffect increases with increasing d , W and decreasing f and the central intensity approaches more and more the intensity of the surrounding. With increasing P this means that for real phase microscopy large phase objects are only visible along the borderline which separates areas with different refractive indices. This effect can be demonstrated by imaging the same "Cottrell" atmosphere for different parameters P . As shown figures 25 a) and b) the center contrast is reduced for higher magnification because this corresponds to a larger P -value: see table I.

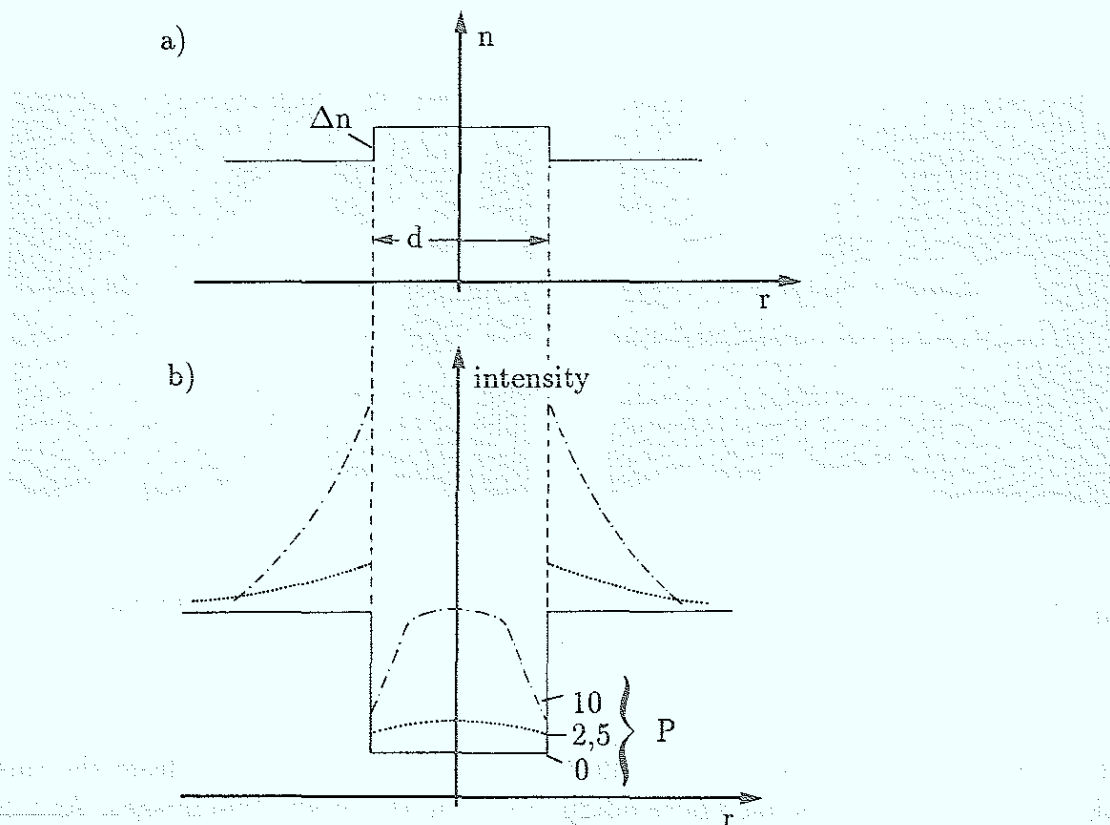


Fig. 24: a) Disc shaped phase object; b) Calculated radial intensity distribution of this phase object for different parameters of P . The calculation were based on a phase difference of $\varphi = 25^\circ$.

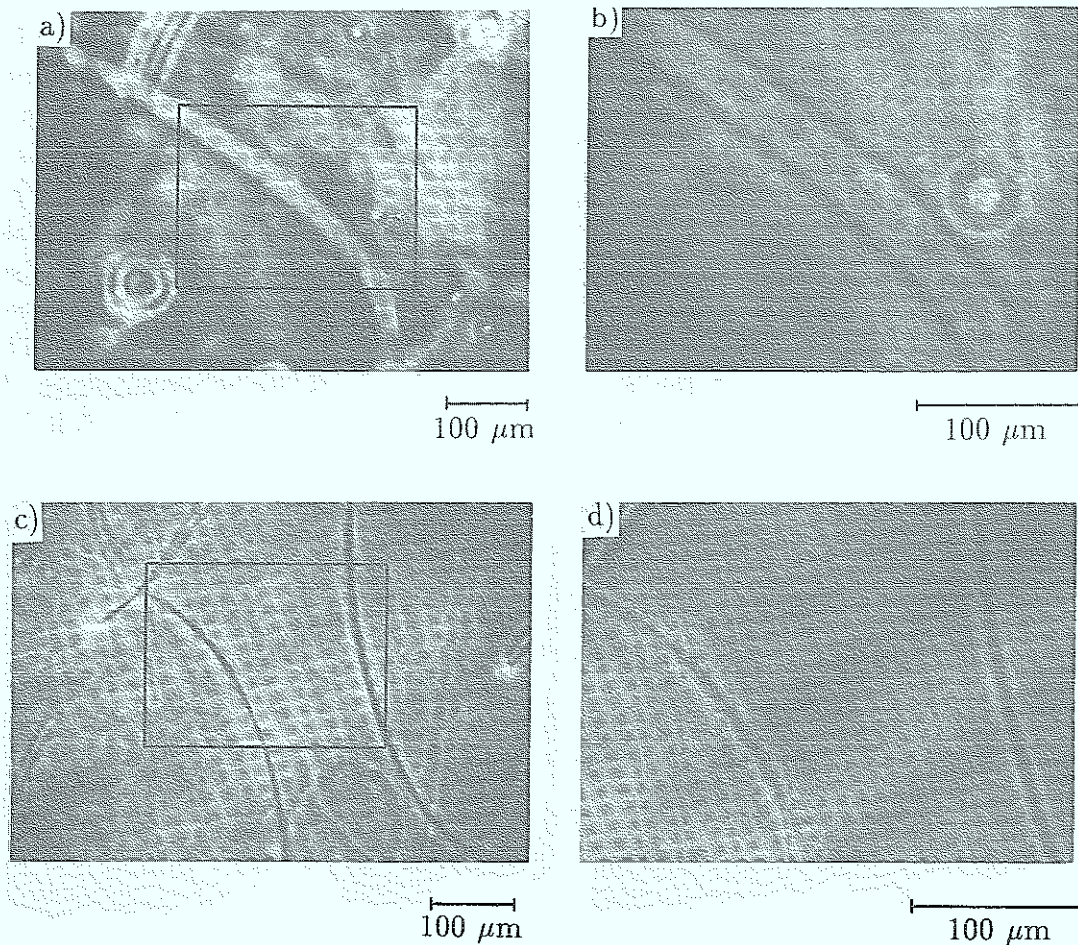


Fig. 25: a), b) Influence of parameter P on the image contrast of "Cottrell" atmospheres in Si-doped GaAs (insert in a, corresponds to figure b)). c), d) Influence of parameter P on the image contrast of "Cottrell" atmospheres in Te-doped GaAs (insert in c, corresponds to figure d).

Table I:

Magnification of the microscope objective	f (mm)	W (mm)	$P = 2\pi \frac{Wd}{f\lambda}$; λ and d in μm)
10 ×	17	0.5	0.18·d
20 ×	8.5	0.6	0.47·d

3.1.2 Interpretation of the difference in the refractive index between the "Cottrell" atmosphere and the surrounding material

As already shown in the previous section "Cottrell" atmospheres can be studied by photoetching, photoluminescence, EBIC, Ramanscattering as well as by phase microscopy. The effects observed by different techniques have been attributed to similar mechanisms, which may be also helpful for interpreting the observed difference in the

refractive index between the “Cottrell” atmosphere and the surrounding material. For following this route it is important to prove that different techniques indeed are looking at the same effect, i.e. the same zone around a dislocation. The phase microscopy is able to observe “Cottrell” atmospheres in the volume as well as in surface-near areas of a sample. Therefore it is possible to compare the result of phase microscopy with that obtained from photoetching (only revealing surface structures) for a particular dislocation. This is seen in figure 26: The DIC-image showing the etching profile reveals several dislocations emerging at the sample surface. The phase contrast image shows that these dislocations are lying almost parallel, slightly inclined to the surface. This configuration allows to measure the width of a particular “Cottrell” atmosphere by both methods and the result confirms our expectation that different techniques indeed reveal the same zone around the dislocation.

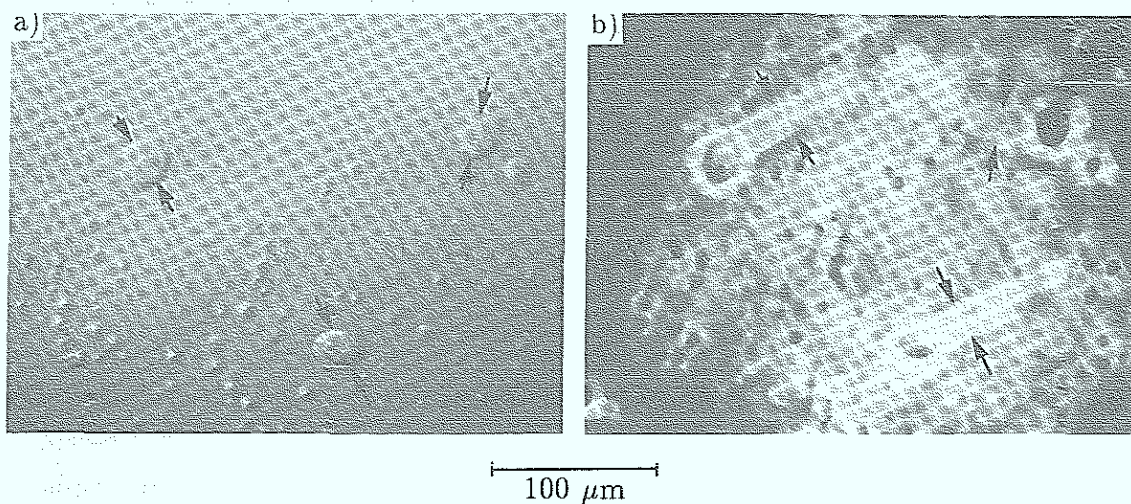


Fig. 26: a) Differential interference contrast (DIC)-image of a photoetched surface. The Si-doped material received a post growth annealing treatment of 40 h at 950 °C. b) Phase contrast image of the identical area.

The reduced etching rate is due to a reduced concentration of holes in the “Cottrell” atmosphere. This has been interpreted [53] as being due to an increased concentration of Si and so called nonradiative recombination centers, the nature of which remains unclear. The increased concentration of both defects has been attributed to their interaction with dislocations. The result of photoluminescence – EBIC – [9] and Ramanscattering [10] measurements are often also explained in terms of this model, although photoetching (see equation 9), EBIC and Ramanscattering cannot determine the concentration of Si directly, but only changes in the free charge carrier concentration, $N_D - N_A$. Such a change, however can also be caused by a redistribution of donors and acceptors, i.e. for example by increasing the number of donors at the expense of acceptors. This interpretation would be also consistent with the photoluminescence results which indicate an increase of donors. In the next section we will discuss a possible mechanism together with arguments which make an increase of Si in a zone extending up to 50 μm from the dislocation very unlikely. An increase of Si is also unnecessary since all result including those from phase microscopy (as shown below) can be understood in terms of an increased free carrier concentration only. In addition recent measurements of the diffusion of single Si-atoms in GaAs show that

their diffusion length at 950 °C is much too small (see also section 3.2.3) to explain the large extension of the “Cottrell” atmosphere.

The results for Te-doped and Si-doped material (which has been grown from a Ga-rich melt) exhibit a decrease in the free carrier concentration around dislocations. This has been measured by EBIC [9, 55] and is shown in figure 27 and 28 by an increased etching rate (see figures 27e, 28e) and a dark center contrast (see A in figures 27c, 28a, c) in the phase microscopy images. Results of Si-doped material grown from Ga-rich melt show some features which are yet not very well understood. The radial distribution

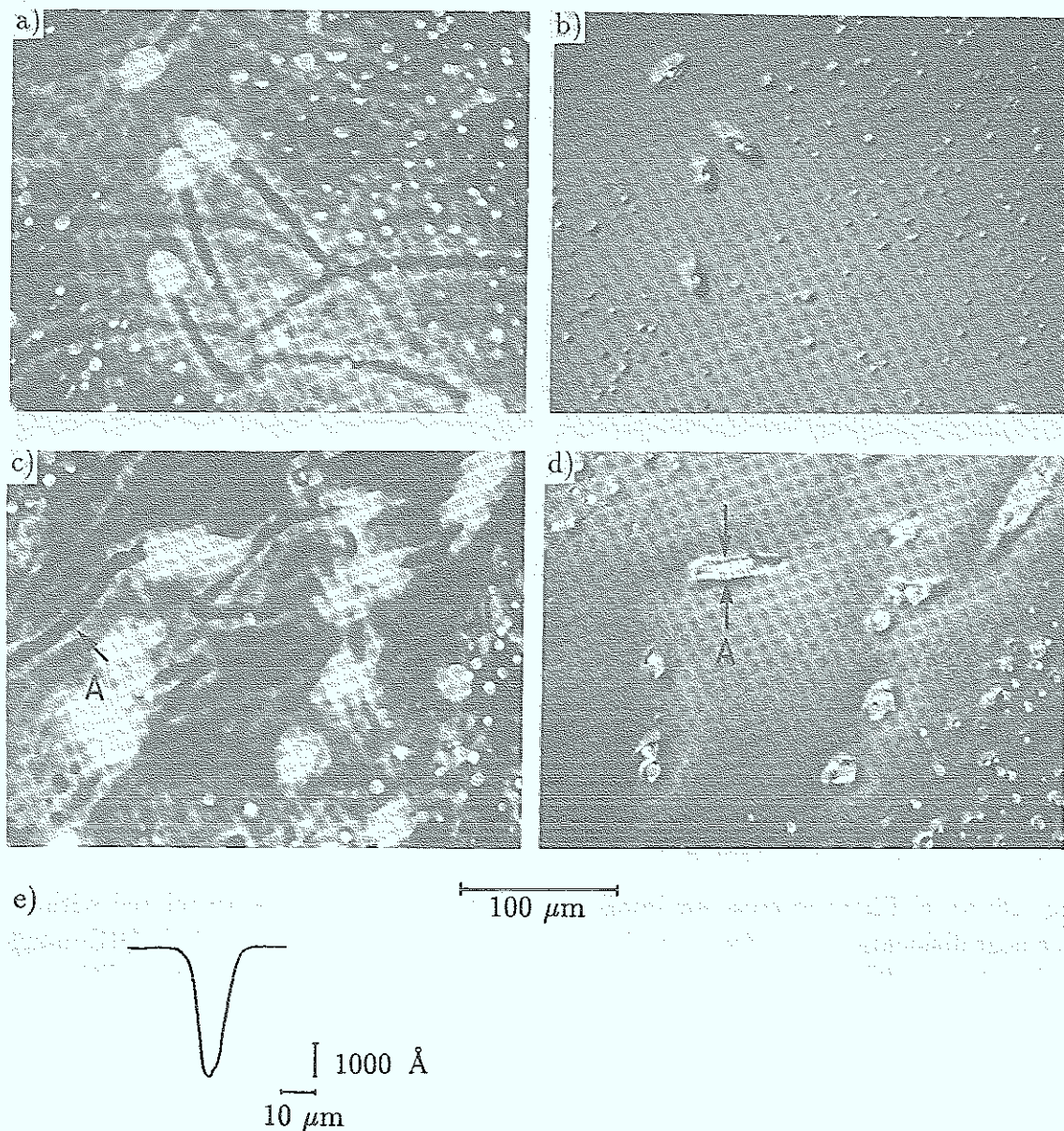


Fig. 27: a), c) Phase microscopy images of “Cottrell” atmospheres associated with surface near dislocations (Te-doped material). b), d) DIC-images of the photoetched surface area identical to a). e) Surface profile close to a dislocation after photoetching.

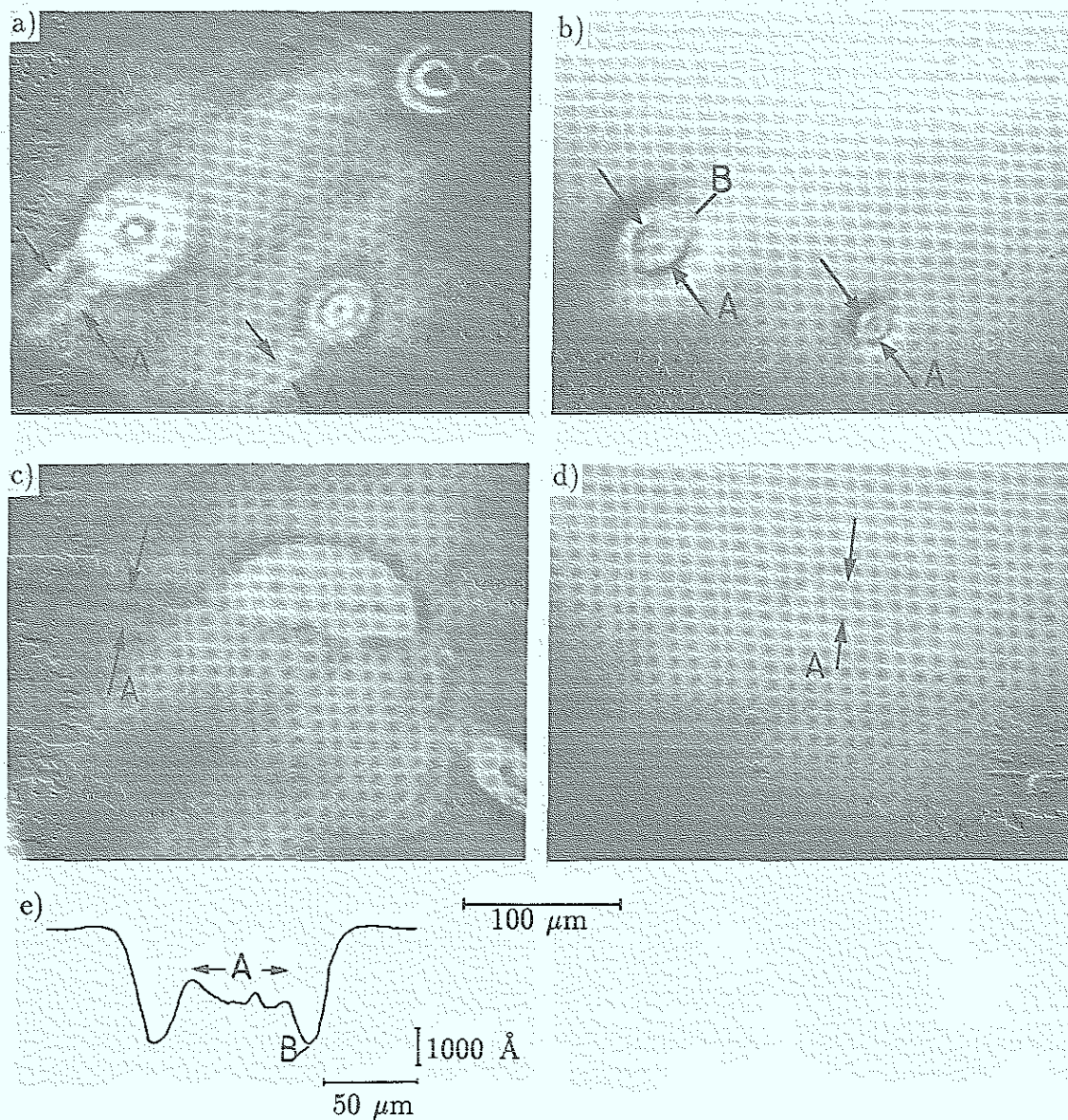


Fig. 28: a), c) Phase microscopy images of “Cottrell” atmospheres associated with surface near dislocations (Si-doped material grown from Ga-rich melt). b), d) DIC-images of the photoetched surface areas identical to a). e) Surface profile close to a dislocation after photoetching.

of the etching rate is rather complicated and the area of the reduced etching rate (see annular area B in figure 28b, e) extends further from the dislocation than the dark center contrast observed by phase microscopy. The halo effects in figure 28a appear rather strong, indicating that they may not be entirely due to imperfections in the imaging system. Further investigations are necessary to understand these details; the main result of figure 28, however, is qualitatively the same as for Te-doped material. It

is interesting that the microdefects around dislocations resolved by photoetching (figure 29) are also similar for both materials. Detailed analysis shows that the microstructure laterally extends over the same area (see e.g. dislocation A in figure 27 and 28) which also exhibits dark contrast in the phase microscopy image, i.e. an area where the free carrier concentration should be reduced. For Te-doped material it has been shown by TEM-studies [56] that 2-dimensional precipitates are formed around dislocations, which have been identified as Ga_2Te_3 [57]. The formation of Te-precipitates could be a possible mechanism for explaining the reduction of the free charge carrier concentration in the “Cottrell” atmosphere. The microstructure detected around dislocation with photoetching for the “Ga-rich” Si-doped material has not yet been studied by TEM. Therefore it is unclear whether the reduced free carrier concentration can be associated with formation of precipitates.

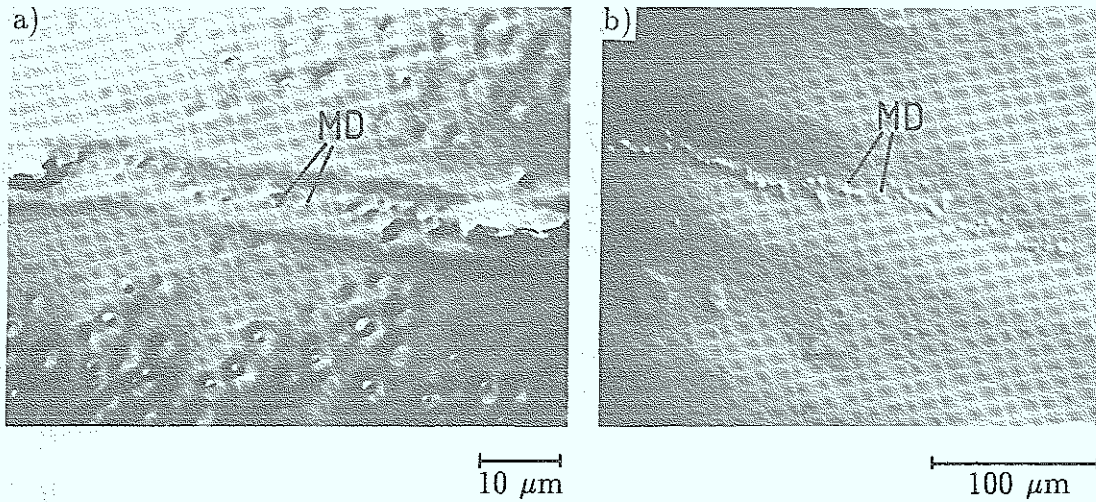


Fig. 29: DIC-image after photoetching of Te-doped (a) and Si-doped (b) material. The “Cottrell” atmosphere shown is associated with a dislocation lying close and parallel to the surface of the sample (MD = Microdefects).

Relation between the refractive index and the free charge carrier concentration:

In a conducting material the refractive index will become dependent on the free charge carrier concentration \bar{n} , if the frequency of the electromagnetic wave is high enough that the inertia of the electrons is affecting the induced current. In this case the refractive index decreases with increasing \bar{n} because the induced current is lagging in phase. As shown e.g. in ref. [58] the change in the refractive index becomes equal to

$$\Delta n = -\frac{2\pi\Delta\bar{n}e^2}{\omega^2 m_{\text{eff}}} \quad (12)$$

Changes of the free carrier concentration measured by EBIC [9, 55] are listed in Table II. From these values for $\Delta\bar{n}$ we can estimate the corresponding phase shift and Δn due to the “Cottrell” atmosphere (for table II, $d \approx 5 \mu\text{m}$ has been assumed) as well as the contrast expected for phase microscopy images. The estimated values for K roughly agree with those observed in phase microscopy images.

Table II:

	$\Delta\bar{n}$ (cm ⁻³)	Δn	φ (radians)	K
[9] Si-doped	$\approx 1.5 \cdot 10^{17}$	$\approx -10^{-3}$	-0.03	+0.12
[9] "Ga-rich" Si-doped	$-5.5 \cdot 10^{17}$	$\approx +3.5 \cdot 10^{-3}$	+0.11	-0.4
[55] Te-doped	$-4 \cdot 10^{17}$	$\approx +2.5 \cdot 10^{-3}$	+0.08	-0.3

Comparison of absorption and phase contrast:

Employing equations (7, 11) for the refractive index and equations (1, 2) for the absorption coefficient we can now quantitatively answer the earlier question: To what extent is the phase microscopy image caused by changes in the absorption coefficient and refractive index, respectively?

$$\frac{K_{\Delta\alpha}}{K_{\Delta n}} = \frac{-\Delta\alpha \cdot d/2}{-\frac{2\pi}{t} \cdot \Delta n \cdot \frac{d}{\lambda}} \approx -3 \cdot 10^{-3} \quad (13)$$

In agreement with our earlier conclusion absorption effects are completely negligible as compared to the influence of the refractive index. In addition the contrast expected from absorption effect would be inverse to the observed one, i.e. an increased free carrier concentration (figure 23) would generate a dark contrast of the "Cottrell" atmosphere if absorption effects were dominating.

Although bright field images are less sensitive for phase objects (see figure 21), because the image contrast is only due to imperfections in the imaging system, absorptions effects are still negligible for "Cottrell" atmospheres as shown earlier. For image contrasts caused by variations in the free charge carrier concentration phase contrast effects are dominating absorption effects. This is very important e.g. for calculating variations in the doping concentration due to growth striations. These calculations have been often based in the past on absorption [40] effects only (see also section 3.2.3).

Dependence of phase contrast on the wavelength:

Most phase contrast images presented in this paper have been obtained in a wavelength region which is determined by the spectral absorption (see figure 3) and by the spectral sensitivity of the CCD-camera (see figure 4) i.e. $0.9 < \lambda < 1.4 \mu\text{m}$. Three (a, c, e) of the images shown in figure 30 were taken at a wavelength of $0.9 (\pm 0.01) \mu\text{m}$. They exhibit a much more pronounced contrast than images taken at larger wavelengths.

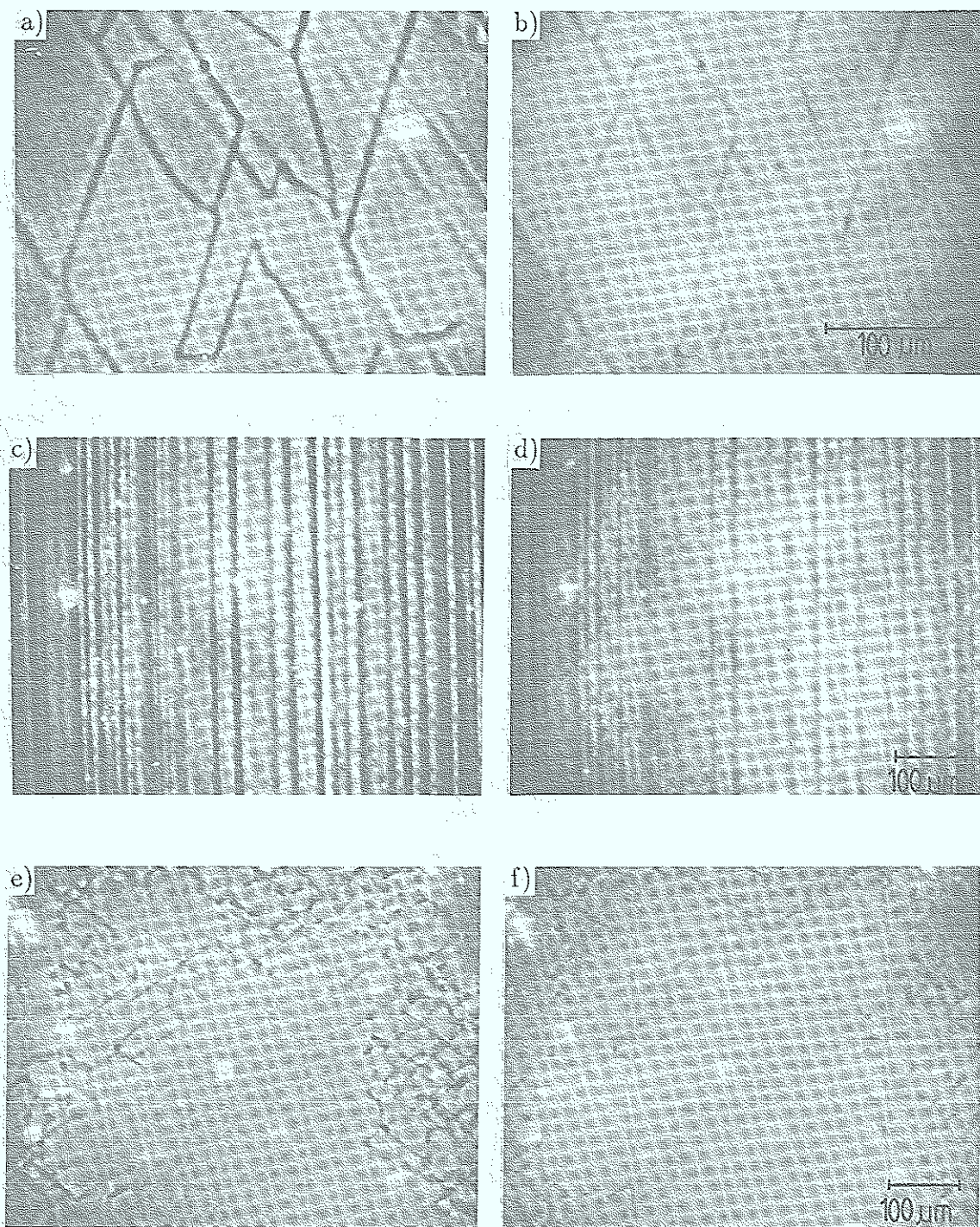


Fig. 30: a), b) Phase microscopy image of Te-doped material grown by VB-technique:
 a) $\lambda = 0.9 \mu\text{m}$ b) $0.9 < \lambda < 1.4 \mu\text{m}$
 c), d) Phase microscopy image of growth striations in Si-doped GaAs (LEC-grown):
 c) $\lambda = 0.9 \mu\text{m}$ d) $0.9 < \lambda < 1.4 \mu\text{m}$
 e), f) Phase microscopy image of Te-doped material grown by VB-technique (a very high growth rate results in a higher dislocation density which is reflected in the formation of cellstructure):
 e) $\lambda = 0.9 \mu\text{m}$ f) $0.9 < \lambda < 1.4 \mu\text{m}$

According to equation (7), (11) and (12)

$$K = -\frac{\varphi}{t} = \left(\frac{d}{t} \cdot \frac{e^2}{c^2 m_{\text{eff}}} \cdot \frac{\Delta \bar{n}}{2\pi} \right) \lambda \quad (14)$$

we expect a higher contrast for larger wavelengths. This indicates that equation (12) is probably too simple to relate the free carrier concentration with the refractive index in a realistic way. From a theoretical point of view this is not surprising, since the refractive index, n , is associated with the absorption coefficient via the Kramers-Kronig relation [60]

$$n(\omega) - 1 = \frac{1}{2\pi} \int_0^{\infty} \frac{\omega' k(\omega') d\omega'}{\omega'^2 - \omega^2} \quad (15)$$

where $\omega' k(\omega')$ ⁴ is proportional to the absorption coefficient $\alpha(\omega')$. In principle the refractive index n therefore can be calculated if the absorption coefficient is known for all frequencies. Unfortunately this is not the case particularly for frequencies above the absorption edge. Since we are mainly interested in the refractive index slightly below the absorption edge (near infrared: $0.9 < \lambda < 1.3 \mu\text{m}$) the two main absorption mechanisms important in this frequency range should be also relevant for determining the refractive index: (i) The fundamental absorption at the band edge, (ii) the interconduction band transition [37]

Both mechanisms can only be understood quantummechanically and they are not related to the simple model which was used to derive equation (12). Employing the dispersion relation (15) F. Stern [61] estimated the contribution of free carriers through interconduction band transitions to the refractive index to

$$\Delta n \approx -\frac{10^{-20} \Delta \bar{n}}{n E^2} \quad (16)$$

where E is the photon energy in (eV). Although this relation is determined by a completely different mechanism as compared to equation (12), it is interesting that Δn is similar in both cases (Δn (16) / Δn (12) ≈ 0.3). Also $\Delta n \sim 1/\omega^2$ for both mechanisms, i.e. neither one is able to explain the result shown in figure 30. To obtain the correct frequency dependence it is important to take the fundamental absorption into account. As a result of the steep rise of the absorption at the band edge the refractive index is peaked at the corresponding frequency as shown in figure 31 for undoped GaAs.

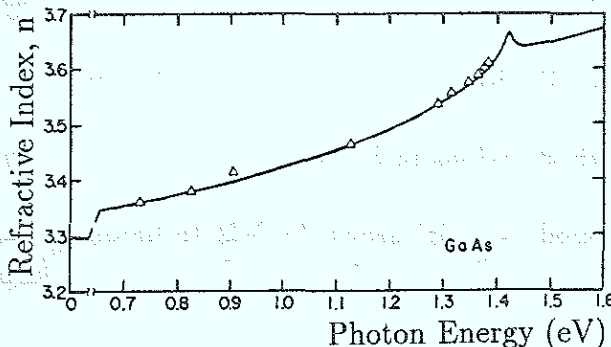


Fig. 31: Measured and calculated refractive index for pure GaAs [61] at 300 K.

⁴ $k(\omega')$ is the extinction coefficient

It has been shown in Ref. [62] that for n-doped material the refractive index is less peaked ⁵ than for undoped material. For increasing doping concentration (n-type) this peak receives a so called Burstein-shift [63] to higher frequency values, because the absorption edge of semiconductors, with small energy state densities the conduction band is shifted to higher energies. Calculated and measured data from ref. [62] and [64], resp. are shown in figure 32a, b. It is interesting to note that the measured data show a stronger dependence on the doping concentration particularly in the range of 10^{18} (cm^{-3}); the measured variation of Δn with $\Delta \bar{n}$ is very close ($\approx 30\%$ larger) to that calculated from equation (12). As a result of the Burstein-shift the same change in the free carrier concentration, $\Delta \bar{n}$, introduces a larger variation of the refractive index at higher frequencies. This explains qualitatively the result shown figures 30, i.e. a higher contrast for a smaller wavelength.

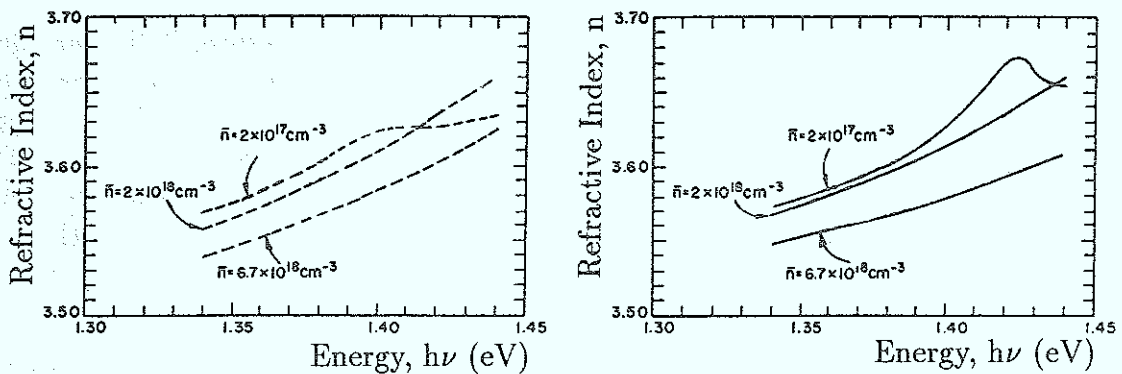


Fig. 32: Measured a) and calculated b) refractive index values as a function of energy for different concentrations of n-type impurities [62].

3.2 Application of Phase Microscopy

In the previous sections we have shown that phase microscopy can be employed to study variations of the free charge carrier concentration associated with the microstructure in doped GaAs crystals. Phase microscopy has a similar potential to study these effects as photo-etching, EBIC and Ramanscattering: while all techniques exhibit similar lateral resolution of $\approx 1 \mu\text{m}$, phase microscopy is probably not as sensitive as the other methods to resolve variations in free carrier concentration (the lower limit is probably $\Delta n \approx 5 \cdot 10^{16} \text{ cm}^{-3}$); in this respect photo-etching is superior to all other techniques although it only provides qualitative results. A calibrated photo-etching technique remains to be established. The main advantage of phase microscopy is that variations of the free carrier concentration can be determined also inside the material whereas only surface effect can be detected by all other techniques. This is very important when studying post-growth annealing effects, which will be discussed in the first part of this section. High temperature ($\gtrsim 600 \text{ }^\circ\text{C}$) annealing treatments inevitably damage to some extent the surface of GaAs-samples. As a result identical areas of the sample cannot be compared before and after annealing when employing only surface techniques. With phase microscopy it is possible to study annealing effects on specific "Cottrell" atmospheres or dislocations inside the sample.

⁵Because the increase of the intrinsic absorption is much less steep than for pure GaAs, see ref. [36: page R148]

In the second part of this section we will present results obtained by phase microscopy on gliding processes which occur due to the buildup of thermal stresses during the cooling period after the crystal growth is completed. In the third part we will discuss phase microscopy studies on growth striations. From annealing results of growth striations we will obtain informations about the diffusion of Si in GaAs, which is still a controversial issue in the literature. Finally, details of the microstructure in Te-doped material as obtained by photo-etching and phase microscopy will be described.

3.2.1 Post growth annealing studies

a) Si-doped material: 950 °C annealing treatment.

In order to compare the effect of annealing on the microstructure, individual dislocations and "Cottrell" atmosphere were documented before annealing as shown in figure 33a, b, c, d. After the annealing treatment (see also chapter 2) the samples were repolished and identical sample areas redocumented (figure 33e, f, g, h). During the 10 h anneal at 950 °C all "Cottrell" atmospheres have substantially grown in diameter (to about 14 μm) and, in addition, some of them also show growth of lateral humps (A). It should also be noted that along some short dislocation segments "Cottrell" atmospheres do not grow (B).

The result of an additional annealing of the same sample for another 40 h at 950 °C is shown in figures 34 and 35 for the two areas from figure 33a and b. A further growth of the "Cottrell" atmospheres to about 30 μm in diameter can be observed. The fact that the contrast of the "Cottrell" atmosphere after the second anneal appears much fainter, is probably due to the imperfections of the imaging technique (see real Zernike method in section 3.1.1). The size of the lateral humps is also increasing and dislocation segments which did not show any growth of the "Cottrell" atmosphere during the first annealing treatment remain unchanged also during the second anneal.

Employing also dark field contrast (see Chapter 2) large precipitates decorating the dislocation can be detected as shown in figures 34d and 35d. It is interesting that lateral humps are observed where the dislocations also show lateral extensions decorated with precipitates and dislocation segment where there is no growth of the "Cottrell" atmospheres no decoration precipitates can be detected either. This shows that there is a strong correlation between the growth of the "Cottrell" atmosphere and that of decoration precipitates (more evidence for this conclusion will be discussed later). The fact that no precipitates can be observed in the as grown material as well as after the 10 h annealing treatment could either mean that they are only formed after long time anneal or, more likely, that they are too small to be visible by our DF-technique.⁶

⁶The resolution of this technique is currently being determined by TEM-studies in our laboratory. Preliminary results indicate that DF-technique can resolve precipitates which are larger than 0.2 μm . The size of precipitates which exhibit a similar IR-scattering intensity as those in figure 34d and 35d have been measured by TEM [50] to about 0.30 μm . Assuming a one to one correlation between the formation of precipitates and the Cottrellatmosphere (see equation 17) we can estimate the size of precipitates after a 10 h anneal to $l_{10} = \left(\frac{d_{10}}{d_{50}}\right)^{2/3} \cdot l_{50} \approx 0.2 \mu\text{m}$ i.e. they may be just too small to be visible.

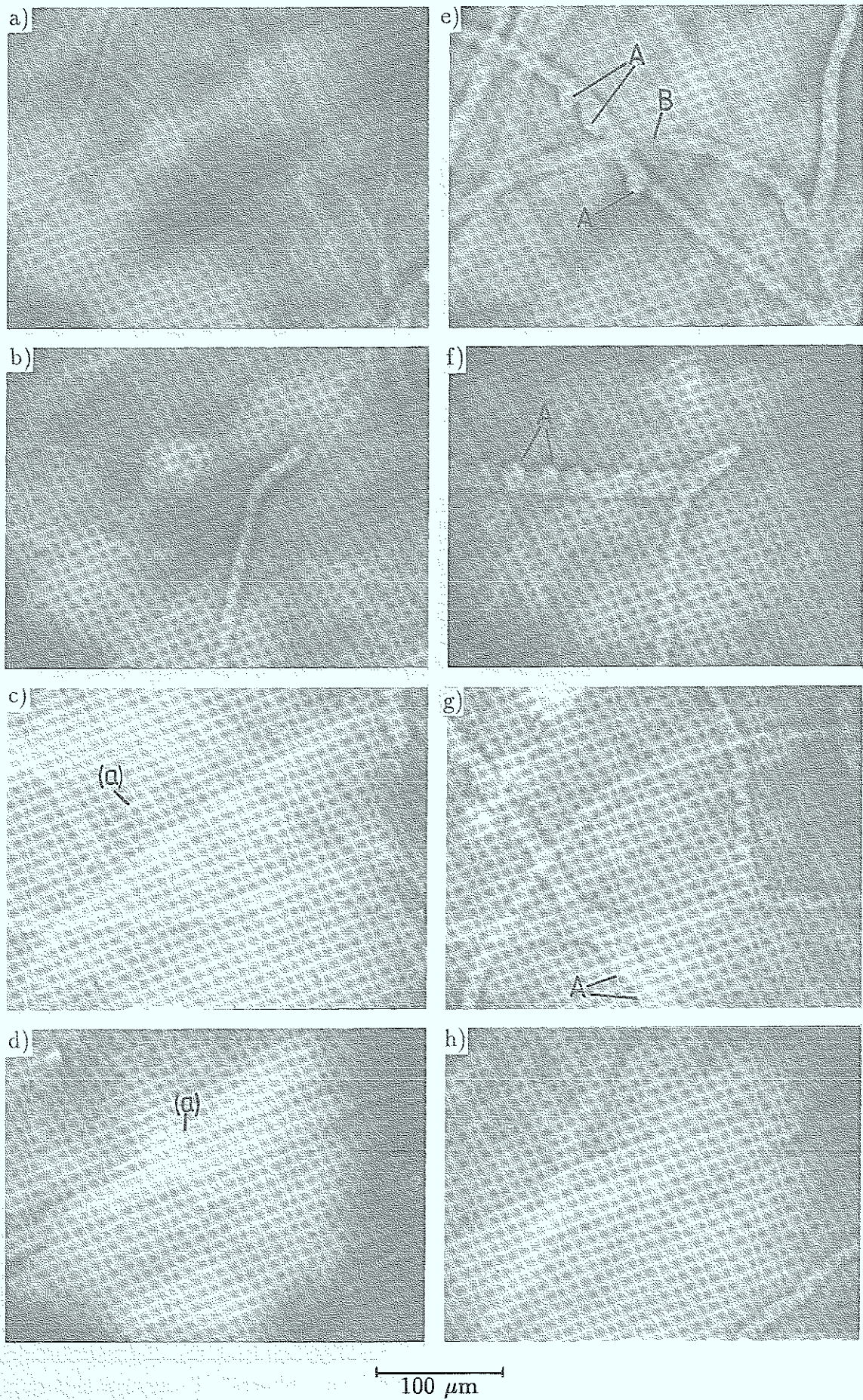


Fig. 33: Phase microscopy images of "Cottrell" atmospheres for Si-doped material: a), b), c), d), before annealing; e), f), g), h) after 10 h at 950 °C.

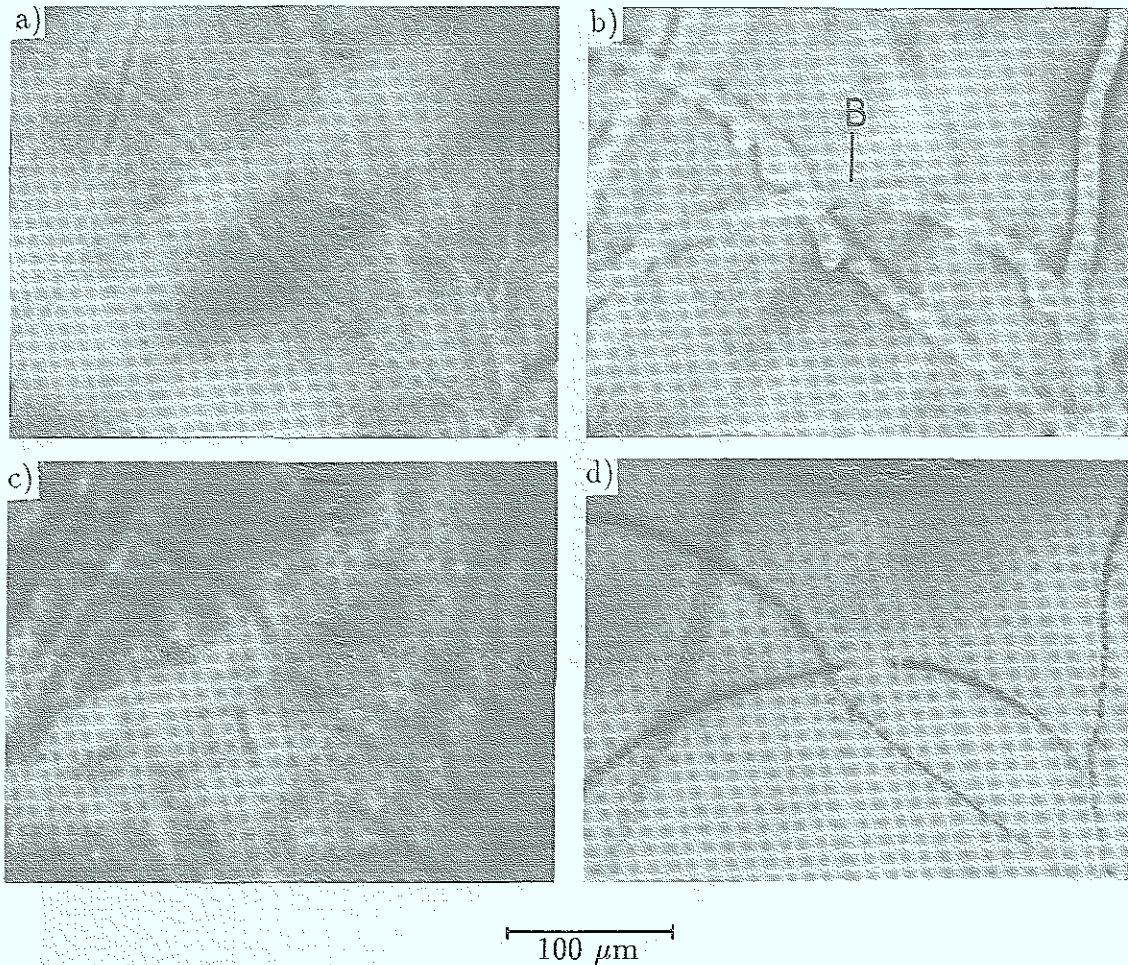


Fig. 34: Phase microscopy images of "Cottrell" atmospheres for Si-doped material a) as grown; b) after 10 h; c) after 50 h; d) dark field image after 50 h anneal at 950 °C.

The diameter of "Cottrell" atmospheres in Si-doped material at 950 °C is growing proportional to the square root of the annealing time. This means that the kinetics of the underlying defect mechanism for the formation of the "Cottrell" atmospheres is that of a diffusion process. It should be noted that only a limited amount of data is available and additional experiments will be required to confirm this conclusion. The result, nevertheless, again raises the question, whether it is justified to apply the term Cottrell-atmosphere to the zones around dislocations which can be observed by phase microscopy and other techniques? As shown below real Cottrellatmospheres are not dominated by a diffusion process. We still use the term Cottrell atmosphere here as already mentioned in section 3.1 – because photo-etching and EBIC-results have been attributed to an increased Si-concentration in the zone due to an elastic or electric interaction of Si-atoms with the dislocation. The crucial question is, whether a sufficiently strong interaction can exist up to distances of 50 μm from the dislocation equal to the lateral extension of the observed "Cottrell" atmospheres? To answer this question the definition and main characteristics of Cottrell atmospheres shall be repeated

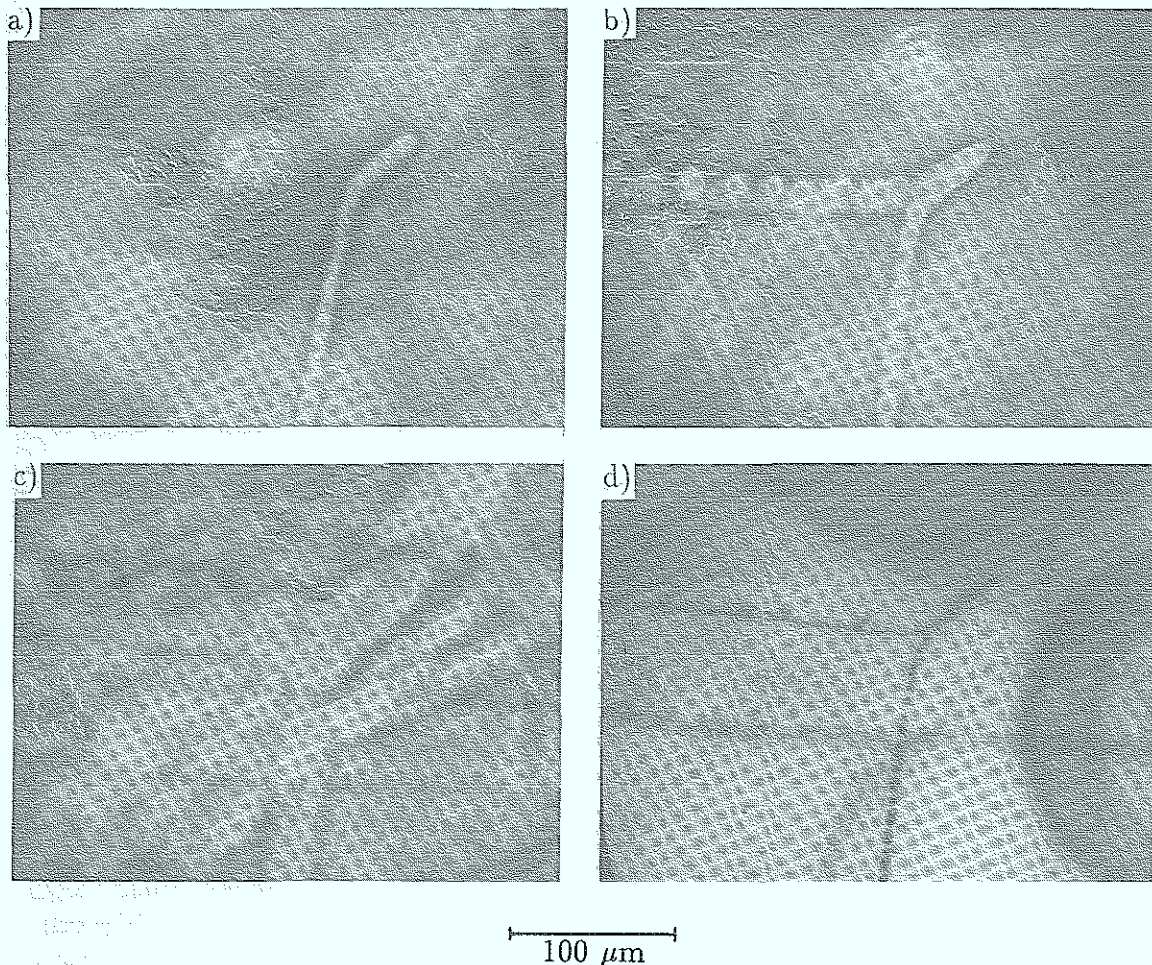


Fig. 35: Phase microscopy images of “Cottrell” atmospheres for Si-doped material
 a) as grown; b) after 10 h; c) after 50 h; d) dark field image after 50 h anneal at 950 °C.

employing the schematic diagram in figure 36. A Cottrell atmosphere is characterised by an increase of the impurity concentration close to the dislocation core due to the attractive interaction of the impurities with the dislocation. The impurities are delivered via diffusion from the outside of the “Cottrell” atmosphere and, consequently, a denuded (reduced impurity concentration) zone is formed around the real Cottrell atmosphere as indicated in figure 36. Within the Cottrell atmosphere the interaction energy between the impurity and the dislocation is sufficiently strong to trap impurities permanently. The lateral extension of the Cottrell atmosphere is roughly determined [59] by the distance from the dislocation where the interaction energy becomes equal to kT . Within the Cottrell atmosphere the flow of impurities is determined by the interaction with the dislocation and can be described as a drift term $j \sim \frac{D}{kT} \text{grad } E_i$ (E_i = interaction energy) which is much larger than the normal diffusion $j = D \text{grad } c$. Outside the Cottrell atmosphere where the interaction energy becomes $< kT$ the flow of impurities is determined by normal diffusion (these arguments are discussed in ref. [59, 65, 66]).

⁷The term Cottrell atmosphere is not restricted to impurity accumulations around dislocations.

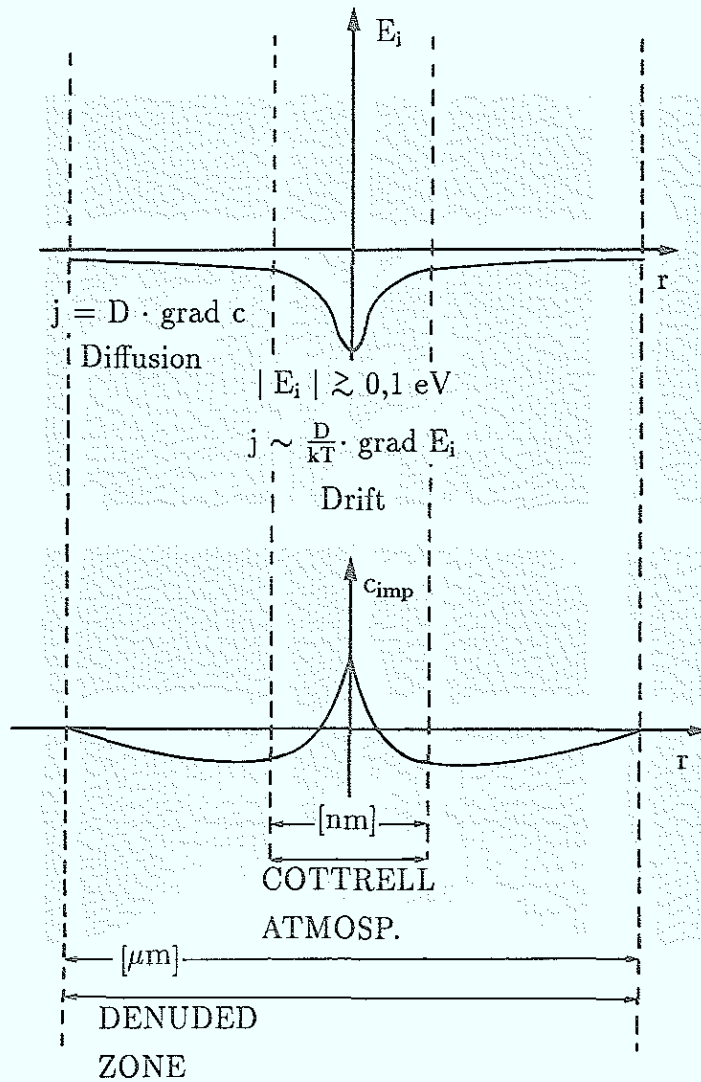


Fig. 36: Schematic diagram of a Cottrell atmosphere: Radial dependence of the interaction energy, E_i and impurity concentration, C_{imp}

The apparent "Cottrell" atmosphere for Si-doped material is still growing at 950 °C as shown in figures 33, 34 and 35. In the case of a real Cottrell atmosphere the interaction energy within this zone must be larger than $kT \approx 0.1 \text{ eV}$ (for 950 °C). Since the lateral extension is roughly $30 \mu\text{m}$ and the interaction energy falls off with the distance from the dislocation, $E_i \sim \frac{1}{r}$, we can estimate an interaction energy in the core area of the dislocation of roughly 5000 eV. This value is too high by probably three orders of magnitude. Therefore, the features observed in Figs. 33 – 35 are only apparent "Cottrell" atmospheres. They are denuded zones⁷, with an

extension which is determined by the diffusion length of the defect responsible for the increased free carrier concentration in this zone. Therefore, we must exclude Si as a possible defect, since the concentration of Si would have to increase in the denuded zone to explain the observed increase in the electronic carrier density. The increased carrier concentration can be attributed to a decrease of the concentration of compensating acceptors. In the following we shall discuss a possible mechanism which explains at least part of our results. The model is based on the fact that decoration precipitates are formed during long-time post-growth annealing at 950 °C. We assume that these

Native defects may also form Cottrell atmospheres as a result of their interaction with the dislocations. In both cases the radial distribution of defects can be described as indicated in figure 36 i.e. a Cottrell atmosphere very close to the dislocation with an increased defect concentration surrounded by a much further reaching denuded zone (apparent Cottrell atmosphere). For native defects the situation changes if the dislocation acts a source of defects rather than as a sink. Then, we may see an increase of defects around the dislocation extending as far as the diffusion of the emitted defect allows. As shown in ref. [67] and ref. [5] dislocation climb can generate Ga-vacancies which may diffuse into the surroundings where they can form As-antisites by reacting with As_i -interstitials. D.J. Stirland et al. [39] indeed measured an increase of EL2 around dislocations reaching as far as $50 \mu\text{m}$ into the surrounding material. His alternative explanation attributing the increased EL2 concentration to the gettering of point defects in the interaction field of the dislocation must be ruled out, because the interaction energy is much too small at a distance of $100 \mu\text{m}$.

are arsenic precipitates since they grow in the same temperature range as arsenic precipitates in undoped sample. As-precipitates have been identified by TEM in Si-doped LEC-grown crystals [68]. In order to form As-precipitates an excess of Ga-vacancies and As-interstitials is required. This condition is very likely because almost all GaAs-crystals are characterized by a large excess of arsenic as shown by chemical analysis [69, 70]. From these experiments we must conclude that after solidification arsenic interstitials and/or Ga-vacancies are present at a level of about $5 \cdot 10^{18}$ (cm^{-3}). After cooling only a minor fraction of the excess arsenic is found in precipitates. About 10^{16} cm^{-3} has been estimated to be present in precipitates decorating dislocations (see section 4 of ref. [44]). Somewhat higher values ($\approx 3 \cdot 10^{16}$ cm^{-3}) have been estimated in ref. [71] and in ref. [72]. In material which received a post growth anneal D.J. Stirland et al. [73] made a very rough estimate finding about 10^{17} cm^{-3} arsenic atoms at most in microprecipitates.

It is not clear in which form the majority of the excess arsenic exists in the material, but there are indications [74] that it could be present as interstitial atoms even after cooling the material to room temperature after crystal growth. For highly n-doped material we expect from theoretical arguments [75] also a relative high concentration of Ga-vacancies since they are negatively charged. We further assume that they are trapped at Si-atoms, forming $\text{Si}_{\text{Ga}}\text{V}_{\text{Ga}}$ -complexes with acceptor character. This type of defect has been identified by J. Krug and G. Spitzer [76] by measuring IR-absorption at local vibrational modes. After an annealing treatment at 1100 °C and after quenching the samples to room temperature they found that $\text{Si}_{\text{Ga}}\text{V}_{\text{Ga}}$ -complexes are formed after an additional annealing above 450 °C (beginning of vacancy migration). Above 900 °C the complexes start dissolving again. After a similar pre-treatment of Si-doped material [77] the yield stress values of the material could be increased by an additional annealing treatment at 400 and 700 °C. This result was also attributed to the formation of $\text{Si}_{\text{Ga}}\text{V}_{\text{Ga}}$ -complexes. A further indication for $[\text{Si}_{\text{Ga}}\text{V}_{\text{Ga}}]$ formation in Si-doped material in the same temperature region comes from deformation experiment [78]. For our post growth annealing at 950 °C we assume that the $\text{Si}_{\text{Ga}}\text{V}_{\text{Ga}}$ -complex starts to dissociate again. Then, the Ga-vacancy performs a hindered diffusion (as indicated in figure 37) – being temporarily retrapped at other Si-atoms and released again afterwards. Ga-vacancies originally trapped in a zone around a dislocation could participate in the formation of As-precipitates at the dislocation. This would result in a reduction of $\text{Si}_{\text{Ga}}\text{V}_{\text{Ga}}$ -complexes (acceptors) and a corresponding increase of Si_{Ga} (donors) within a zone extending from the dislocation as far as the hindered diffusion of the Ga-vacancies allows. By spectral photoluminescence indeed an increase of Si on Ga-sites has been observed [53]. This model would be consistent with the following findings:

- (i) The denuded zone is formed along dislocations segments which are also being decorated by As-precipitates. This is shown in Fig. 35 but it is particularly evident for the two examples in figure 38. In the figure 38c, the decoration of the dislocation is interrupted for about 25 μm . The cylindrical shape of the denuded zone around the dislocation changes into half spheres at both ends of the interruption obviously determined by the influence of precipitates. In figure 38a the precipitates are too far apart to form a continuous cylindrical zone; the denuded zone is shaped spherically around each precipitate.

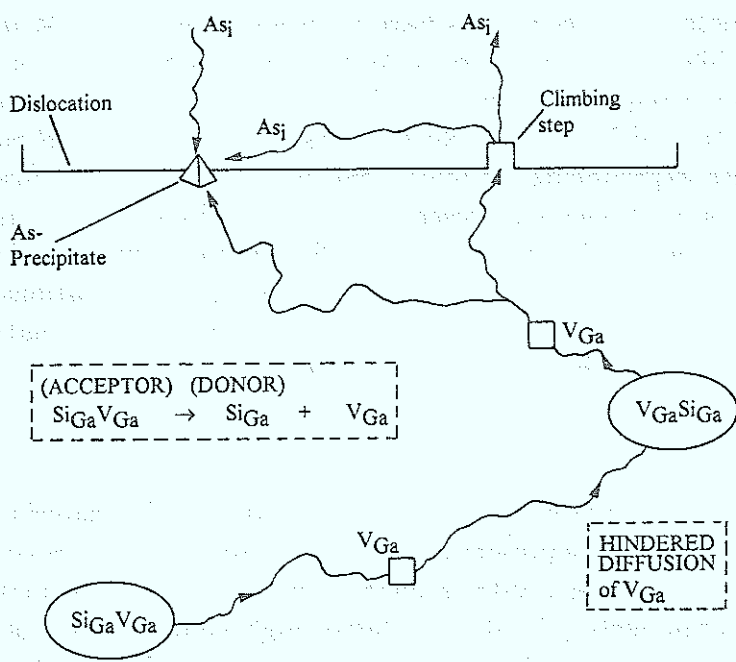


Fig. 37: Redistribution of donors and acceptors in Si-doped material by dissociation of Si_{Ga}V_{Ga}-complexes, hindered diffusion of V_{Ga} and formation of As-precipitates and climb processes at dislocation.

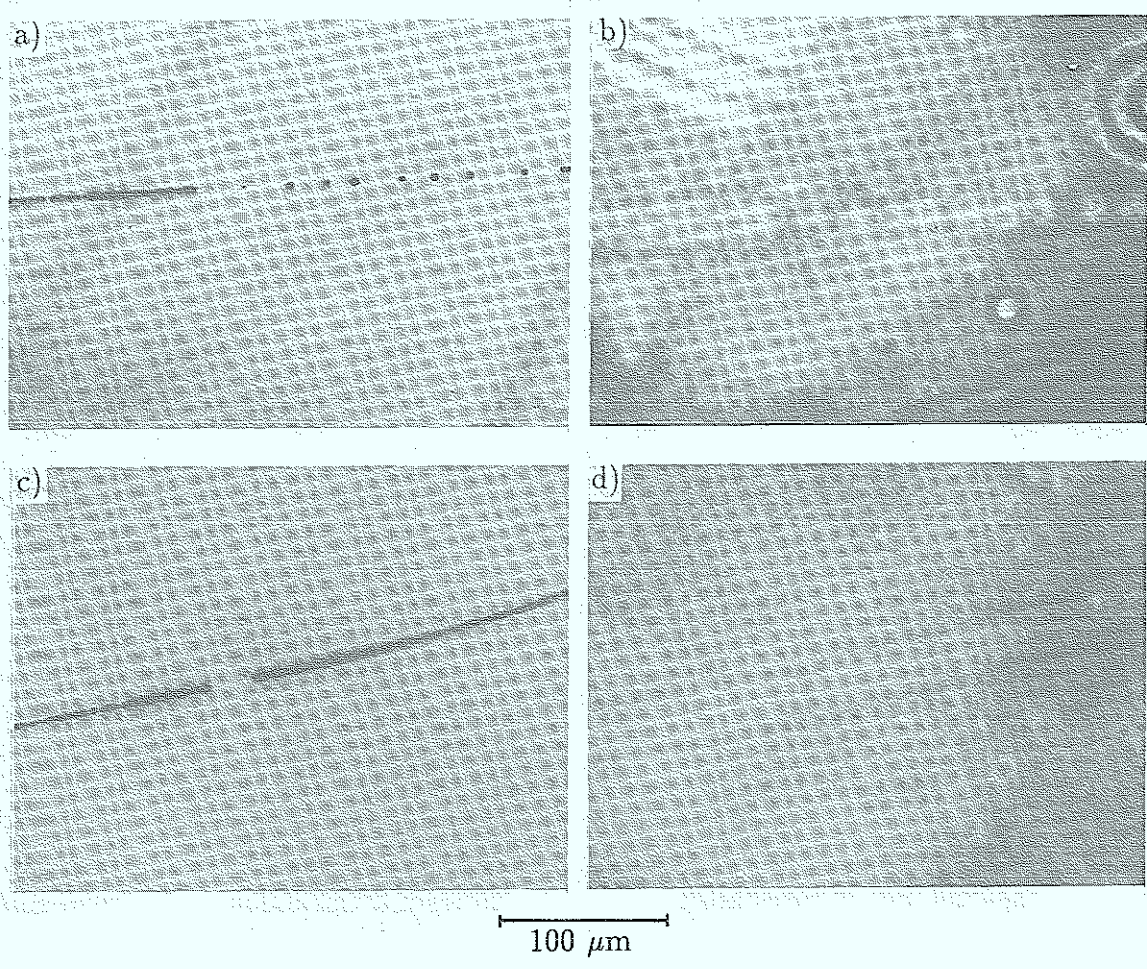


Fig. 38: Comparison of darkfield- (a), c)) and phase microscopy (b), d)) images of Si-doped material after post growth annealing at 950 °C for about 50 hours.

- (ii) If the dislocation density is very low, i.e. if the dislocations are far apart we also observe the formation of matrix precipitates (DF-image) and denuded zones around each individual precipitate, if the material received a post growth annealing treatment at 950 °C for about 50 h. A reduced etching rate and a bright phase contrast (Fig. 39c) is found, within the denuded zone showing that the free carrier concentration is increased. This result indicates that the proposed defect mechanism (fig. 37) can operate under favourable circumstances also in the matrix.

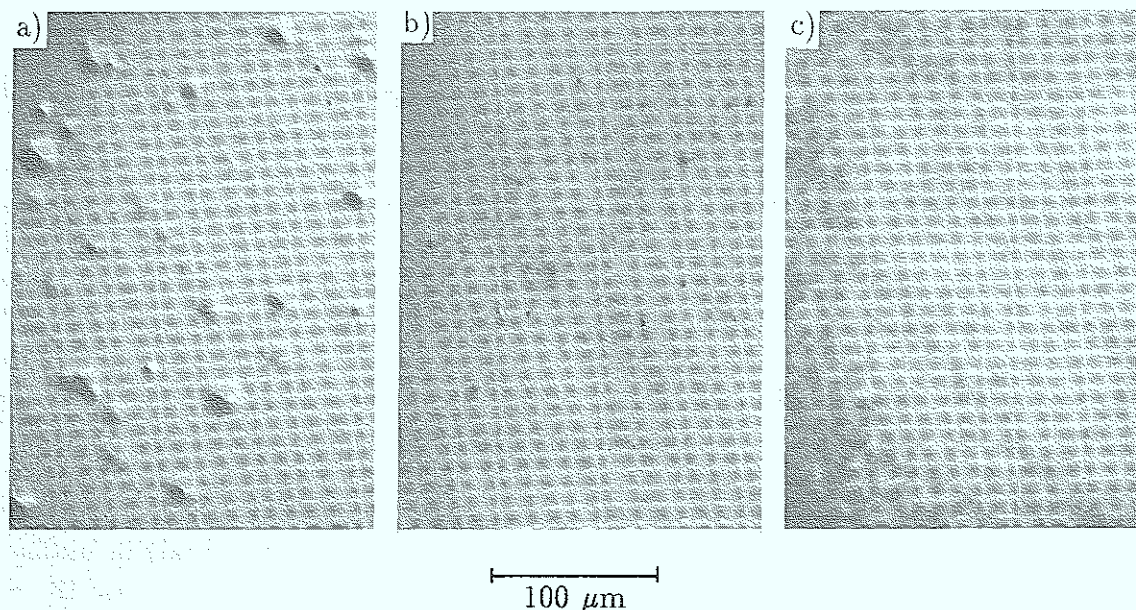


Fig. 39: Comparison of darkfield- b), phase microscopy- c) and differential interference contrast (DIC) image a) of matrix precipitates and their associated denuded zone. The DIC-image a) was taken from a photoetched surface, whereas the other two b), c) from inside the sample.

- (iii) If all Ga-vacancies extracted from the denuded zone are only participating in the formation of As-precipitates we can estimate the size of these precipitates from the increase in donor concentration measured by EBIC to about 10^{17} (cm^{-3})

$$\Delta \bar{n} (\text{cm}^{-3}) \left(\frac{d^2 \cdot \pi}{4} \right) \cdot \Delta d = 4 \cdot 10^{22} (\text{cm}^{-3}) \cdot 0.12 \cdot l^3 \quad (17)$$

where $d \approx 30 \mu\text{m}$ is the diameter of the denuded zone, $\Delta d \approx 3 \mu\text{m}$ the average distance between As-precipitates (tetrahedral shape) and l the size of the tetrahedron. Although we don't know the size of the precipitates since the calibration of the darkfield method is yet not completed, $l \approx 0.35 \mu\text{m}$ estimated from equation (17) appears as a reasonable value⁸. In particular since this is an upper limit, because Ga-vacancies may also react with the dislocation itself to generate a positive climbing steps, which would be associated with the formation of As-interstitials and this in turn may help to grow As-precipitates more readily along dislocations than in the matrix (see also (vi)).

⁸The precipitates after 50 h anneal at 950 °C in Si-doped GaAs appears (judged by the scattered light intensity) somewhat larger as those usually observed in undoped as grown material. TEM sample from undoped material reveal As-precipitates of $\approx 0.3 \mu\text{m}$.

- (iv) The growth of the denuded zone appears to be controlled by a diffusion process as already discussed. In the present model this must be interpreted as a hindered diffusion, for which its temperature dependence is determined by the dissociation of the Ga-vacancy from the Si-atom, i.e. the migration energy of the Ga-vacancy is much smaller than the dissociation energy. The preexponential factor is then determined by the concentration of Si-atoms.

$$D \approx \frac{\nu}{N_{\text{Si}}^{2/3}} e^{-\frac{E_{\text{Diss}}}{kT}} \quad (18)$$

Only very preliminary data on the temperature dependence of the diffusion coefficient are yet available. At 850 °C after 50 h no measurable growth of the denuded zones could be observed, whereas at 1010 °C the diffusion constant is roughly 7-times as large as at 950 °C (see next section). From these very limited data we can estimate a dissociation energy $E_{\text{Diss}} \lesssim 3.0$ eV. Further experiments will be necessary to obtain an accurate value for E_{Diss} . It should be noted, however that the temperature range for measuring E_{Diss} is very limited (probably only ≈ 120 °C wide) because as shown later additional defect mechanisms seem to dominate already at 1070 °C (see next section). The estimated value of ≈ 3.0 eV for the dissociation energy is much higher than the migration energy of Ga-vacancy [79] and therefore confirms our assumption that the Ga-vacancy will perform a hindered diffusion. It also confirms the experimental results that As-precipitates are formed much more readily (they are present in as grown material) in undoped material than in Si-doped GaAs (only after > 40 h at 950 °C), because the diffusion of Ga-vacancies is not hindered by temporary trapping at Si-atoms. It should be noted, however, that the formation of As-precipitates occurs still in the same temperature range (900–1000 °C) for both materials.

- (v) The formation of As-precipitates is not sufficient for forming a denuded zone which is visible by phase microscopy or which exhibits a reduced etching rate. The Si-concentration must be high enough to provide a sufficient increase of donors (figure 37). This explains – as shown in figure 62m – why the denuded zones are only visible by phase microscopy or photo-etching at the tail end of the crystal, where the Si-concentration is sufficiently high due to macrosegregation. Denuded zones become visible for $n_{\text{Si}} \gtrsim 1 \cdot 10^{18} \text{ cm}^{-3}$.
- (vi) As we will show in detail in the next section glide processes of dislocation have been observed in Si-doped material due to thermal stresses generated during the cooling process of the crystals after its growth is completed. Upon gliding the dislocation unlocks from the denuded zone leaving it behind as a “fingerprint” of its own original position and configuration. Two examples are shown in figure 33c, d). After annealing at 950 °C for 10 h the denuded zone of the dislocation (in its final position (a) grows as described at the beginning of this section. The “fingerprints” of its earlier position widens in diameter with vanishing contrast. After another 40 h annealing time the “fingerprints” are disappeared completely (see figure 40). This result is somewhat surprising because on the basis of our model we would expect that the formation of a denuded zone is correlated with the formation of As-precipitates though they may be too small to be detected.

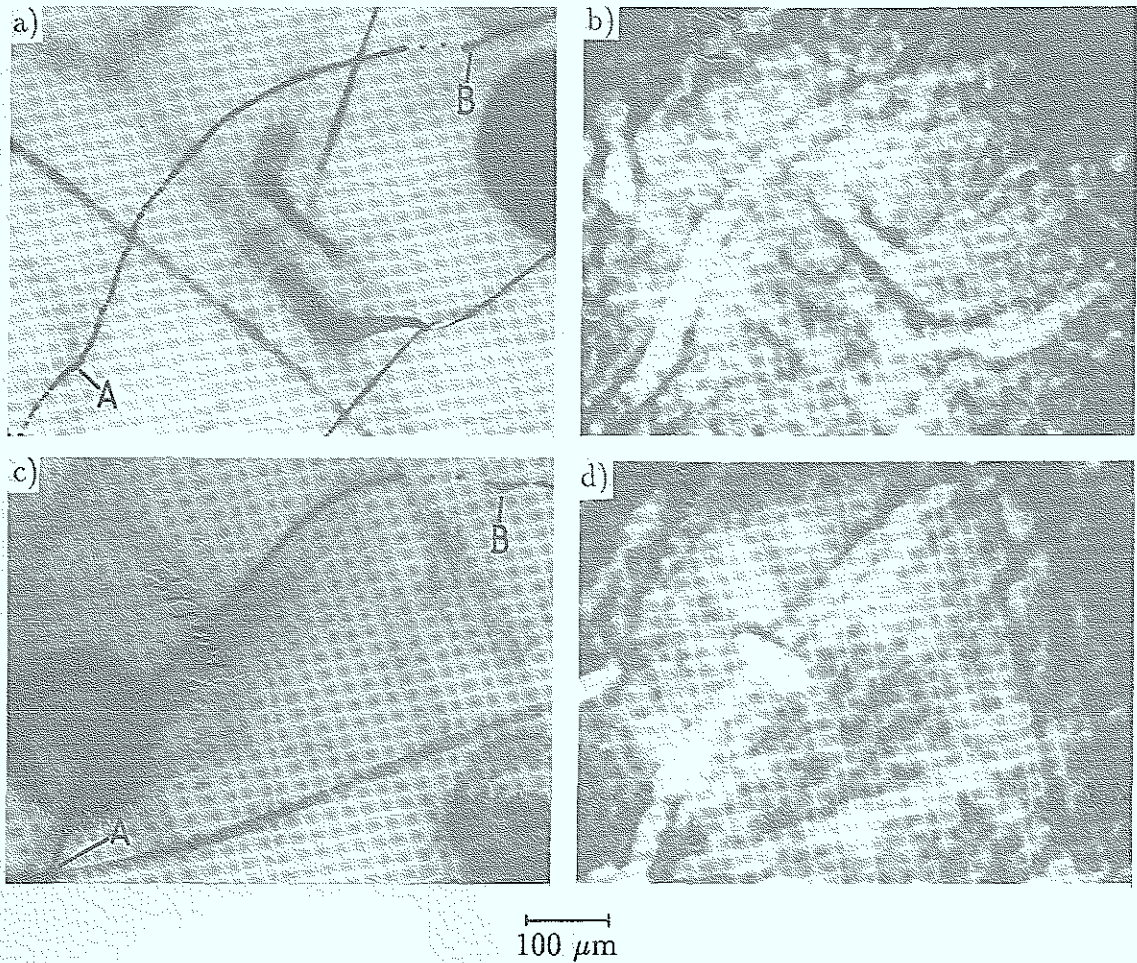


Fig. 40: Phase microscopy b) d) - and darkfield images a) c) of dislocation segments (AB) which were subject to glide processes during the cooling of the crystal. The material received a post growth anneal at 950 °C for about 50 h.

If the dislocation breaks away the As-precipitates left behind would be expected to grow further since we also observe the growth of matrix defects, i.e. growth without the presence of dislocations. Although we do not know the mechanism causing this result, the presence of a dislocation may have a supporting influence to nucleate and to grow As-precipitates (as indicated earlier in (iii)). It should be noted that the present model also allows the formation of denuded zones (less Ga-vacancies, more Si-donors) even without the formation of As-precipitates by a positive⁹ climb of the dislocation. The relation between the diameter of a denuded zone formed by this mechanism and the distance a dislocation would have to climb to absorb sufficient Ga-vacancies is given by

$$d = 3.5 \cdot 10^7 \sqrt{\frac{x}{\Delta \bar{n}}} \quad (16a)$$

i.e. if the dislocation climbs by $x = 10^{-4}$ cm a denuded zone of $d = 10^{-3}$ cm could be formed with $\Delta \bar{n} \approx 10^{17}$ (cm⁻³).

⁹A very detailed TEM-analysis presented in ref. [71] shows that positive climb can be observed much more often than negative climb (emission of Ga-vacancies or absorption of As_i-interstitials). This result, however, is in contradiction to an assumption which is often made in the literature that the excess arsenic is mainly present as As-interstitials.

Material from other sources: Si-doped material grown by the LEC-method has also been subjected to a long time annealing treatment at 950 °C. The as grown material shows also no As-precipitates and similar to our material denuded zones around dislocation exhibiting a bright contrast ($\Delta n < 0$) in phase microscopy. Upon annealing the denuded zone grows in diameter and precipitates are forming along dislocation, however smaller in size and number. More experiments are required to study the similarities or differences between Si-doped GaAs grown with LEC and VB-technique, respectively.

b) Si-doped: Growth kinetics of the denuded zone

In part a) of this section we already discussed the time dependence of the growth of the denuded zone at 950 °C. In this part we will briefly describe a few preliminary results on the temperature dependent growth.

- (i) 850 °C: After a 10 h anneal no growth of the denuded zone could be detected within our error margins, i.e. $\approx 2 \mu\text{m}$. From this value we can roughly estimate a lower limit of $\approx 3.0 \text{ eV}$ for the activation energy of the process when comparing the upper limit of $3 \mu\text{m}$ with the extension of the denuded zone of the 950 °C anneal.
- (ii) 950 °C: These data have already been discussed in part a) of this section.
- (iii) 1010 °C: After a 5 h anneal the denuded zone has grown the about $20 \mu\text{m}$ (see Fig. 41) in diameter.

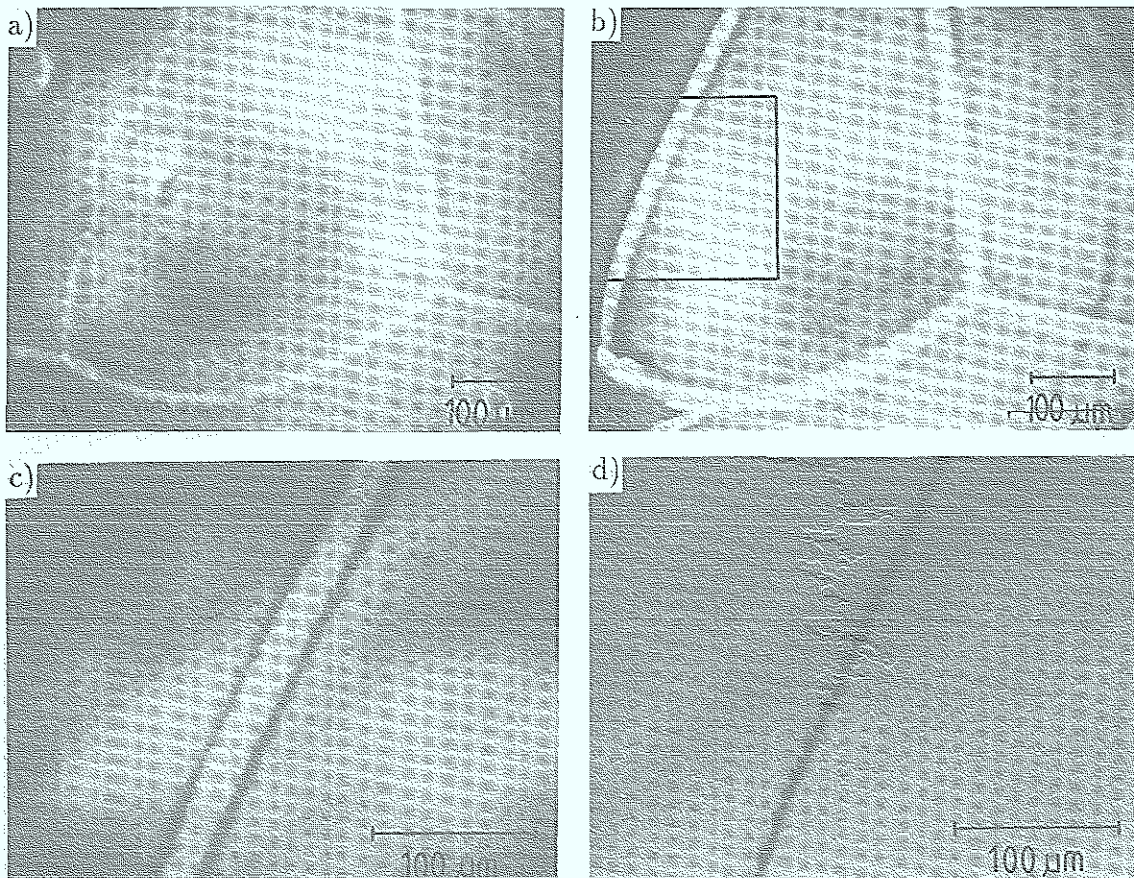


Fig. 41: Phase microscopy image of identical samples areas of a) as grown material b, c) (insert in b corresponds to figure c) after 5 h anneal at 1010 °C. Darkfield image d) was taken after annealing.

Comparing this with the growth rate of the denuded zone at 950 °C an activation energy of about 3.0 eV can be estimated. If the growth process is described by a hindered diffusion of the Ga-vacancy, the dissociation energy of the defect complex, $\text{Si}_{\text{Ga}}\text{V}_{\text{Ga}}$ must be identified with this activation energy. Although there are no reliable data available for the migration energy, the values from literature [79] are much smaller than 3.0 eV. This confirms our assumption that the diffusion process of the Ga-vacancy is only determined by the dissociation from the Si-atom. In this case the diffusion coefficient for the hindered diffusion is given by equation (18).

- (iv) 1070 °C: The result of this annealing treatment cannot be employed for determining the activation energy. The phase microscopy image after annealing indicates that additional or other defect mechanisms must operate than those at lower annealing temperature. The zone around the dislocation exhibits a dark center contrast with a very faint (not visible in figure 42b but vaguely in 42c) bright contrast extending to about 40 μm in diameter. Due to its higher sensitivity to small variation in the free carrier concentration, the zone structure can be imaged much more clearly by photo-etching. Corresponding to the result of the phase contrast the surface profile after photo-etching shows a deep depression within of a broad hillock (100 μm in diameter). The defect mechanism responsible for the observed variation is not known.

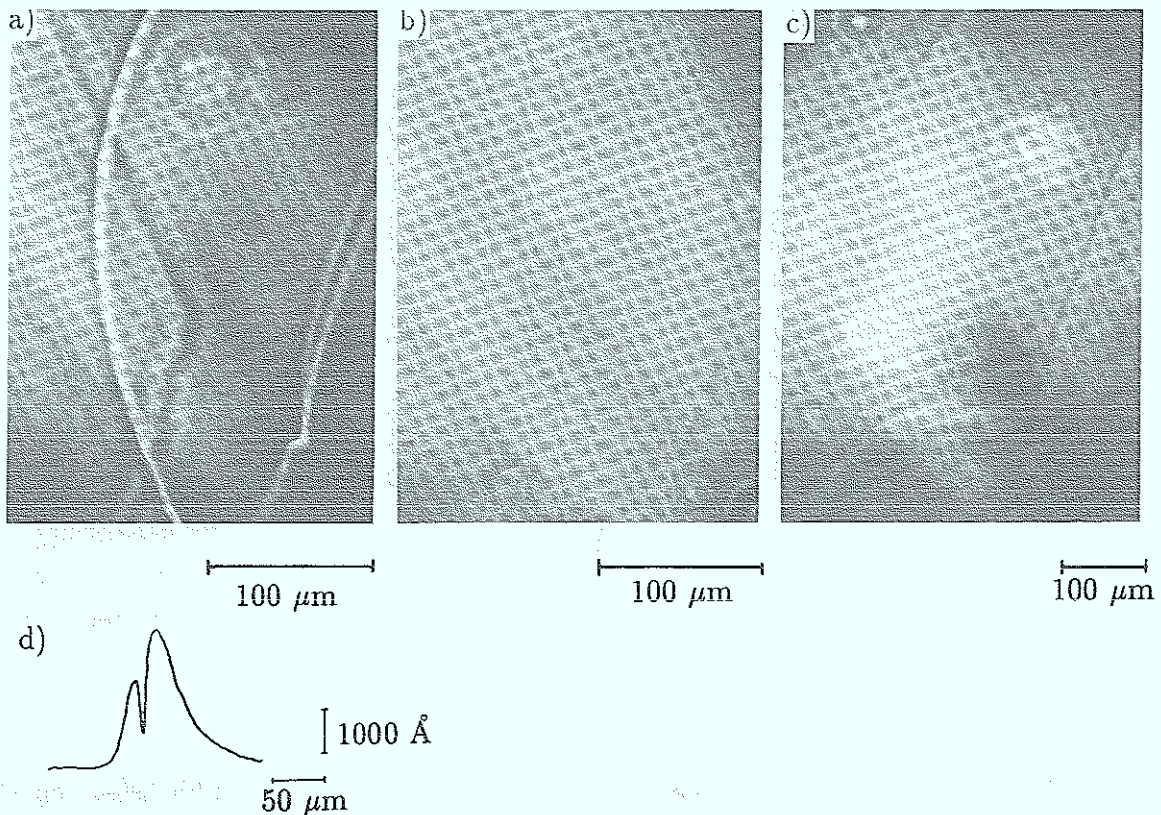


Fig. 42: a) and b) are phase microscopy images comparing identical areas of the grown material and that which had been annealed for 1 h at 1070 °C; c) different area after annealing exhibiting vaguely a bright zone around the dislocation; d) surface profile of a photoetched surface after annealing.

c) *Si-doped: 1100 °C + 950 °C:*

The material first received a 10 h annealing treatment at 1100 °C and, after fast cooling to room temperature, the sample was again annealed for 10 h, at 950 °C. After the first anneal the material does not exhibit any phase contrast around the dislocations. It is interesting that in some parts of the sample decoration precipitates are formed along dislocations (see figure 43b) at a temperature as high as 1100 °C, although it is a well known fact that at such temperatures As-precipitates are being already dissolved in undoped material [80, 81, 82]. It appears that As-precipitates in Si-doped samples are more stable at higher temperatures. Further experiment are currently performed to understand this effects.

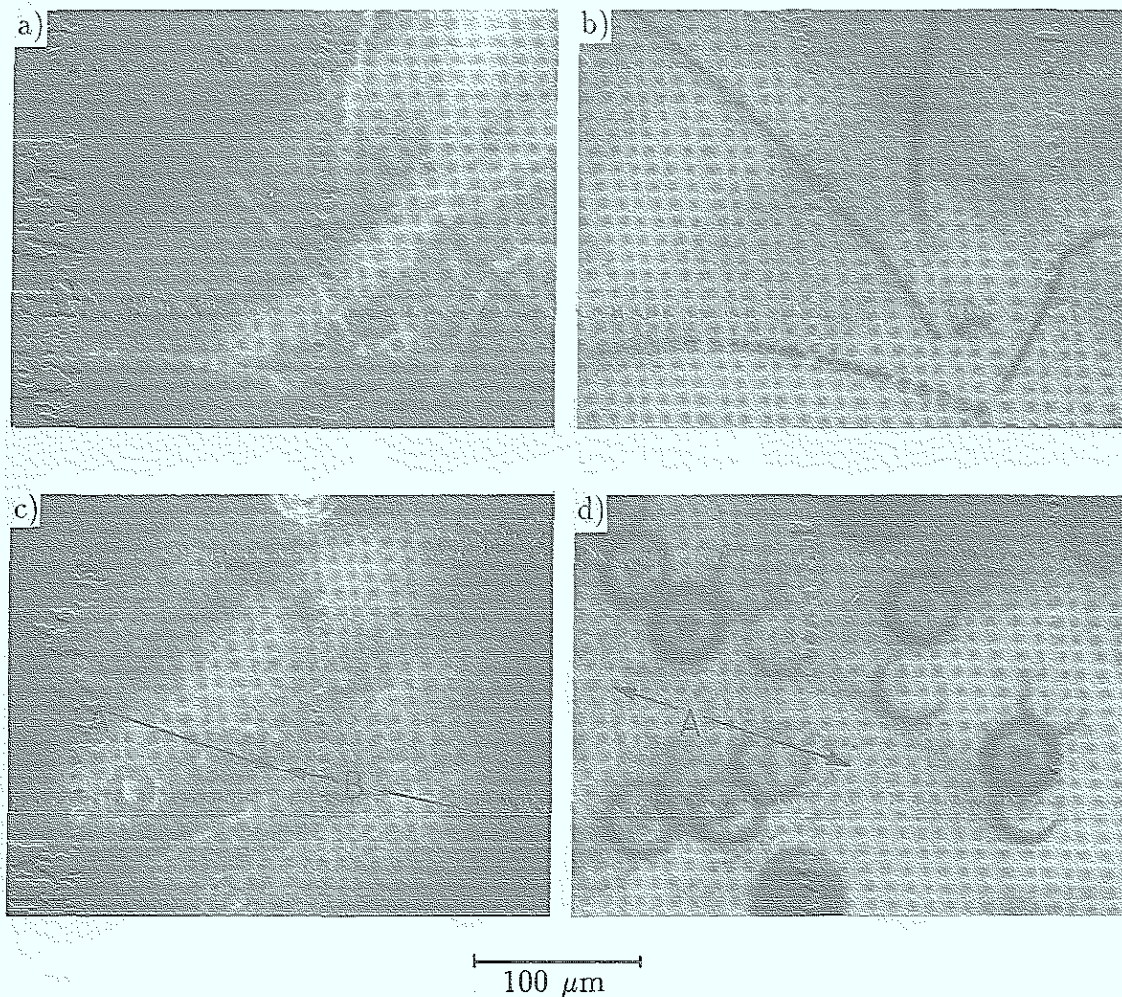


Fig. 43: The phase microscopy images (a, c) of the denuded zone and darkfied images (b, d) of the same area after the 950 °C annealing treatment.

The subsequent annealing treatment at 950 °C for 10 h has no visible effect on the decoration precipitates, i.e. if additional precipitates are formed along dislocations they are probably too small to be seen. The phase microscopy images, however, do exhibit again a bright contrast around dislocations indicating that the dissolution and formation of the denuded zones in this material is reversible (figure a, c). The denuded zones are formed at all dislocations, those which were decorated during the annealing

treatment at 1100 °C with visible As-precipitates and those which were not. Figure 43d (DF) shows a dislocation segment which was only partially decorated during the 1100 °C anneal (A). During the subsequent annealing treatment at 950 °C – because it lasted only for 10 h (see part a) of the section) – no additional precipitates become visible, whereas the denuded zone is formed along the whole length of the dislocation segment A and B. In terms of our model we must conclude that the hindered diffusion of Ga-vacancies is so fast at 1100 °C that their concentration is homogeneous across the material including the region around the dislocations. A subsequent annealing at 950 °C again forms a denuded (lower concentration of V_{Ga}) zone around the dislocation visible in the phase contrast due to the associated increase of donors in this zone.

d) Si-doped (grown from Ga-rich melt): 40 h at 950 °C

As already discussed in section 3.1.2 the defect structure around dislocations in the material is different to that observed in Si-doped material, which was grown from nearly stoichiometric melts. We find a reduction of the free carrier concentration around the dislocation because the phase microscopy shows a dark contrast (Fig. 44a) and photo-etching (Fig. 44e) an increased etching rate. In the same area photo-etching resolves microstructural defects probably due to microprecipitates (see figure 29b). Further away from the dislocation we observe a broad halo (bright) but the photo-etching rate remains high. A consistent model to explain this complex result has not yet been found. Annealing results could not clarify the observations.

The center phase contrast (Fig. 44b) is much darker after annealing than before annealing. This indicates that the free charge carrier density has decreased further. Considering EBIC-measurements this is surprising, since the free carrier concentration close the dislocation is as low as $\bar{n} \lesssim 5 \cdot 10^{16}$ already for as-grown material [9], i.e. a further decrease in \bar{n} should not be visible in phase microscopy. Outside the dark phase contrast a very faint bright contrast extending to about 40 μm from the dislocation can be detected. This can be correlated to a broad ($\approx 40 \mu\text{m}$) hillock in the photoetched surface (figure 44f). The increased etch rate in the center of the hillock corresponds to the dark contrast in figure 44b, which is similar figure 42b (As-rich Si-doped material after annealing at 1070 °C). Comparing figure 44b and 44d we must conclude that the decoration precipitates even for “Ga-rich” material are growing during the annealing treatment at 950 °C, although the decoration precipitates are of the arsenic type as indicated by photo-etching (see also discussion in section 3.3.3).

e) Si-In-codoped:

Si-In codoped material in the as-grown state exhibits a very similar microstructure as Si-doped GaAs. Upon annealing at 950 °C, however the material behave very different. The microstructure developing is comparable to that found in Si-doped material when annealed close to 1100 °C.

f) Other annealing studies:

Annealing has also be performed on undoped and Te-doped samples. They will be discussed in section 3.2.4. We have also studied the thermal stability of variations in the doping concentration due to growth striations (see section 3.2.3).

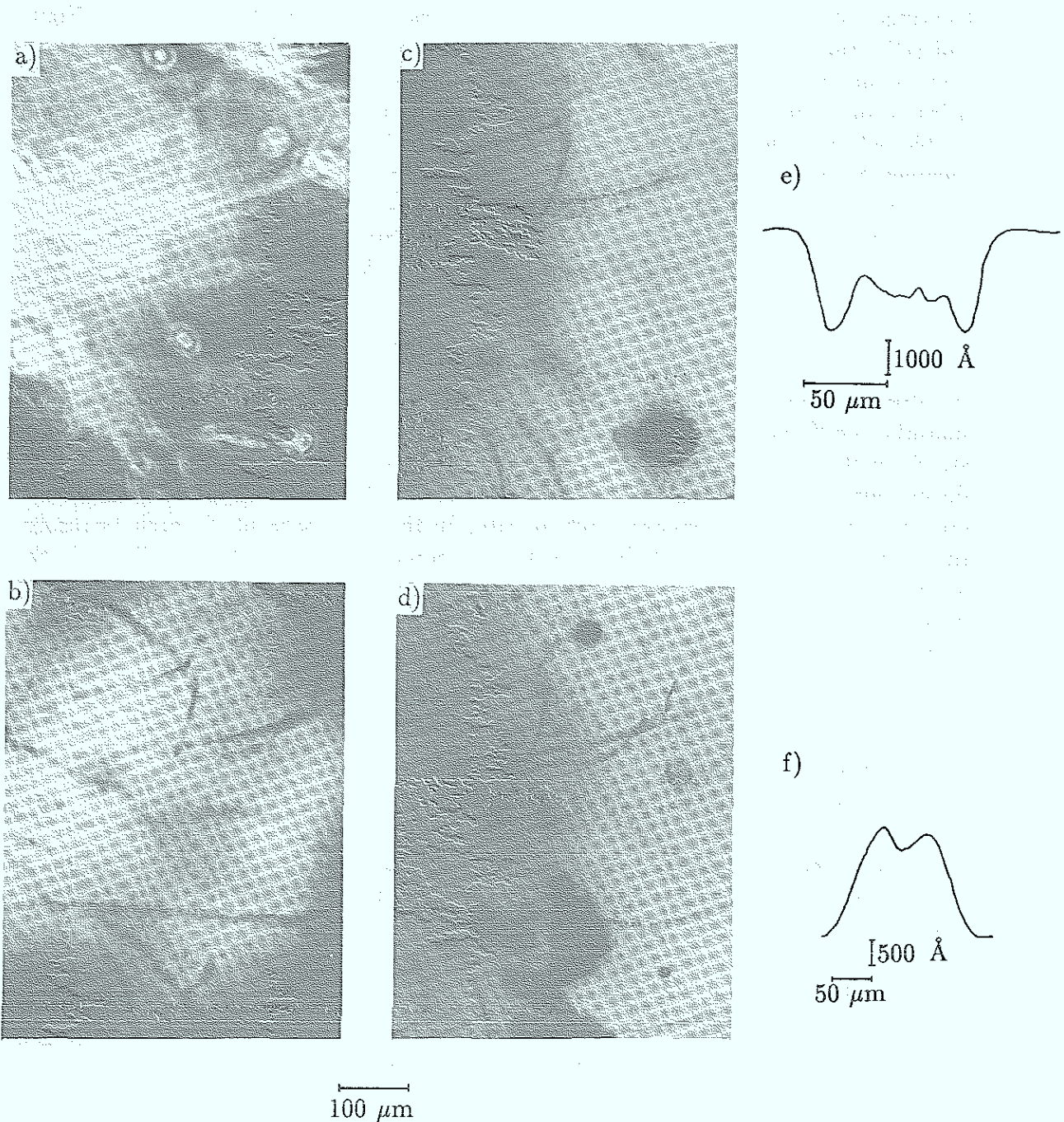


Fig. 44: Comparison of a phase microscopy a), b) – and darkfield image c), d) for “Ga-rich” material. e), f) Surface profile around a dislocation after photo-etching (Note: a, c, e for as grown material, b, d, f after 950 °C annealing; a, b, c, d show identical sample areas).

3.2.2 Glide processes during cooling of the crystal

It has been shown by photo-etching studies [83] that in Si-doped material dislocations are subject to glide-processes during the cooling period which follows the crystal growth. These glide-processes are probably caused by thermal stresses. Crystal grown in the present work by VB-methods also show these effects, however usually only in the last (tail end) third of the crystal. Gliding of dislocation in Si-doped material can be

detected by photo-etching because defects interacting with dislocation cause changes in the electrically properties in the surrounding of dislocation. This means that the gliding traces of the dislocation can be made visible. Some examples for these traces are shown in figure 45. They must be identified as intersection lines of glide planes with the sample surface, i.e. we can easily determine the type of gliding planes which are operative. Comparing figures 45f, 46b with the photoetched (110) and (100) surface it is evident that – in agreement with the literature – most gliding actions take place on (111)-planes. Fig. 45a, however also shows a different type which can be identified as a (113)-plane (Fig. 45e). Hornstra [84] has shown that $[112]$ -dislocation lines on (113)-slip planes have a $\frac{a}{2} [110]$ -Burgersvector in zinkblend lattices (see also [85]).

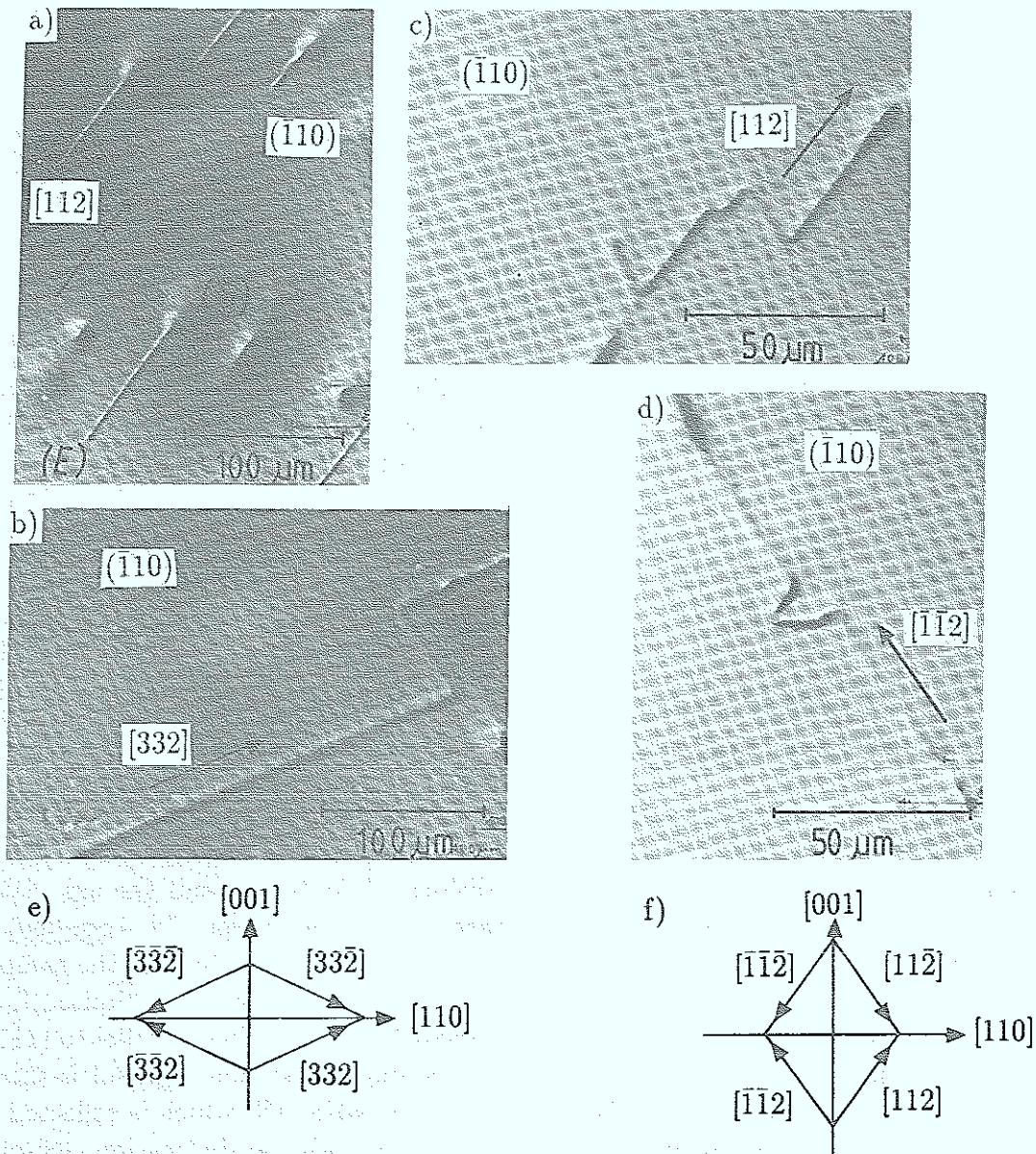


Fig. 45: a), b), c), d), DSL-etched surface (110) of Si-doped sample, cut from the crystal parallel to the growth direction $[001]$. e) Intersection of (113)-planes with the $(\bar{1}10)$ -surface of the sample. f) Intersection lines of (111)-glide planes with a $(\bar{1}10)$ -surface.

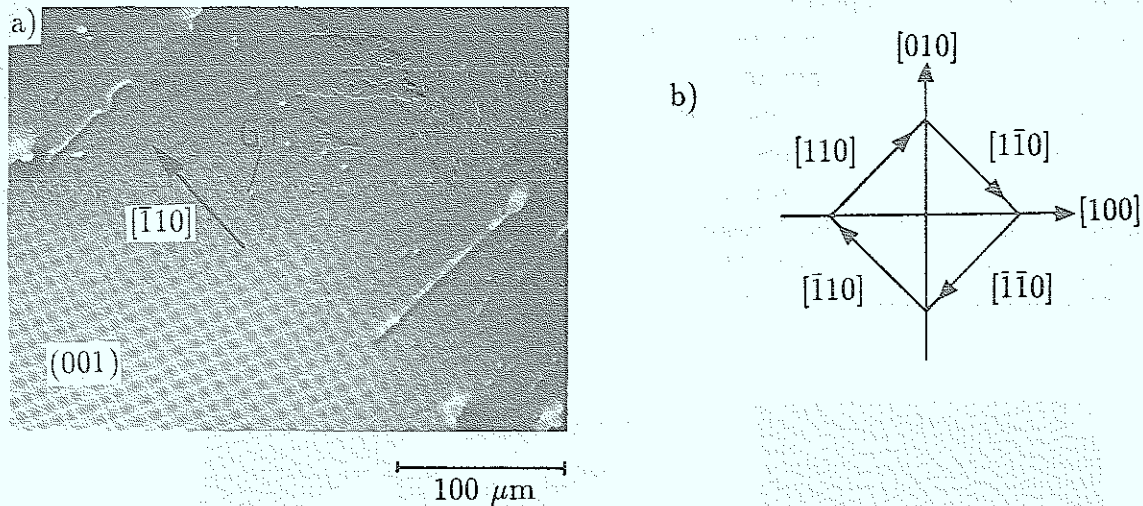


Fig. 46a): DSL-etched surface (100) of Si-doped sample, cut from the crystal parallel to the growth direction [001]. b) Intersection lines of (100)-glide planes with a $(\bar{1}10)$ -surface (GT = Glide trace).

Since the dislocation outcrop exhibits a very pronounced etching profile (needle shaped hillock) on the surface the starting (S) and the final position (E) of the dislocation can be easily distinguished (Fig. 45a). The denuded zone around the starting point (S) is much broader than that around the final position, indicating that the temperature of the crystal when the gliding process takes place is already too low to form large zones. From the annealing results presented in the previous section this temperature must be about or somewhat below 950 °C.

The continuous traces shown in Fig. 45 and 46 indicate that the gliding action of the dislocation also must be a continuous steady motion. In some cases the gliding motion is interrupted i.e. the dislocation is resting at intermediate positions, where it also forms denuded zones around it. As a result the gliding trace resembles a row of hillocks along the gliding path of the dislocation. This implies that the thermal stresses probably vary during the gliding action.

In contrast to photo-etching which only sees dislocation outcrops and the associated denuded zones on the surface of the sample phase microscopy can provide complementary information about the dislocation and its denuded zone in the bulk of the sample. Since most dislocations glide along the (111)-planes and because of the limited focal depth of the microscope several samples were prepared with a surface parallel to (111)-planes. One example is seen in figure 47 in which a long dislocation segment is shown in its final position (E) after gliding from its starting position (S) which is reflected by the broad denuded zone acting as a "finger print" for the original dislocation. (Similar gliding processes were shown in figure 33c, d.) After the dislocations has reached its final position only a very small denuded zone is formed. As already discussed this may be due to a then presumably low temperature of the crystal. Small denuded zones are also often observed for intermediate positions as e.g. shown in figure 33c (see also figure 51).

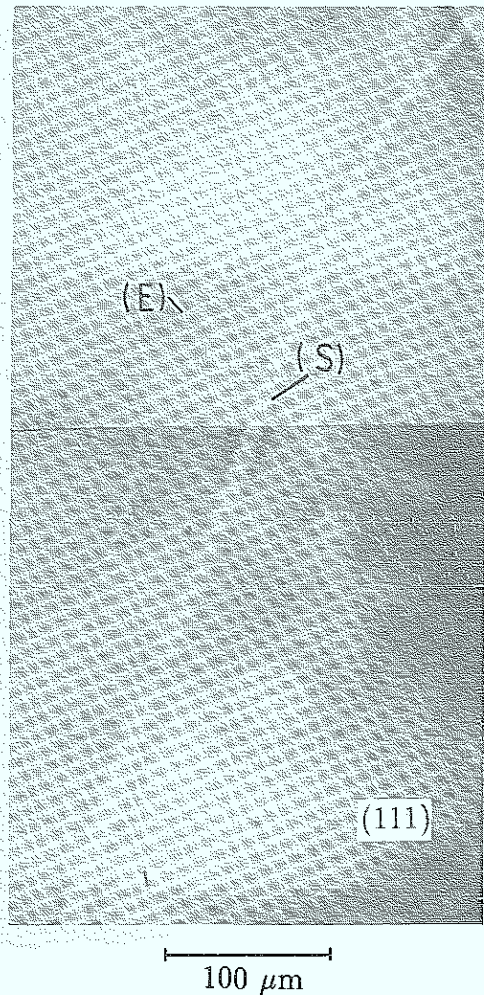


Fig. 47: Phase microscopy image of Si-doped material. The sample surface was prepared parallel to a (111)-plane. (S) original position, (E) final position of the dislocation.

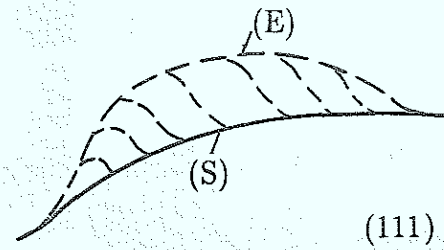


Fig. 48

Assuming that the dislocation segment gets unlocked from its original position more or less simultaneously along its whole length, the stress required to initiate the gliding process may be estimated from the curvature of the dislocation which reflects its line tension. An alternative mechanism is indicated in figure 48. The dislocation breaks away locally and by extending laterally the dislocation would also reach the same final position [86]. This unlocking mechanism would require a much higher initial stress than reflected by the final curvature of the dislocation. Considering intermediate glide positions as e.g. shown in figure 33c and 51 this mechanism appears rather unlikely. Calculating the stress from the curvature of the dislocation (the relation between both will be discussed in section 3.3 in more detail) we obtain values of approximately 0.03 MPa. It is interesting to compare this value with critical resolved shear stresses (CRSS) of GaAs, which are determined by the yield points of the stress-strain curves by multiplying with the appropriate Schmidfactors. The CRS-stress characterizes the onset of plastic flow [77] and is roughly 1 – 2 MPa for GaAs in the temperature region of 1000 – 1400 K. It should be noted that the yield point is the result of the multiplication of grown in dislocation rather than the result of dislocations being unlocked, e.g. from “Cottrell” atmospheres. Unlocking stresses have been measured for Si-doped GaAs by I. Yonenaga et al. [87] but only for relatively low temperatures ($\lesssim 550$ °C). They found that the stresses required to unlock dislocations are much higher (two orders of magnitude) than those we estimated from the curvature of the dislocation line. Although the unlocking of dislocations is a thermally activated process and as a result we expect the unlocking force to decrease with temperature, it is not clear whether this

can account for the decrease of two orders of magnitude. For a comparison the drop of the critical-resolved shear stress between 500 and 950 °C is much smaller (factor 2 to 3). It should be noted that the small values of the present work are based on the assumption that the thermal stresses are determined by the line tension of the dislocation, which may not be justified. The arrest of the dislocation at its final position may simply be caused by a temporary reduction in the thermal stress.

In figure 49 some results are presented which are typical for Si-doped LEC-grown material. The sample (a commercial wafer polished on both sides) has a (100)-surface and the image has been taken in a region of low dislocation density. The image shows the projection of dislocations which reach from one surface of the sample to the other.

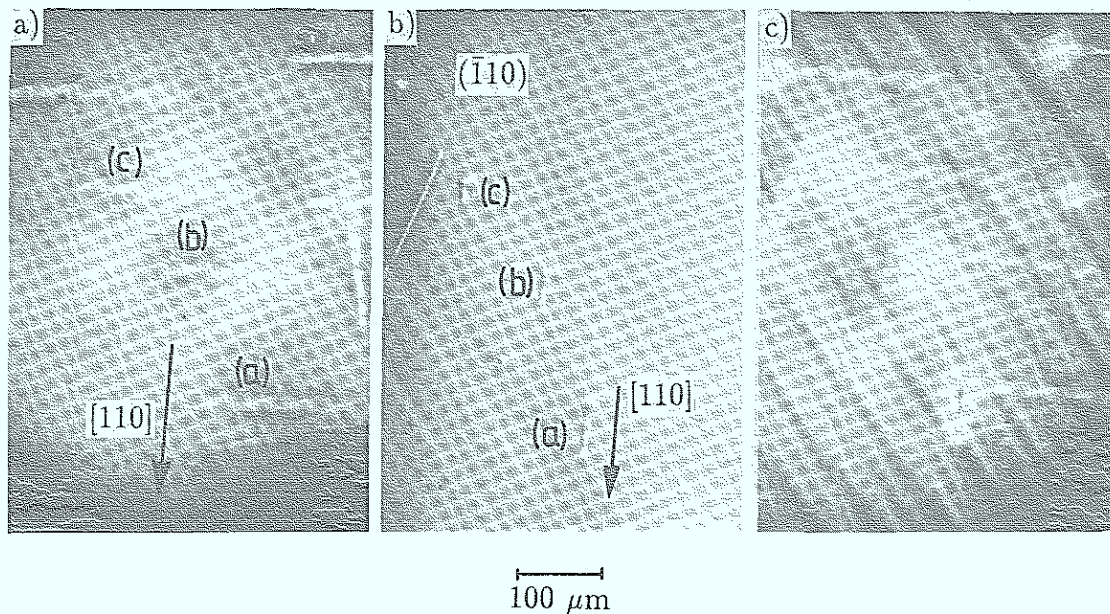


Fig. 49: a) Phase microscopy image of a Si-doped LEC-Wafer with a (100)-surface (before photo-etching), b) Differential interference contrast of the photoetched surface (identical area as a)) c) Phase microscopy image after photo-etching¹⁰.

Their projection is parallel to [110]-direction and they are gliding on (111)-planes, because the point of intersection with the surface (see dislocation (a)) moves parallel to [110]-direction. The direction of the glide trace can be seen more clearly after photo-etching the surface (see figure 49b). A dislocation with a line vector of [112] is consistent with these result and the length of the projection if compared with the thickness of the sample also agrees with this assumption. Dislocations with a line vector of $\vec{u} = [112]$ lying on a (111)-glide plane probably have an Burgers vector $\vec{a} = \frac{1}{2} [1\bar{1}0]$. Although it is not possible to get a clear cut answer about the type of dislocations from IR-images from these purely geometrical considerations we can obtain a well founded guess nevertheless. The dislocations shown in figure 50 can be "identified" this way as a dislocation with $\vec{u} = [110]$, $\vec{a} = \frac{1}{2} [011]$ on (111)-plane.

¹⁰The surface profile after etching is also visible in a phase contrast. An elevated area is seen as a dark contrast for a small elevation and the contrast is inverted for larger elevations (see figure 53). The growth striations observed in this figure are due to the photoetched surface profile. In figure a) striation cannot be seen, because for a (100)-wafer they are almost parallel to the surface of the sample.

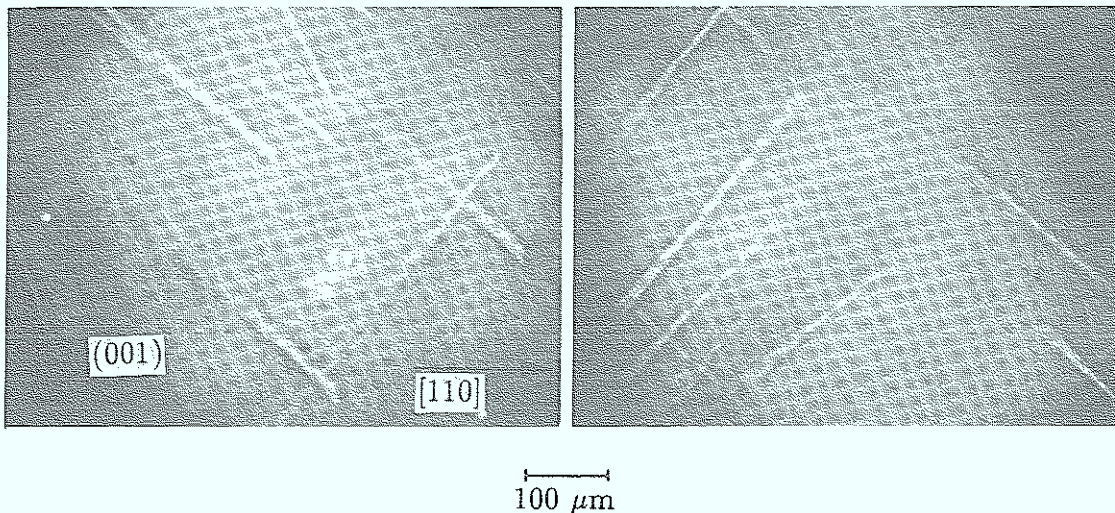


Fig. 50: Phase microscope image of a Si-doped LEC-wafer with a (100)-surface.

The dislocations a, b in figure 49b were subject to an interrupted (“stop and go”) glide process as compared to the continuous glide motion shown in figure 45. A clearer version of a “stop and go” motion is given in figure 51. From its original position (a) the dislocation moved to its final position (g) stopping at the 5 intermediate positions (b), (c), (d), (e), (f). The denuded zones left behind at intermediate positions are small and exhibit a contrast which is not as strong as for the starting and final position.

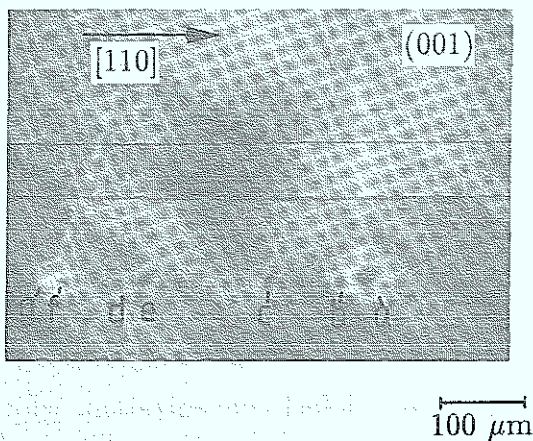


Fig. 51: Phase microscope image of a Si-doped LEC-wafer with a (100)-surface. For discrimination continuous and “stop and go” glide motion the surface was photoetched. Since the focal depth is much smaller than the thickness of the sample, the image was composed of 3 pictures focussed at different depths of the sample.

As shown in figures 45 and 46 often several glide planes are part of the gliding trace. It is not clear whether this is due to cross gliding processes or whether dislocation segments located on intersecting slip planes perform a simultaneous glide process (the latter would imply that all segments have the same Burgersvector.). Employing phase microscopy we can image the glide trace on a photoetched surface (see footnote 9 on page 52) as well as the associated dislocation. The result shown in figure 52 and 53 supports the interpretation by dislocation segments lying on intersecting glide planes, because the configuration of the glide trace resembles very nicely that of the dislocation. Since the dislocation is connected to both end points of the gliding trace, we may assume that the glide trace indeed is generated by the dislocation segments seen in figure 52 and 53.

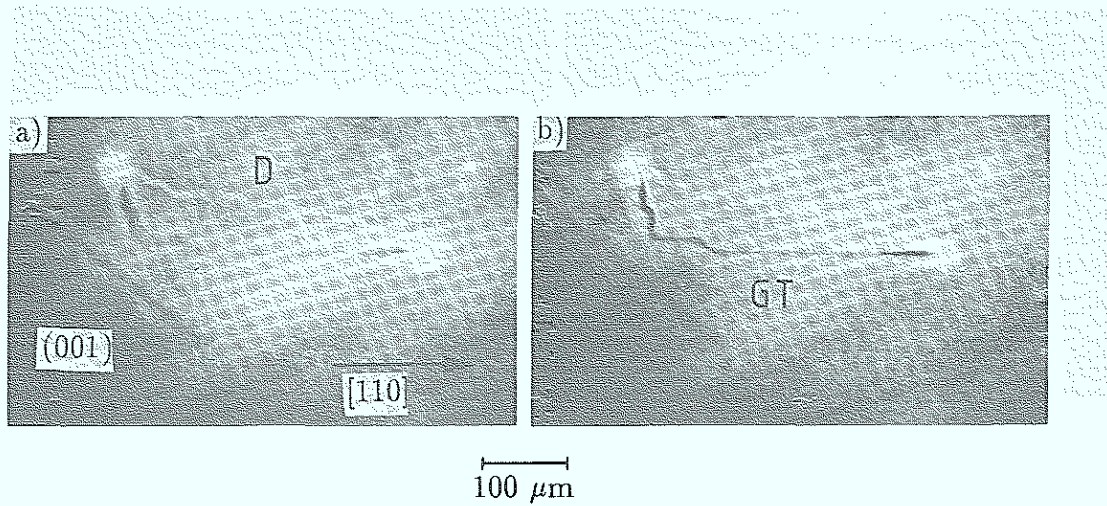


Fig. 52: Phase microscope images of a Si-doped LEC-wafer with a photoetched (to reveal glide traces) surface: a) focussed on the dislocation, D b) focussed on the glide trace, GT.

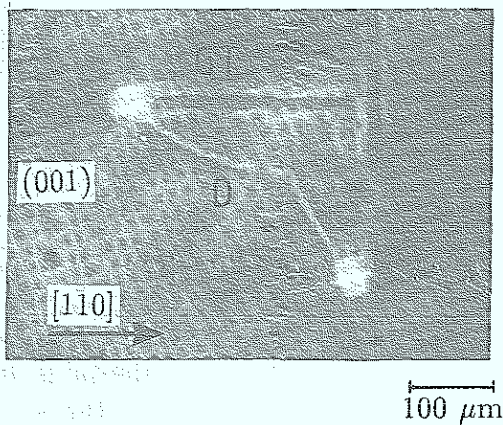


Fig. 53: Phase microscope images of a Si-doped LEC-wafer with a photoetched (to reveal glide traces, GT) surface.

3.2.3 (i) Growth Striations

Growth striations are inhomogeneities in the doping and defect concentration, which are in some cases comparable to those found in the vicinity of dislocations. The scale of the lateral variation of these inhomogeneities is similar in both cases. Therefore, growth striations should generate similar problems for the performance of electronic devices as dislocations. This has been confirmed by a Y. Fujisaki and Y. Takano [6] who studied the relationship between fluctuations in the MESFET threshold voltage, V_{th} , and the striation pattern.

Methods used for studying dislocations and their surroundings have also been employed for growth striations, i.e. Photo-etching [88, 89, 90], Infrared microscopy [40, 91, 92, 93, 94] and X-ray topography [e.g. 94, and 96]. In spite of this large effort to investigate growth striations a number of problems remain unresolved, a few of which shall be addressed in this section.

As briefly outlined earlier the interpretation of IR-images of growth striations, particularly if they are used for a quantitative determination of doping inhomogeneities, is very questionable. This is mainly due to the uncertainty which of the optical properties absorption, refractive index n or gradients in n are responsible for the image contrast. A.F. Witt [40] considers absorption effects as dominant, whereas in ref. [91, 92] evidence is presented that gradients in the refractive index are causing the image contrast of growth striations. For a quantitative assessment it is also important to know whether the correct absorption thickness of the growth striations is given by the thickness of the sample (this assumption was made in ref. [40]) or roughly by the focal depth of the optical imaging system.

In section 3.1 we have shown that bright field contrast as well as phase microscopy images are only sensitive to relative large variations ($\gtrsim 5 \cdot 10^{16} \text{ cm}^{-3}$) in the free carrier concentration \bar{n} (i.e. this technique cannot be used for undoped samples) and that absorption contrast due to $\Delta\bar{n}$ is always negligible as compared to refractive index effects. This is evident for phase microscopy by equation (13) in the case of small phase shifts (compare also initial slopes of the contrast versus d in figure 54). For large phase shifts, if $\Delta\bar{n} \gg 10^{17} \text{ cm}^{-3}$ or $d \gg 100 \mu\text{m}$ the relation between absorption contrast and phase contrast is more complicated as shown in figure 54.

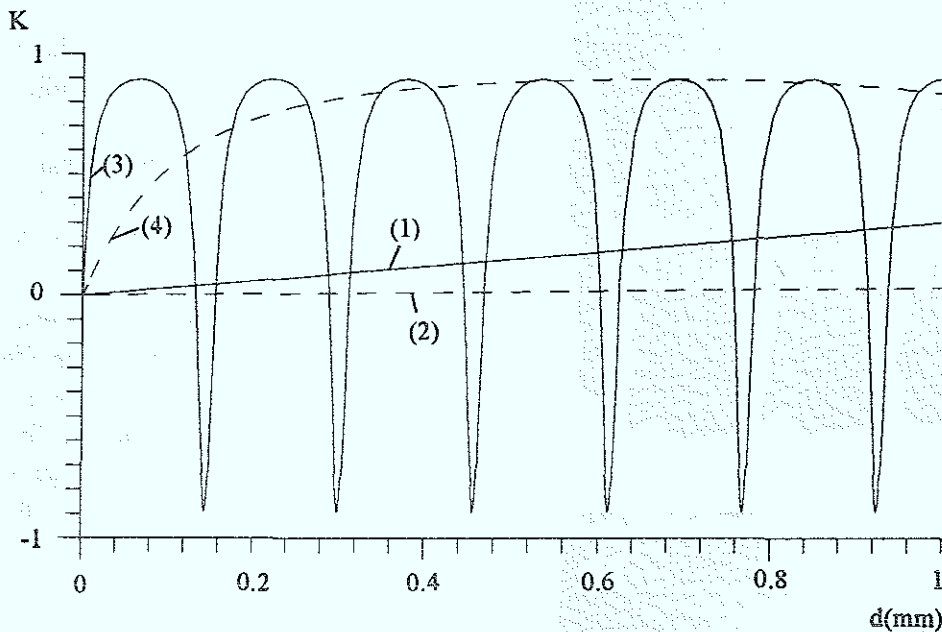
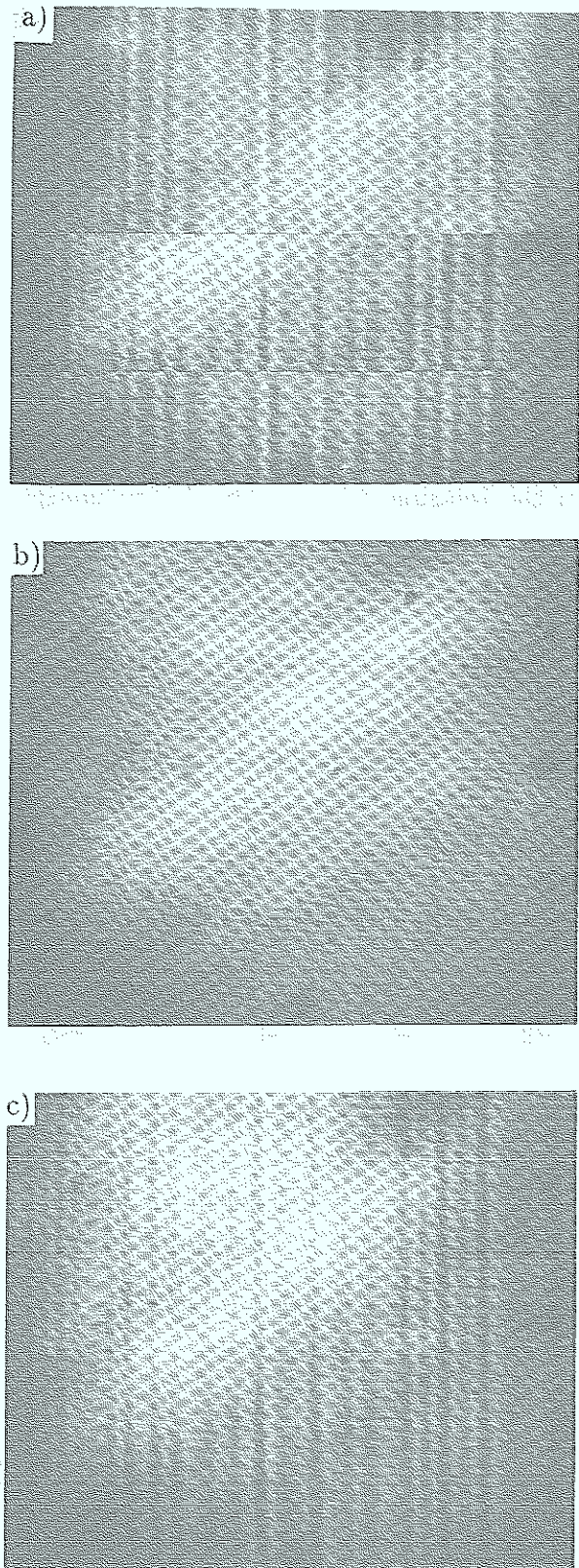


Fig. 54: Absorption- (1) K_α ($\Delta\bar{n} = 10^{18} \text{ cm}^{-3}$), (2) K_α ($\Delta\bar{n} = 10^{17} \text{ cm}^{-3}$), and phase contrast (3) $K_{\Delta n}$ ($\Delta\bar{n} = 10^{18} \text{ cm}^{-3}$), (4) $K_{\Delta n}$ ($\Delta\bar{n} = 10^{17} \text{ cm}^{-3}$) as a function of the variation in the free carrier concentration and the thickness d .

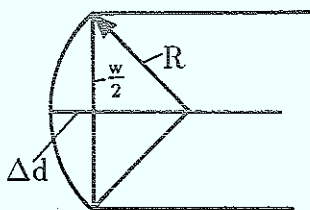
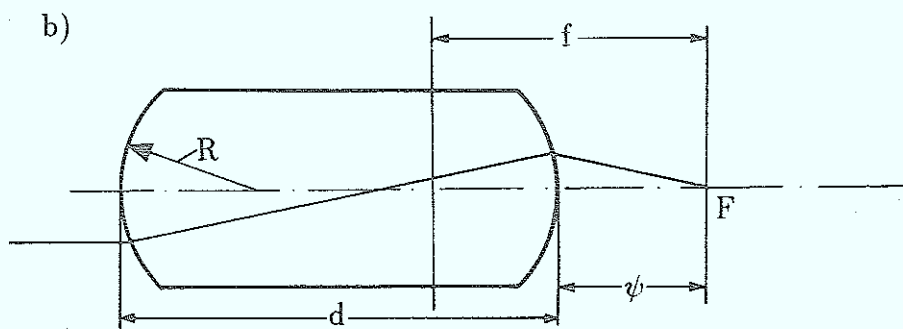
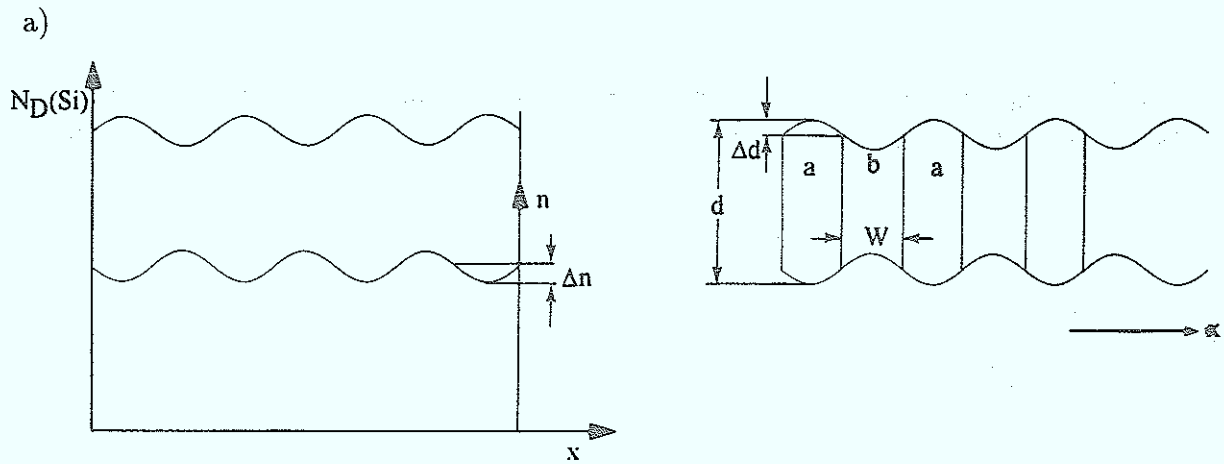
Other complications for assessing IR-images of growth striation are:

- (i) When using a microscope it is difficult to define d : Taking thickness of the sample as proposed in ref. [40] means overestimating d , whereas setting d equal to the focal depth, d_{foc} of microscope may underestimate d .
- (ii) Refractive effects as shown in the following.



To eliminate these complications at least partly relative thin samples ($d = 48 \mu\text{m} \approx d_{\text{foc}}$ and $d = 140 \mu\text{m}$, resp.) have been investigated. As shown in figure 55 the bright field contrast strongly depends on the focussing conditions. A striation pattern is only visible when focussing on a plane slightly in front or somewhat behind the sample. Both images exhibit a complementary contrast as shown by the insert in figure 55a. The contrast vanishes completely when focussing onto a plane in the middle of the sample. This result clearly eliminates absorption effects as a dominant cause for the image contrast; it rather indicates the importance of refractive effects as discussed in section 3.1.1. A periodic modulation of the refractive index—as illustrated in figure 56—may be considered ($\frac{1}{2} \cdot d \cdot \Delta n = n \cdot \Delta d$) as a modulation of the sample thickness, i.e. the sample would resemble a series of cylindrical lenses (figure 56b). Under this assumption we calculated the position of the focal point, F as a function of d for typical parameters of $\Delta n = 5 \cdot 10^{-4}$, 10^{-3} , $3 \cdot 10^{-3}$, 10^{-2} and $W = 10, 15 \mu\text{m}$.

Fig. 55: a), b), c) Bright field images of growth striations in a Si-doped LEC-sample ($d = 140 \mu\text{m}$) for different focussing conditions: a) focussed to a plane about $20 \mu\text{m}$ in front of the upper surface (insert is taken from figure c); b) focussed to the mid plane of the sample; c) $20 \mu\text{m}$ behind the back surface.



c)

$$R \approx \frac{\left(\frac{w}{2}\right)^2 \cdot n}{2 d \Delta n}$$

$$f = \frac{R^2 \cdot n}{N}$$

$$N = (n-1) [2nR - d(n-1)]$$

$$\psi = \frac{R [nR - (n-1)d]}{N}$$

Fig. 56: a) Schematic lateral distribution of the doping concentration and the associated variation of the refractive index; b) Corresponding optical thickness of the sample according to relation $\Delta d = \frac{1}{2} \frac{d\Delta n}{n}$; c) Calculation of the focal length and the distance ψ .

For the cylindrical lens shown in figure 56c a very complex dependence of the focal length and the distance ψ on the thickness of the sample is found, particularly for $d \gtrsim 0.15$ mm (Fig. 57).

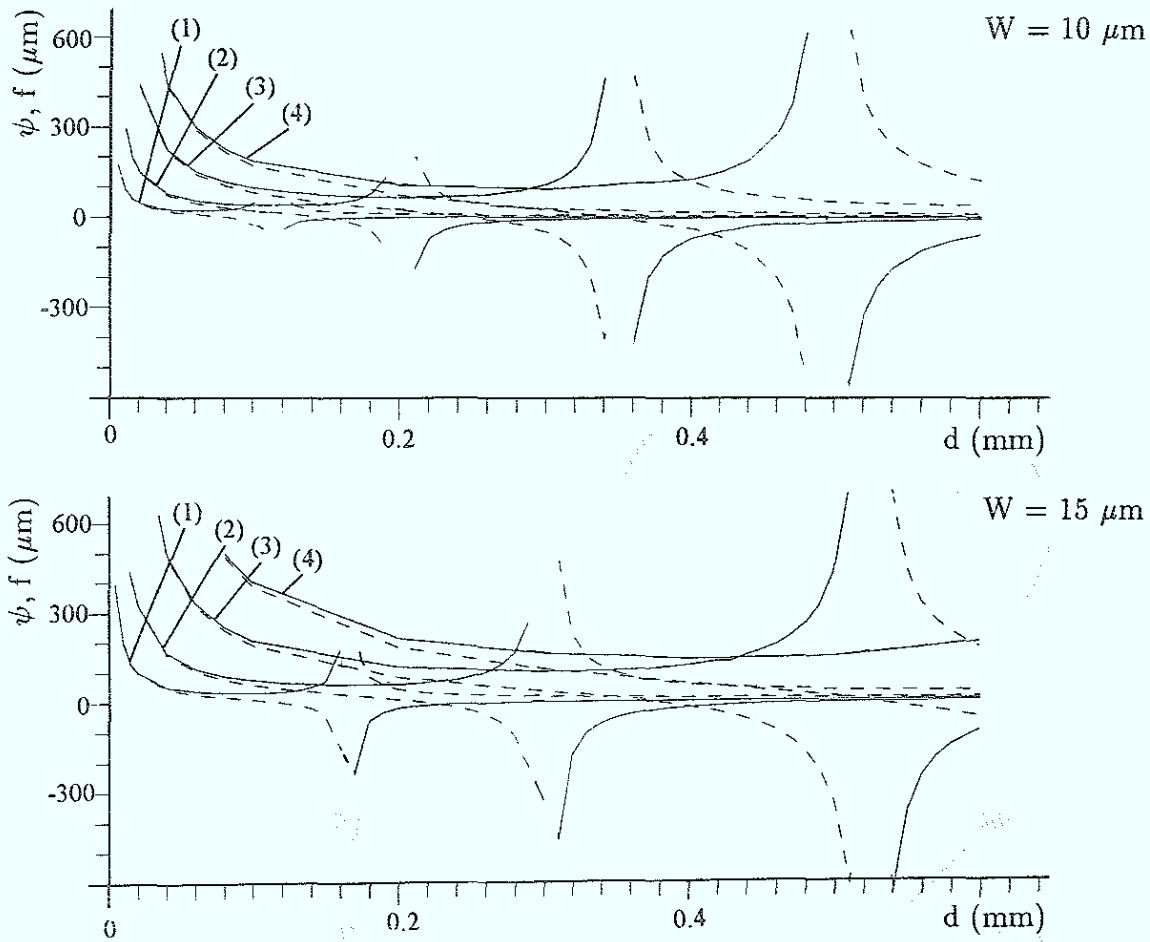


Fig. 57: Focal length and distance of the focal point from the surface of the lens as a function of the thickness d of the sample calculated for different variations in the free carrier concentration and for different widths of the grow striations. Dashed (solid) lines correspond to ψ (f): (1) $\Delta\bar{n} = 10^{-2} \text{ cm}^{-3}$, (2) $\Delta\bar{n} = 3 \cdot 10^{-3} \text{ cm}^{-3}$, (3) $\Delta\bar{n} = 10^{-3} \text{ cm}^{-3}$, (4) $\Delta\bar{n} = 5 \cdot 10^{-4} \text{ cm}^{-3}$

For thin samples typical values 0 to 100 μm are calculated for ψ , which increase with decreasing d . We expect that the contrast of a bright field image due to refractive effects will be largest if the microscope is focussed close to the focal plane (see also

section 3.1.1) of the cylindrical lens. As shown in figure 55 ($d = 140 \mu\text{m}$) and figure 58 ($d = 48 \mu\text{m}$) a high contrast is obtained at distances of $20 \mu\text{m}$ and $60 \mu\text{m}$, resp., consistent with the estimated values of ψ . Therefore we may conclude, that

- (i) the bright field image contrast is mainly caused by refractive effects. This confirms results presented in ref. [92 and 93]
- (ii) the variation in the refractive index due to growth striations is probably between 10^{-3} and 10^{-2} . This corresponds to a variation in the free carrier concentration of roughly $\Delta n = 10^{17} \text{ cm}^{-3}$ to 10^{18} cm^{-3} . Similar values have been found by EBIC in Si-doped samples [90]
- (iii) for thick samples or very large changes of Δn refractive effects are strong and depend on d in a very complex way, making the interpretation of bright field image very difficult. It is, however very likely that bright field contrast is still not dominated by absorption effects.

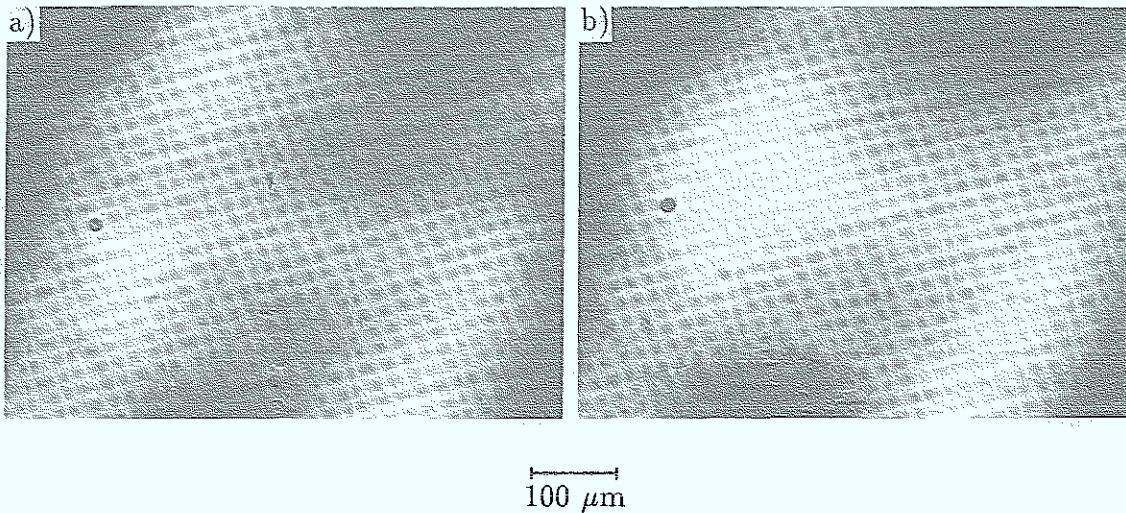


Fig. 58: a), b) Bright field images of growth striations in a Si-doped LEC-sample ($d = 48 \mu\text{m}$) for different focussing conditions: a) focussed to a plane about $60 \mu\text{m}$ in front of the upper surface; b) $60 \mu\text{m}$ behind the back surface.

In figure 59 a bright field image (focussed near the backside of the sample) is compared with phase contrast (a) for the identical area of the sample. Both images agree very well. A striation which exhibits a dark contrast in figure 59b can be described as a converging cylinder lens, i.e. the refractive index in this region is higher than the average value of n (see also discussion in section 3.1.1 on page 19). Under these conditions we expect to find a dark contrast also for the phase microscope image. This is shown in figure 59 (arrows indicate identical sample areas for BF- and Ph.C. images). Also we expect

that refraction effects should influence phase contrast in a similar way as bright field contrast. For thin samples however, the effect is small. The phase contrast image doesn't change as long as the microscope is focussed on planes within the thin sample.

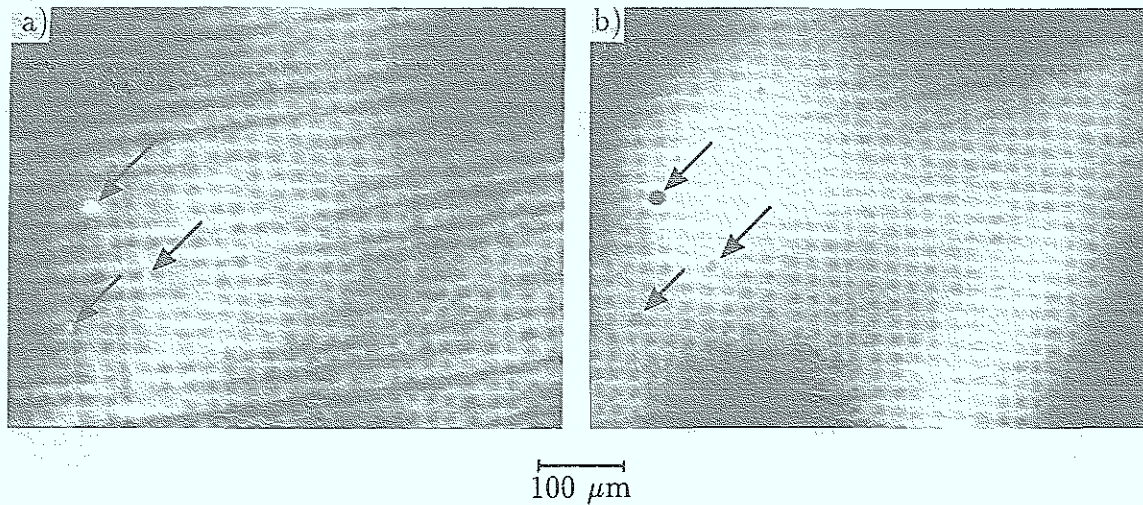
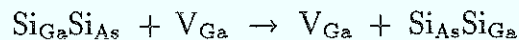


Fig. 59: Phase microscope (a) and bright field (b) image of the same sample area ($d = 48 \mu\text{m}$; the bright field image was obtained by focussing on the backsurface of the sample).

3.2.3 (ii) Thermal annealing of striations:

Annealing of striations in Si-doped GaAs can be used to study the diffusion of Si, which is still a controversial issue in the literature. Among the earlier work the measurements by Greiner and Gibbons [105] are the most detailed studies which also include the determination of the activation energy ($D(\text{cm}^2\text{s}^{-1}) = 0.12 \cdot \exp - \frac{2.5\text{eV}}{kT}$). They proposed that the diffusion under their experimental conditions¹¹ takes place by way of donor acceptor complexes ($\text{Si}_{\text{Ga}}\text{Si}_{\text{As}}$), which can easily move in the GaAs-lattice with a vacancy of either type, e.g.:



A completely different situation may arise if the concentration of Si is too low to form a sufficient number of $\text{Si}_{\text{Ga}}\text{Si}_{\text{As}}$ -pairs. This can be achieved by the so-called δ -doping with Si during MBE-growth of GaAs-layers [see e.g. 98]. Thereby a very thin layer of GaAs is Si doped by about $5 \cdot 10^{18} \text{cm}^{-3}$ [97]. Although the experimental results of measuring the diffusion coefficient for Si by different groups [98–107] are controversial, the most detailed and probably also most reliable data by E.F. Schubert et al. lead to values for the diffusion constant ($D(\text{cm}^2\text{s}^{-1}) = 4 \cdot 10^{-4} \exp \left(-\frac{2.45\text{eV}}{kT} \right)$) which are by 2 to 3 orders of magnitude smaller than determined by Greiner and Gibbons. The diffusing species must be single Si-atoms, since for $[\text{Si}] \lesssim 5 \cdot 10^{18} \text{cm}^{-3}$ all Si incorporated by δ -doping is electrically active and occupies only donor sites.

¹¹The diffusion source used was a 100 Å thick layer of Si on the surface of the GaAs-sample. SIMS and differential Hall measurements of the diffusion zone show that the majority of the diffused Si is present in an electrically inactive form.

Growth striation of Si-doped ($N_D - N_A \simeq 10^{18} \text{ cm}^{-3}$) LEC-grown GaAs crystals are associated with variations in the concentration of electrically active Si-atom between 10^{17} to 10^{18} cm^{-3} . This has been shown by EBIC-measurements which are sensitive to $N_D - N_A$ (see also section 3.2.3(i)). The typical width of growth striation is $\approx 10 \mu\text{m}$. By annealing this material at temperatures sufficiently high to diffuse the Si over distances of $10 \mu\text{m}$ it should be possible to eliminate growth striations and thereby obtaining the diffusion coefficient at that particular temperature. This diffusion coefficient should be representative for a single atom diffusion, since at average concentrations of 10^{18} cm^{-3} Si-donor-acceptor pairs will be hardly present and because the analyzing technique (phase microscopy) employed is only sensitive to electrically active Si-atoms. Figure 60 shows the relation between the annealing temperature and - time required for a diffusion length of $10 \mu\text{m}$ calculated for two different diffusion coefficients representing single atom - and donor-acceptor pairs diffusion, respectively.

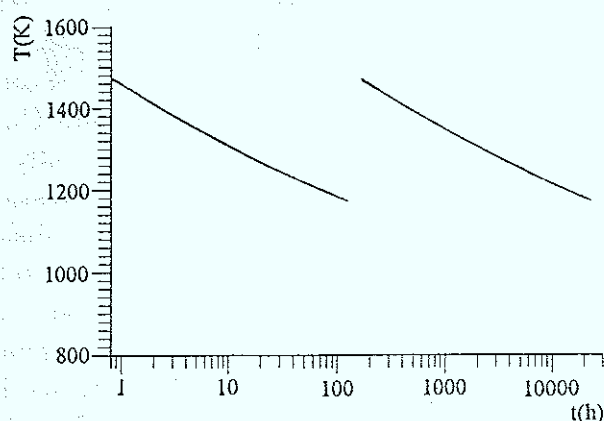


Fig. 60: Relation between annealing time and - temperature for a diffusion length of $10 \mu\text{m}$. (The different diffusion coefficients are taken from ref. [105] and ref. [98], resp.).

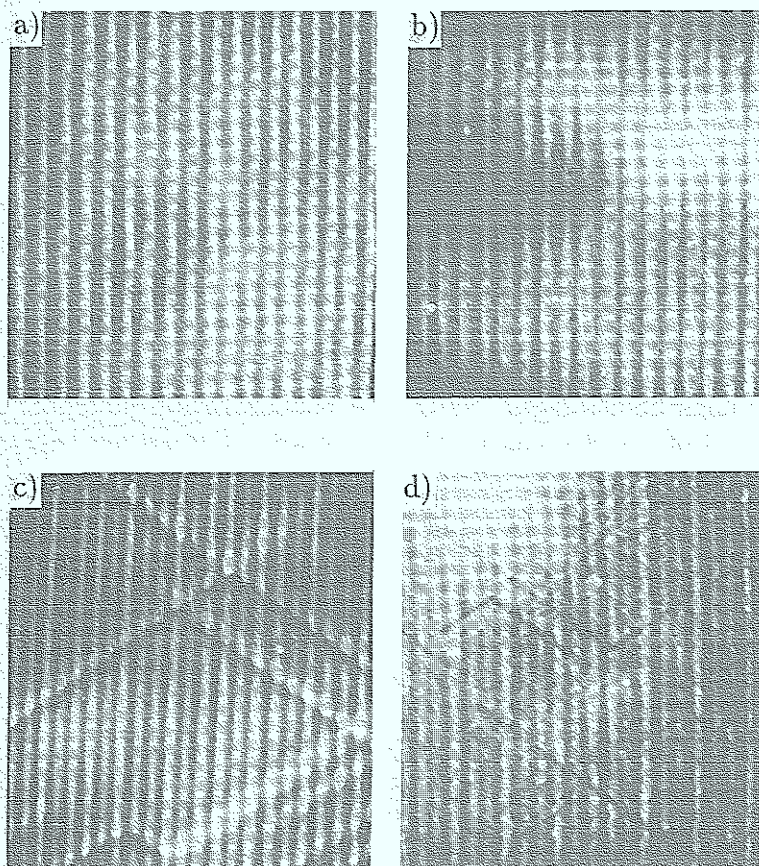


Fig. 61: Phase microscope images of growth striation in Si-doped LEC-grown GaAs
a) before; b) after 20 h at $1150 \text{ }^\circ\text{C}$; c) before; d) after 70 h at $1150 \text{ }^\circ\text{C}$.

In figure 61 growth striations are shown before and after annealing at $1150 \text{ }^\circ\text{C}$. From the fact that even after an annealing time of 70 h we still observe striations we may exclude the large value of the diffusion coefficient in figure 60.

100 μm

3.2.4 Te-doped GaAs

In contrast to Si-doped material the surrounding of dislocation in Te-doped GaAs is characterized by a reduction in the free carrier concentration as compared to the matrix. This has been measured by energy dependent EBIC-measurements [55] and follows also from the photo-etching profile showing an increased etching rate around the dislocation (see figure 27) and from phase microscopy image (e.g. figure 27) exhibiting a dark contrast. The reduction of the free carrier concentration may be attributed to the fact that precipitates (presumably Ga_2Te_3 see section 3.1.1) are formed in the zone of increased etching rate and dark phase contrast. On the other hand EBIC- and CL-measurements reveal an additional zone surrounding that seen by photo-etching and phase microscopy which exhibits a further reduction in the free carrier concentration. This discrepancy is not yet understood. Considering only EBIC and CL-results an interpretation is given in ref. [55] based on the assumption that electrically inactive $\text{Te}_{\text{As}} - \text{V}_{\text{Ga}}$ complexes are formed in both zones and that the Te-concentration is increasing in the inner zone due to the interaction of these impurities with the dislocation. It is very unlikely that the $\text{Te}_{\text{As}} - \text{V}_{\text{Ga}}$ complex is electrically inactive (see ref. [108]) and as shown in section 3.1.2 an increase of the impurity concentration at a distance of about $5 \mu\text{m}$ from the dislocation appears to be impossible. Also this model does not explain photo-etching and phase microscopy results. It is difficult to see how this discrepancy could be resolved, but it seems necessary to compare - in a first step - the different techniques for the same material and even for identical sample areas to make sure that the same effect is studied by all techniques. In the course of the present work this was not possible, we will therefore limit the following presentation to a description of the experimental result obtained with phase microscopy and photo-etching.

(i) *axial dependence of the defect structure in a Te-doped crystal (Fig. 62a-f):*

Due to macrosegregation [109] the Te-concentration is rather inhomogeneous as indicated by the values of the free carrier concentration along the growth axis which have been determined by resistivity and Hall effect measurements. The defect structure in the cone area of the crystal is very similar with that of undoped material (see next section), i.e. dislocations decorated with As-precipitates which are visible in the dark field images. As the Te-concentration increases the number of decoration precipitates decreases. Almost no microdefects are revealed by darkfield or by phase microscopy in the middle of the crystal. Birefringence images however revealed a similar density of dislocation as formed in the cone area and the tail end of the crystal. Towards the end of the crystals, if the free carrier concentration exceed values of about 10^{18} cm^{-3} the dislocation structure becomes visible again in phase microscopy images. With further increasing carrier concentration the phase contrast intensifies. As a comparison with Si-doped material the axial dependence of the defect structure as seen by phase microscopy and DF-contrast is shown in figure 62g...m. The Si-concentration increases along the growth axis due to macrosegregation to similar values as observed for the Te-doped GaAs shown in figure 62a...f. Also the dislocations in the cone area are decorated by As-precipitates, no decoration can be seen for intermediate doping

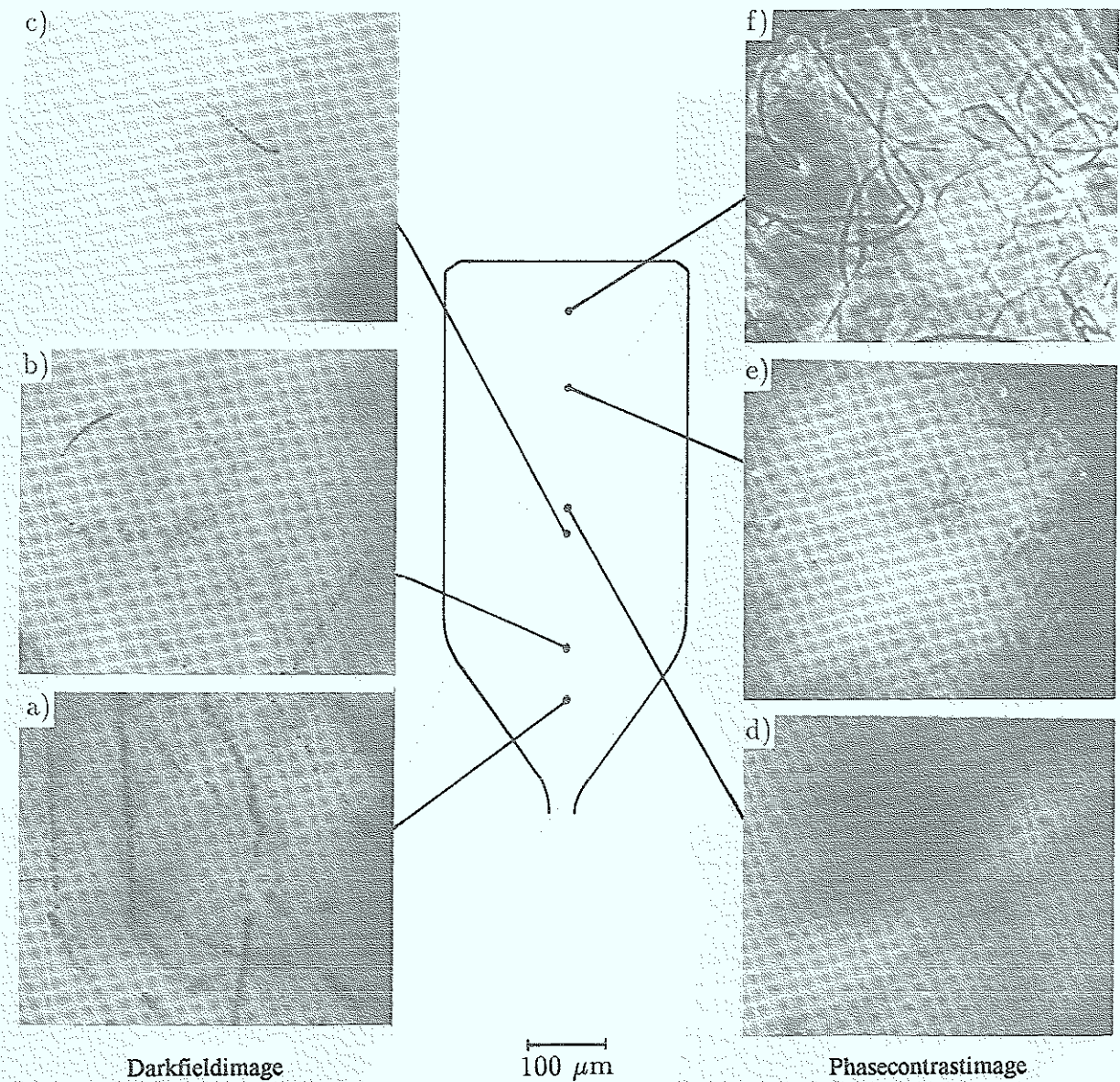


Fig. 62: Phase microscopy - and dark field images of a Te-doped crystal taken at different positions along the growth axis of the crystal. Different positions correspond to free carrier concentration of: a) $= 1.6 \cdot 10^{16} \text{ cm}^{-3}$, b) $= 3 \cdot 10^{16} \text{ cm}^{-3}$, c) $= 1.9 \cdot 10^{17} \text{ cm}^{-3}$, d) $= 2.2 \cdot 10^{17} \text{ cm}^{-3}$, e) $= 1 \cdot 10^{18} \text{ cm}^{-3}$, f) $= 1.3 \cdot 10^{18} \text{ cm}^{-3}$.

concentrations and dislocation can be visualized by phase contrast in the tail end of the crystal when the doping concentration exceeds $\approx 10^{18} \text{ cm}^{-3}$, i.e. the decoration of dislocation in the concentration range up to about 10^{18} cm^{-3} is similar for Si- and Te-doped GaAs.

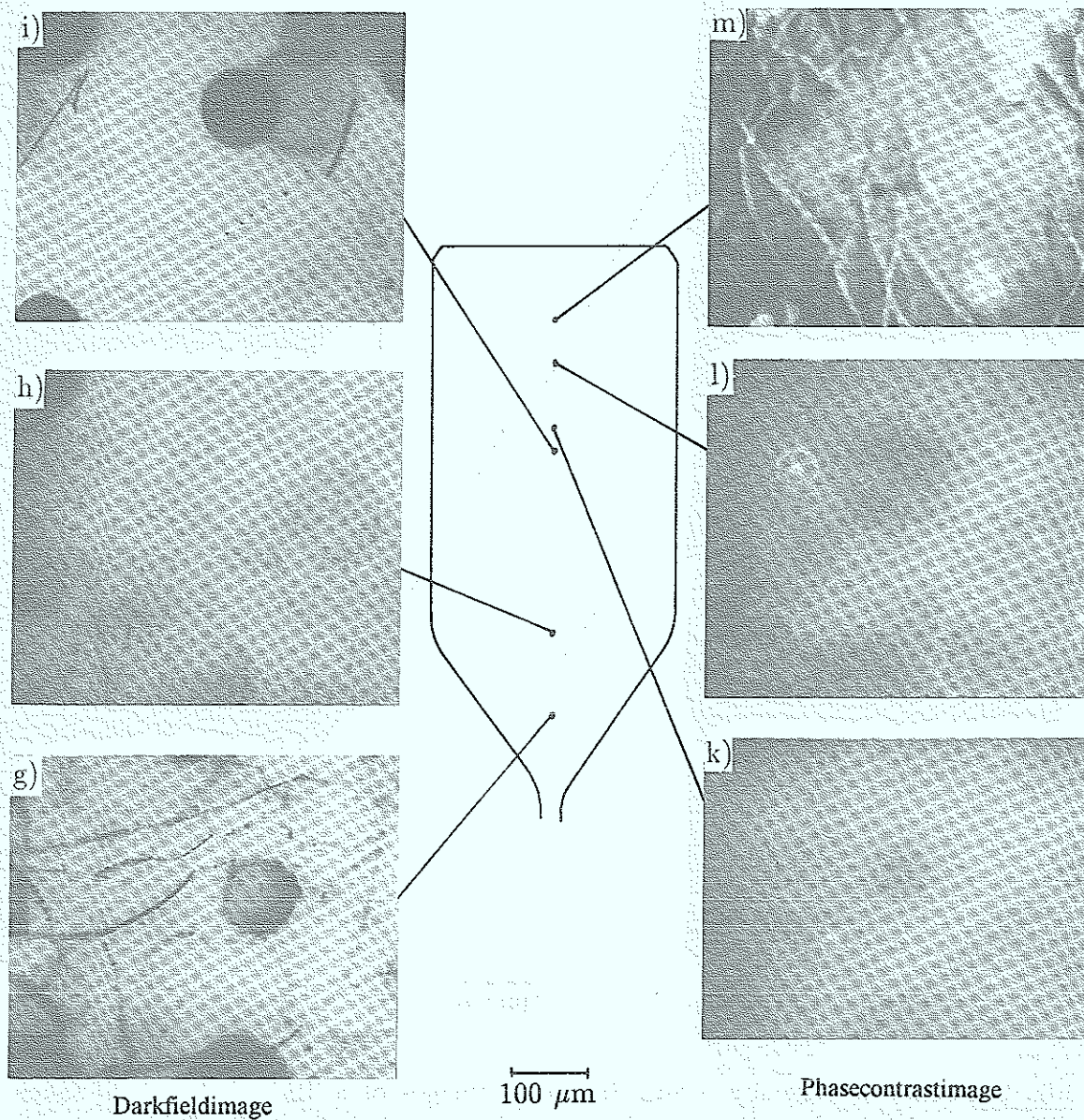


Fig. 62: Phase microscopy – and dark field images of a Si-doped crystal taken at different positions along the growth axis of the crystal. Different positions correspond to free carrier concentration of:
 g) = $1.1 \cdot 10^{17} \text{ cm}^{-3}$, h) = $2.4 \cdot 10^{17} \text{ cm}^{-3}$, i) = $2.6 \cdot 10^{17} \text{ cm}^{-3}$, k) = $2.7 \cdot 10^{17} \text{ cm}^{-3}$, m) = $1 \cdot 10^{18} \text{ cm}^{-3}$.

A more detailed result from the tailend of a Te-doped crystal is shown in figure 63.

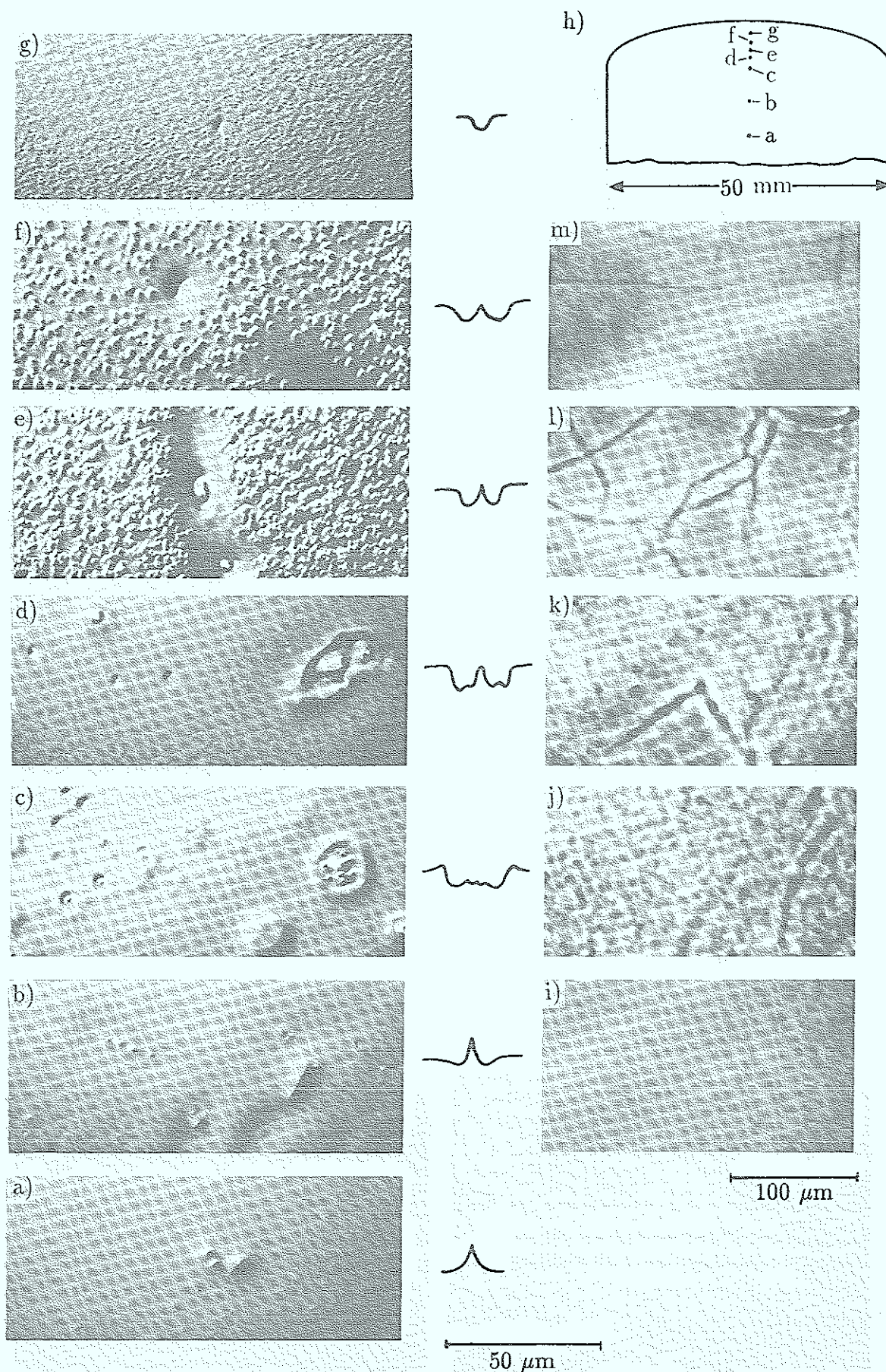


Fig. 63: Comparison of differential interference contrast (DIC) images (a–g) and phase microscopy images (i–m). DIC-images show the profile of the photoetched surface, whereas the phase microscope images of the defect structure inside the specimen. For each position the surface profile of typical defects is presented schematically. The individual position (a–g) within the tail end of the crystal are indicated in h).

For position (a) the zone around the dislocation remain invisible and the photo-etching reveals hillocks (reduced etching rate) a few microns wide. At position (b) when denuded zones just become visible by phase microscopy depressions (increased etching rate) of similar width as the phase contrast can be detected in the vicinity of the dislocation. At position (c) the denuded zones are much wider ($\lesssim 20\mu\text{m}$) and exhibit a stronger contrast. The areas which show a reduced etching rate also extend up to $20\mu\text{m}$ in diameter. This area is also often characterized by micro defects (hillocks due to reduced etching rate) and surrounded by a shallow annular mound. At position (c) we also observe matrix defects (not related to dislocations) which are associated with a dark contrast in the phase microscopy image and a reduced etching rate (the surface profile is similar to that around a dislocation). Matrix defects had also been observed by TEM-studies [56]. In this ref. it was shown that microstructural defects (intrinsic loops and faulted loops [56]) are observed close to dislocation as well as in the matrix. It appears that these loops create denuded zones which are visible in the phase microscope and also by photo-etching. The defect structure at position (d) is very similar to position (c). At position (e) the number of matrix defects have increased dramatically. Probably because of their smaller size they are no longer visible in phase contrast. The width of the denuded zone is decreasing from position (c) to (e). This may be correlated with the increased number of matrix defects. At position (f) the denuded zone around the dislocation extends still lesser and also becomes fainter in contrast until they are no longer visible by phase contrast at position (g). The size of matrix defects decrease further going from (f) to (g). The increasing number of matrix defects is probably related to the increasing concentration of Te-atom, however we cannot exclude the influence of stoichiometric effects. We expect that during growth the concentration of Gallium increases substantially in the melt.

(ii) *Annealing Results*

In the following we will briefly describe some preliminary annealing results for Te-doped material

1. in Figure 64 the effect of a 10 h anneal at $750\text{ }^{\circ}\text{C}$ on the phase contrast of the denuded zones around dislocations and matrix defects is presented.

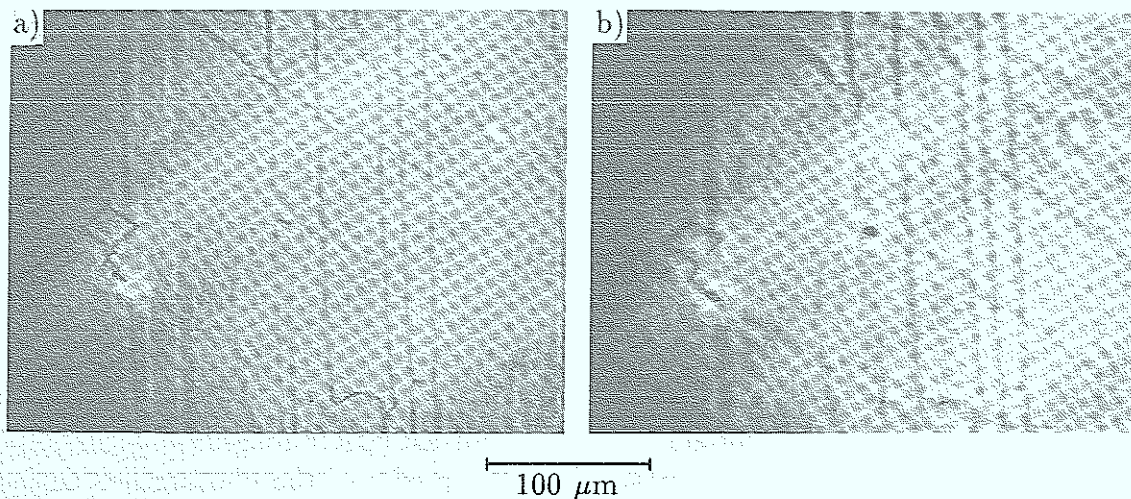


Fig. 64: Phase microscopy image of a Te-doped sample before and after annealing at $750\text{ }^{\circ}\text{C}$ for 10 h.

The contrast after annealing is fainter and the width of the denuded zones is slightly increased.

2. annealing at $850\text{ }^{\circ}\text{C}$ for 20 h results in similar effects, i.e. a reduced contrast and a slightly increased width of the denuded zones. However, in some areas of the crystal, the etching rate around dislocation is reduced, as visible in the DIC-image in figure 65. The phase microscope image of the same area when focussing somewhat below the surface shows a bright contrast around the dislocations. Both result indicate that the free carrier concentration around some dislocation has increased due to the annealing. The defect mechanism responsible for the result is not known.

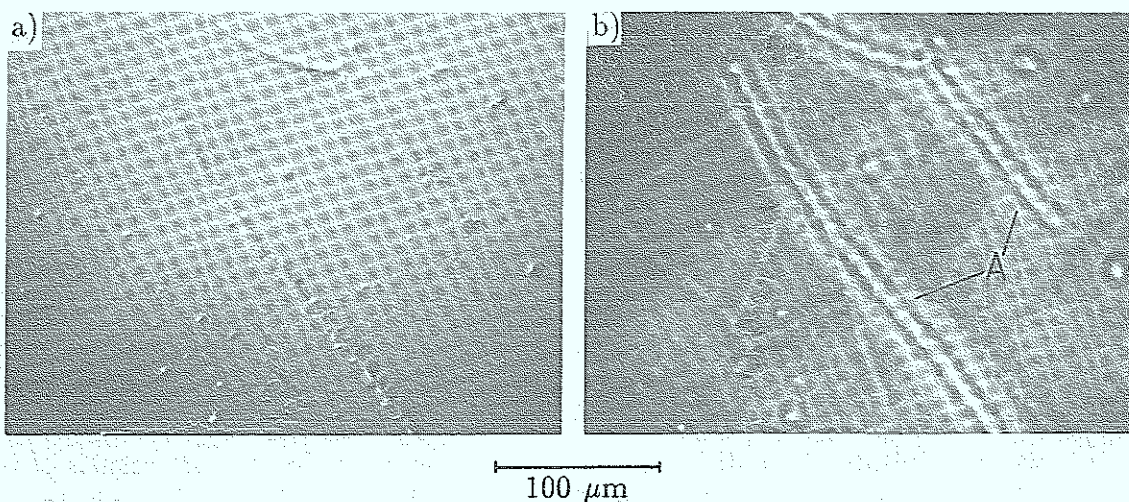


Fig. 65: DIC-image a) and phase microscope- b) of a Te-doped sample after annealing at $850\text{ }^{\circ}\text{C}$ for 10 h. The surface of the sample is photoetched. The bright contrast A on the photoetched surface of image b) is not relevant for the present discussion (it shows the phase contrast image of the photoetched surface).

3. As shown in figure 66 we also observe a bright phase contrast around the dislocation after an annealing treatment at $1100\text{ }^{\circ}\text{C}$ for 10 h with a subsequent fast cool-down to room temperature. Also consistent with this result is the reduced etching rate indicated by the surface profile in figure 66c).

It is interesting to note that in contrast to Si-doped samples the denuded zones do not show any substantial growth at any of the annealing temperatures.

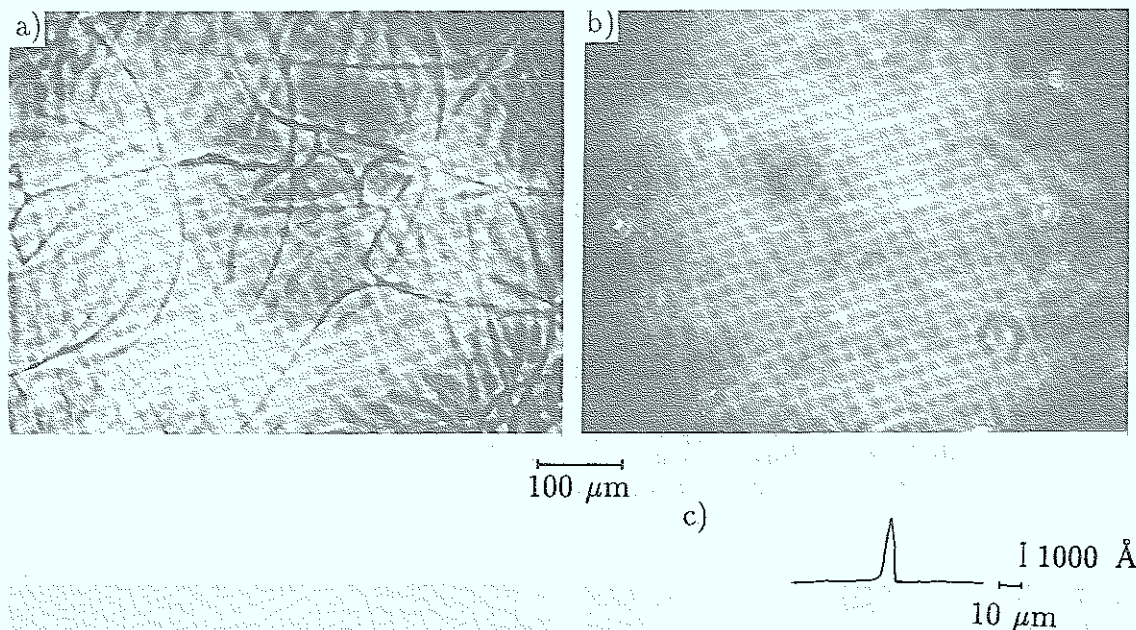
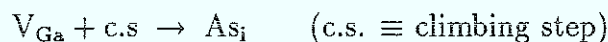


Fig. 66: Phase microscope images before (a) and after (b) annealing at 1100 °C for 10 h. (c) Surface profile after photo-etching of the annealed sample.

3.3. Defect structure in undoped GaAs

The defect structure of as grown undoped GaAs is characterized by dislocation which are decorated by As-precipitates. The formation of these precipitates is due to an excess of arsenic (see also section 3.2.1) present in the material after solidification probably as As-interstitials and Ga-vacancies. Only a minor fraction of the excess arsenic will precipitate along dislocations. There is some evidence from results of ref. [38, 74] that the rest of the arsenic remains e.g. as As-interstitials. Precipitates are formed much more readily at dislocation than in the matrix because dislocations may provide nucleation sites and through positive climbing may also supply additional As-interstitials



As shown in chapter 2 As-precipitates can be most easily detected by NIR-microscopy using dark field contrast. Since the decoration precipitates are typically only a few microns apart the configuration of the dislocation structure can also be seen. In the first part of this section we will present different configuration and types of dislocation which we have found in GaAs-crystals mainly grown by Vertical Bridgman Technique. In some cases we employed photo-etching to resolve details of the dislocation between the decoration precipitates. In the second part we will describe briefly dislocations which are associated with twins the formation of which can be observed in Vertical Bridgman crystals under certain conditions. In the third part we will discuss the influence of the melt composition on the formation of As-precipitates.

3.3.1 Dislocation Structure in VB-crystals

Studying the dislocation structure through darkfield images of decoration precipitates does not allow to determine the Burgers vectors of the dislocation. This information

can be obtained e.g. by x-ray topography or also through IR-microscopy when employing polarized light to image strain fields associated with individual dislocations [see section 3.4]. Relying on darkfield images we can only determine the dislocation vector, but in many cases it is possible nevertheless to safely guess the glide plane and Burgers vector of the dislocation. Another difficulty of the darkfield technique is associated with the fact that the decoration of the dislocation network is not homogeneous, i.e. some dislocation cannot be seen because the precipitates are too small or the dislocation may not be decorated at all. In this context it should be noted that the scattering intensity is proportional to d^6 (d = diameter of the precipitates) i.e. we can probably see only the larger precipitates. We will also show that in some rare cases rows of decoration precipitates can be found which are not associated with dislocations.

(i) *Configuration of dislocation lines:*

Typical dislocation structures found in VB-crystals are shown in figure 67 and 68. The dislocation network consists of curved and straight dislocation segments. The latter can often (see below and section 3.1.2) be related with dislocation line

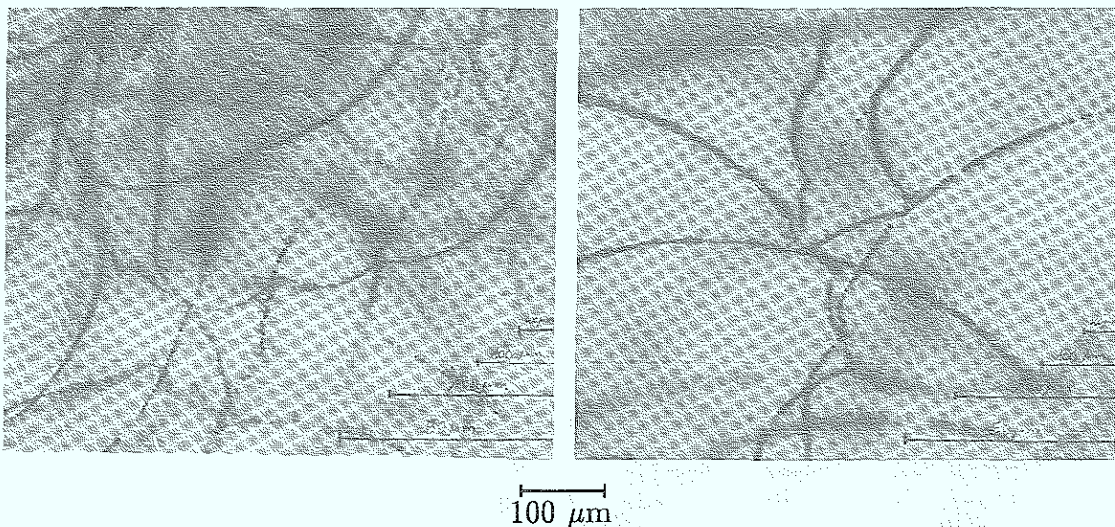


Fig. 67: Darkfield image of doped GaAs grown by VB technique: (110)-plane).

vectors $[112]$ or $[110]$ on a (111) $[110]$ glide-system. Also they are often part of dislocation loops (Fig. 68 and figure 22). Curved dislocation segments are often found parallel to (110) or in particular to (111) -planes¹² (see Figs. 67 and 69). Since dislocation with (110) -glide planes are rarely found in GaAs (see below) it is likely that the dislocation is curved because of climbing processes. The curvature of dislocation on (111) -plane, however is probably due to a glide-process which took place before this dislocation had been decorated with As-precipitates (below ≈ 1000 °C). Under these conditions thermal stresses present in the crystal during the initial cooling can be estimated as indicated in figure 69. The thermal stresses of about 0.02 MPa appear rather small compared to the critical resolved shear stress at the same temperature (see also discussion in section 3.2.2).

¹²The error margin for determining the inclination of dislocation against the image plane is $\lesssim 5$ μm .

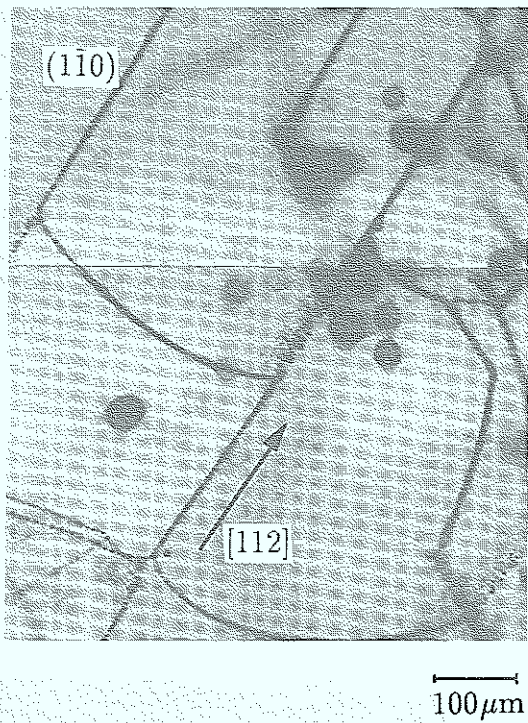
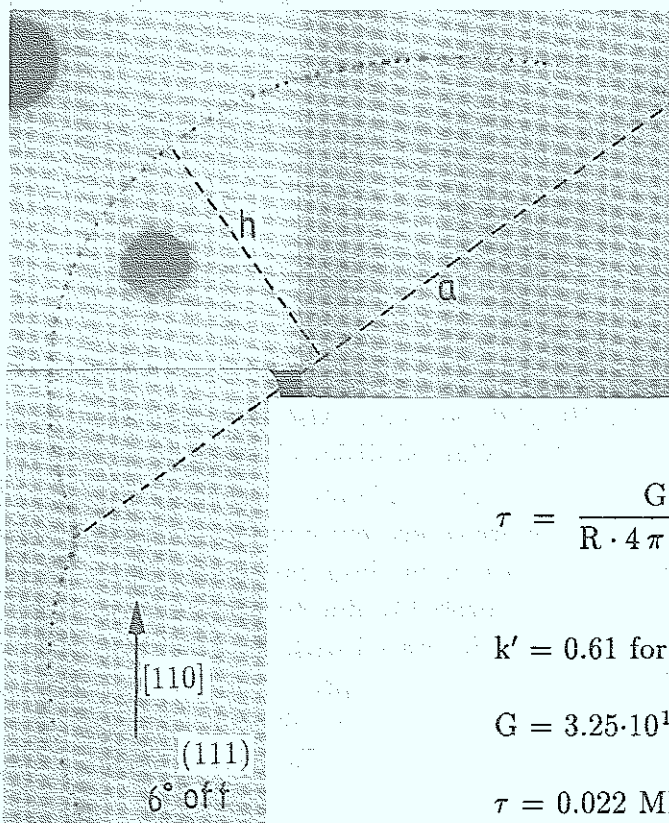


Fig. 68: Darkfield image of undoped GaAs grown by VB technique: (110)-plane.



100 μm

$$R = \frac{a^2 + 4h^2}{8L}$$

$$\tau = \frac{G \cdot b}{R \cdot 4\pi(1-\nu)} \cdot k' \cdot \ln \left[\frac{1.3 \cdot 10^{-3} \cdot R \cdot \arcsin\left(\frac{a}{2R}\right)}{b} \right]$$

$$k' = 0.61 \text{ for } 60^\circ \text{ disloc.}, \nu \approx 0.32$$

$$G = 3.25 \cdot 10^{10} \text{ Pa}; \quad b = 4 \cdot 10^{-10} \text{ m [95]}$$

$$\tau = 0.022 \text{ MPa}$$

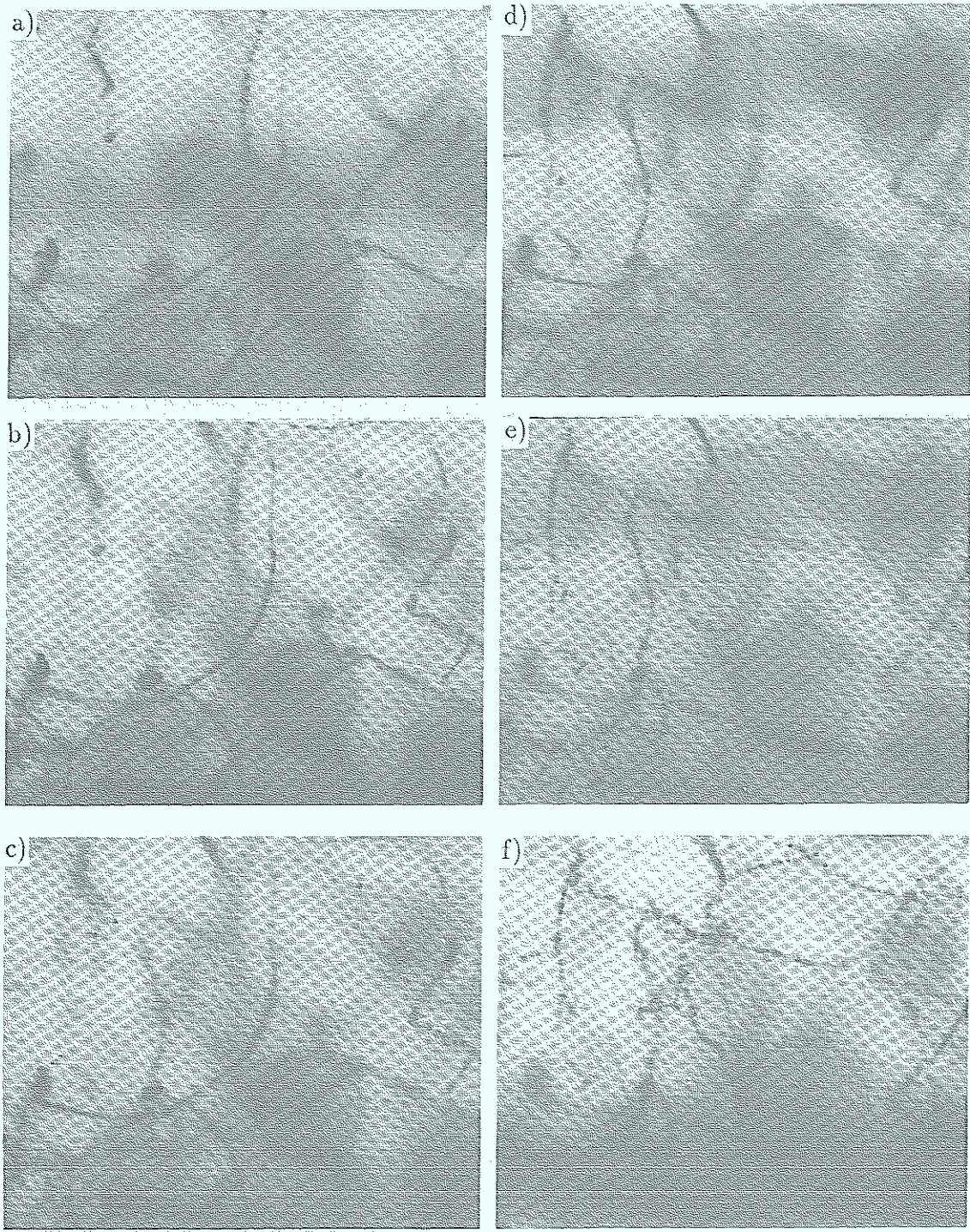
Fig. 69: Darkfield image of undoped GaAs grown by VB technique: (110)-plane.

Darkfield images can also be employed to determine the dislocation density as well as the number of decoration precipitates. Knowing their average size (from recent TEM-studies in our laboratory we know that the decoration precipitates in VB-crystals are larger than in LEC-material: typical size in VB-material is $\approx 0.35 \mu\text{m}$) we can also estimate the total amount of arsenic contained in the decoration precipitates. Note that the dislocation density per cm^{-2} (Etch Pit Density) is related to the total length (cm) of dislocations per cm^{-3} . The etch pit density is expected to be somewhat smaller (\approx factor 2) than the total dislocation length. The difference between both quantities depends on the types and distribution of dislocation which form the dislocation network. The total length of dislocations has been determined as shown in figure 70: Darkfield images are taken by focussing at successively increasing depths. If the focussing planes of two successive images are closer than the focal depth of the microscope the whole dislocation network of the selected volume can be imaged. The length of this network projected onto the image plane is shown in figure 70g. Using the projected length for estimating the dislocation density partially compensates the error made by comparing the total dislocation length with the etch pit density. The dislocation density $\approx 5000 \text{ cm}/\text{cm}^3$ derived from figure 70 is a typical value for VB material as found by counting etch pits [1]. The amount of arsenic contained in decoration precipitates $N \approx 10^{15} \text{ cm}^{-3}$ appears almost an order of magnitude smaller than found in LEC-grown material.

(ii) *Dislocation Cell Structure in VB-crystals:*

As shown in ref. [1] and [110] dislocation cell structures can also be found in VB-crystals if the density of the dislocation is sufficiently high ($> 5 \cdot 10^3$). Cell structure can be detected most easily by etching methods (see [1, 111]) but can also be seen by infrared microscopy as shown in figure 71 and 72. The latter shows the cell structure for a LEC-grown crystal using a darkfield image of the As-precipitates which decorate the dislocation in the cell wall. Probably due to a much higher dislocation density for LEC-crystals as compared to VB-material the As-precipitates are somewhat smaller. Sometimes the scattering intensity from LEC-material is too small to resolve any decoration precipitates by our darkfield technique. Figure 71 shows vertical Bridgman material which was grown with a very high growth rate resulting in a high dislocation density. Since the material was Te-doped the dislocation can only be imaged by phase microscopy. Individual dislocations can be resolved within the cell wall. The presence of straight (often part of dislocation loops) and curved dislocation segments indicate that climb as well as glide processes must have been involved in forming cell structure by polygonisation.

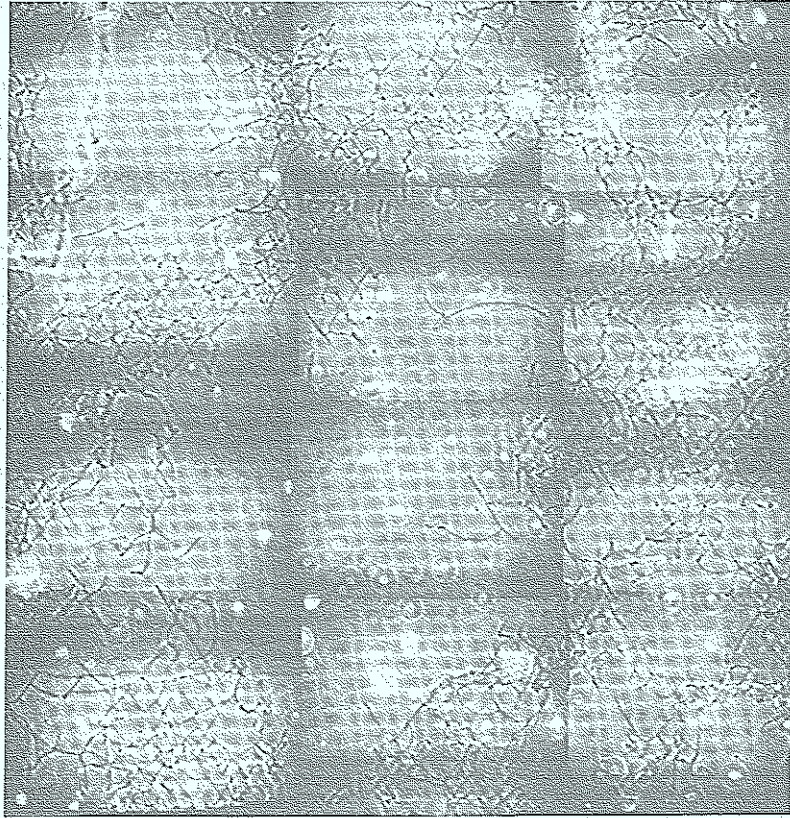
An alternative model [111] attributes dislocation cell structure to chemical inhomogeneities which can be generated by constitutional supercooling effects. They destabilize the growth front which then breaks up into cells separated by cell walls containing a different impurity concentration or stoichiometrical composition. As a result the lattice mismatch between the cell interior and the cell wall may become so large that dislocations are generated to accommodate the lattice strain. Although this model is favoured by some [111, 112], most groups [2, 113,



100 μm

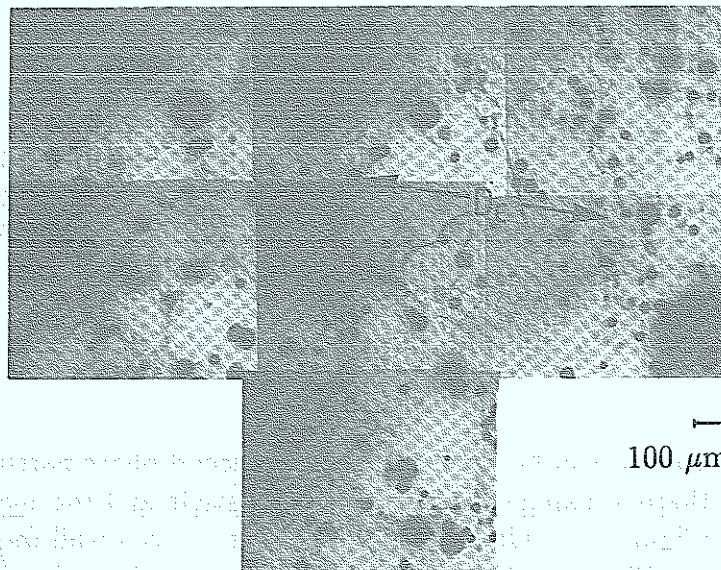


Fig. 70: Darkfield image of undoped GaAs (VB-crystal) a, b, c, d, e, f are images of the same area at successive depths; g) Total length of the dislocation network projected onto the image-plane: 93 cm in 0.016 cm^3 equal 5800 cm/cm^3 . Average distance (size) of precipitates $\approx 4 \mu\text{m}$ ($0.3 \mu\text{m}$): $N_{As} \approx 10^{15} \text{ cm}^{-3}$



100 μm

Fig. 71: Phase microscopy image of Te-doped GaAs grown by VB-technique (high growth rate).



100 μm

Fig. 72: Darkfield image of SI-GaAs grown by LEC ($D_C =$ cell diameter)

114] believe in cell formation by polygonisation processes of dislocations. It is difficult to see how to obtain differences in impurity concentration between the cell interior and the cell wall sufficiently large to create the necessary lattice mismatch. For In-doped material it has been shown [115] that the concentration difference of $\gg 10^{19} \text{ cm}^{-3}$ is required to generate misfit dislocations. For undoped material concentration differences in native defects (stoichiometric effect) on the other hand do not generate large lattice distortions.

Cell formation as a result of constitutional supercooling in fact can be observed in GaAs for undoped as well as doped material, but normally only at the tail end of the crystal. In figure 73a cell formation is shown for undoped material which is due to an excess of gallium as revealed by Ga-droplets in the cell walls (see figure 73d). In figure 73b, c cell formation was generated by macrosegregation of Te when high growth rates were employed. If constitutional supercooling is relevant for the formation of dislocation cell structure we would expect to find an increased dislocation density in the cell walls shown in figures 73b, c which are formed by constitutional supercooling. DIC-images after photo-etching (figures 73a, c) as well as the phase microscopy image for the doped sample do not indicate any increases in dislocation density when comparing crystal regions which contain CS-cell wall and those which do not. Therefore it is unlikely that dislocation cell structure will be the result of constitutional supercooling effects.

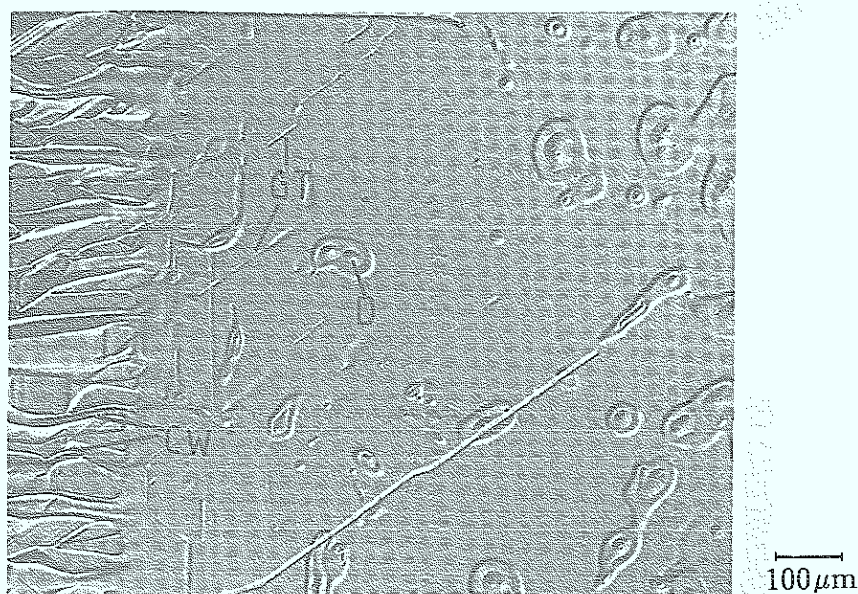
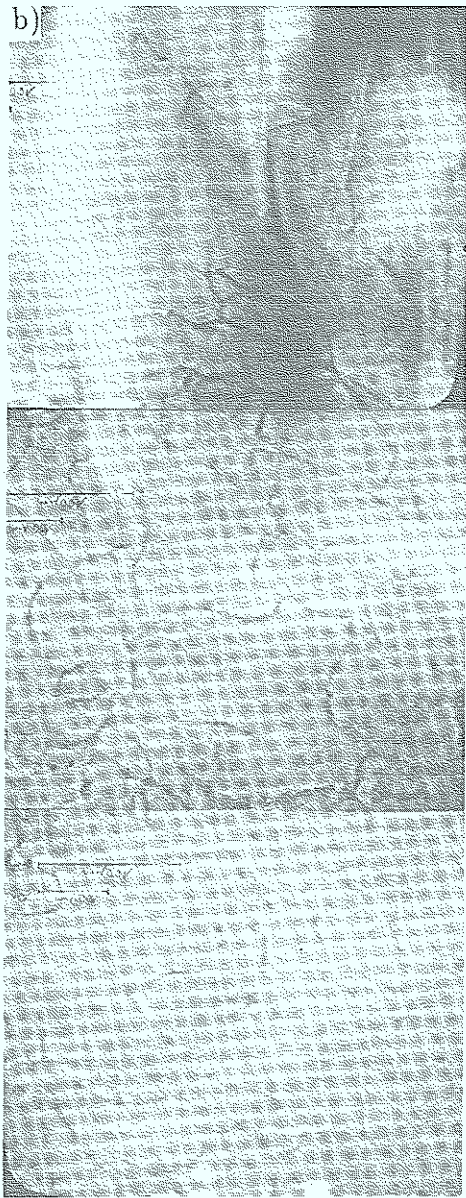
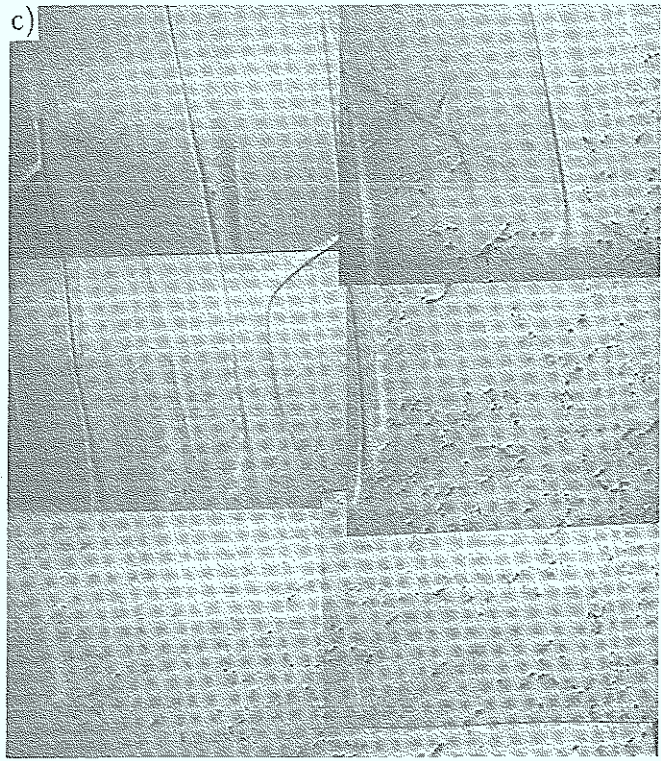


Fig. 73: a) DIC-image of a photoetched surface of undoped GaAs grown from a Ga-rich melt (D: dislocation; GT: glide traces of of dislocation; CW: cell walls)

Misfit dislocations can be generated e.g. by second phase particles due to the difference in thermal expansion between the particle and the matrix. An example is shown in figure 73d) Ga-droplets are formed in cell wall due to constitutional supercooling. Photoetching of the surrounding of these droplets reveals a high density of dislocations probably due to the differential thermal expansion coefficient of the Ga-inclusion and the GaAs-crystal.



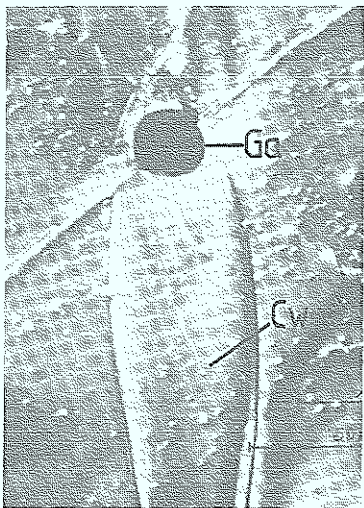
100 μm



100 μm

Fig. 73 b), Phase microscope image of Te-doped GaAs (c.s.: area exhibiting constitutional supercooling).

Fig. 73 c), DIC image of a photoetched surface of Te-doped GaAs.



100 μm

Fig. 73 d), DIC-image of photoetched surface of undoped GaAs: Cell walls at the end of a crystal are often terminated by a Ga-droplet (Ga: Ga-droplet; CW: cell wall).

(iii) *Lineage in VB-crystals:*

It is sometimes questioned [113] that lineage has been observed also in VB-crystals. R. Naeven [1] clearly showed that lineage occurs also in this material. By studying lineage which forms close to the edge of the crystal R. Naeven found by photo-etching the crystal surface close to a $[110]$ -direction (B) as well as the (001) cross-section (A) that the lineage may be characterized as a subboundary composed of $[112]$ dislocation lines. By preparing a microscope sample with a $(\bar{1}\bar{1}0)$ -surface the subboundary can be imaged in the darkfield, indeed showing that the subboundary does consist mostly out of $[112]$ -dislocation lines.

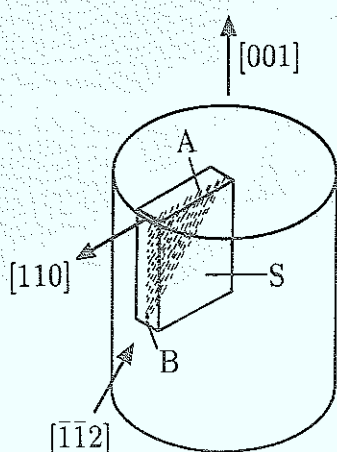


Fig. 74: Schematic diagram for the dislocation structure of the lineage observed in VB-crystals.

A small angle boundary as shown in figure 75 we expect to be formed through polygonisation of edge dislocations of the glide system $(111) [\bar{1}10]$ with a line vector $[\bar{1}\bar{1}2]$. (This type of dislocation has also been often identified in GaAs (see also section 3.2.2). This interpretation of lineage contradicts that given by H. Ono [116] and D.J. Stirland [113] who attribute lineage to the formation of sessile dislocation lying along $[110]$ -direction and acting as precursor structure of

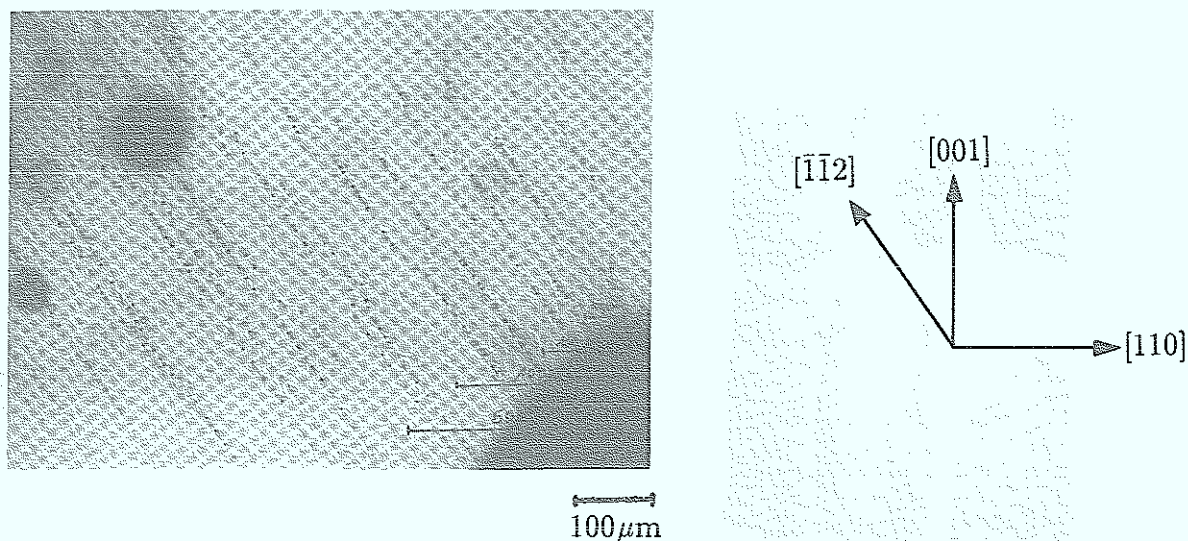


Fig. 75: Darkfield image of undoped GaAs grown by VB-technique: small angle boundary consisting out of $[112]$ -dislocation-lines. (The sample was cut from the crystal as indicated in figure 74).

the lineage. The sessile dislocation are formed by interaction between dislocations on inclined slip planes. It is difficult to see how a dislocation although lying along $[110]$ and usually only less than $100 \mu\text{m}$ long can cause a lineage feature which often extend over 1 cm . Also lineage features are often observed (see R. Naeven: Formation of polycrystalline growth) to coalescend along the growth direction to form a small angle ground boundary containing a higher density of dislocations. This process is most easily understood as a continuation of polygonisation if this process is also responsible for forming the lineage structure. If the lineage was generated through reactions of a sessile dislocation with slip dislocation it would be difficult to understand the coalescence of adjacent lineage features.

To study the dislocations of the subboundary shown in figure 75 in more detail, the sample was thinned down so that the dislocation lies very close to the surface. After photo-etching (see Fig. 76) it was evident that the dislocation lines are pinned by the As-precipitates forming arches between them parallel to the $(\bar{1}10)$ -surface of the sample. From the previous arguments we may exclude the $(\bar{1}10)$ -plane as a slip plane for these dislocations; i.e. we must interpret the arching of the dislocation between the precipitates as due to a climbing process.

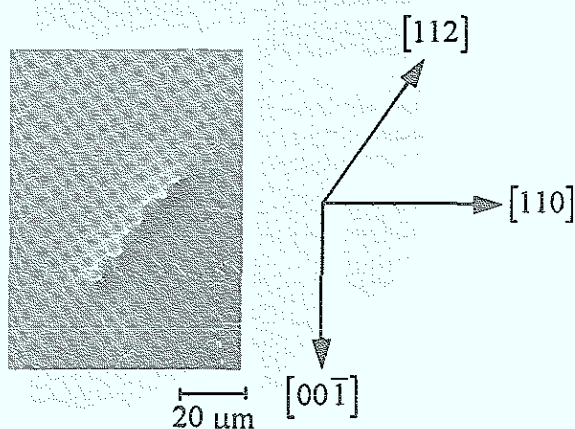


Fig. 76: DIC-image of undoped photoetched sample: Climbing of $[112]$ -dislocations in a (110) -plane.

In one crystal another type of small angle grain boundary (figure 77) has been observed. It extends in axial direction from the seed area to the tailend and in radial direction from the centre to crystal surface (as indicated in figure 77a). Darkfield images of sample 1 mainly show $[001]$ dislocation lines in the small angle grainboundary. Photo-etching of sample s_2 (see figure 77c) reveals the grainboundary as a feature (A) which is often called a "streamer" in the literature [117]. Similar small angle grainboundaries have been observed by F.L. Vogel [118] in Ge and have been identified as $[001]$ dislocation line on a (110) $[110]$ glide system. Edge dislocation along $[001]$ also have been found in In-doped GaAs grown by LEC [5]. They are observed in the central area which extends in radial direction up to the diameter of the seed. Therefore it is most likely that the dislocations observed in figure 77 are characterized by $\vec{u} = [00\bar{1}]$, $\vec{b} = \frac{1}{2}[110]$ and a $(\bar{1}10)$ -slip plane. The same conclusion will be drawn in section 3.4 from the results of polarisation microscopy. Imaging sample s_1 in polarized light (figure 93) with high magnification we find the dislocation line forms arches between the As-precipitates which act as pinning points. Since the image-plane is normal to the slip plane for edge dislocations of a small angle grainboundary (which is parallel to (110)) the arching must be attributed to climbing processes.

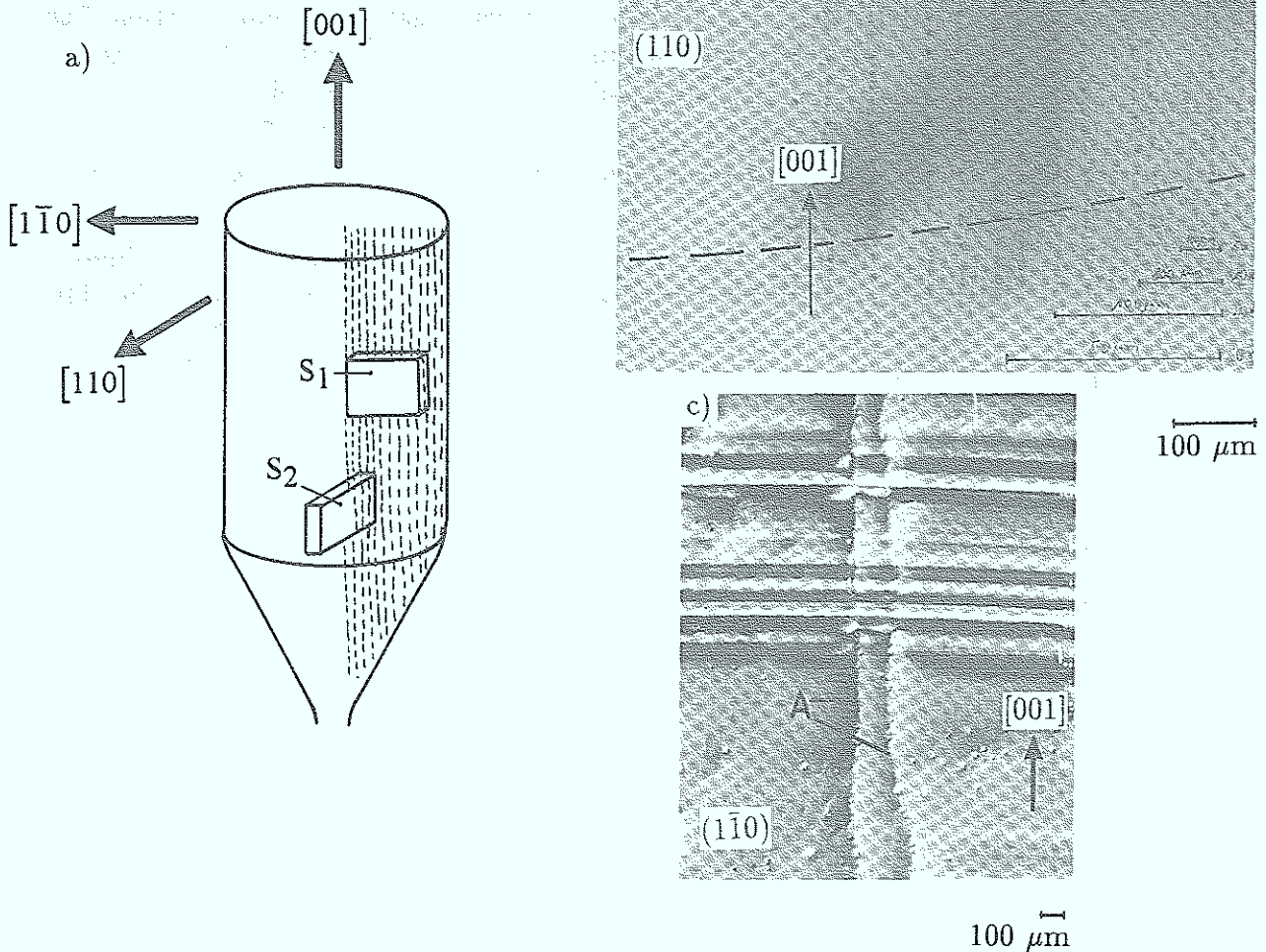


Fig. 77: a) Schematic diagram of the VB-crystal contain a small angle grainboundary along $[110]$ consisting of $[001]$ -dislocation lines, as shown in b) by the darkfield image of sample (s_1). The dashed line indicates the growth front, which was determined by photo-etching of the surface of sample s_1 . c) DIC-image of the photoetched sample (s_2).

Dislocation growing out of the seed and propagating along the central axis are supposed to grow together with the crystal (so-called grown in dislocations). For this type of dislocation we expect that Klapper's theorem [121] – that the path of dislocations at the newly formed interface is driven by the tendency to minimize the strain energy per dislocation line length ought to apply, i.e. dislocations should propagate normal to the growth surface. This tendency has been observed in ref. [119]. The dislocations shown in figure 77b do not exhibit such a behaviour. This is very conspicuous near the edge of the crystal where the curvature of the growth striation increased.

(iv) "Pseudo" decoration precipitates:

In almost all crystals doped or undoped structural defects are observed featuring rows of precipitates. Two examples are shown in figure 78. These features are predominantly formed in the middle part of the crystal, less in the cone area and almost none in the tail end. They are particularly conspicuous in doped samples

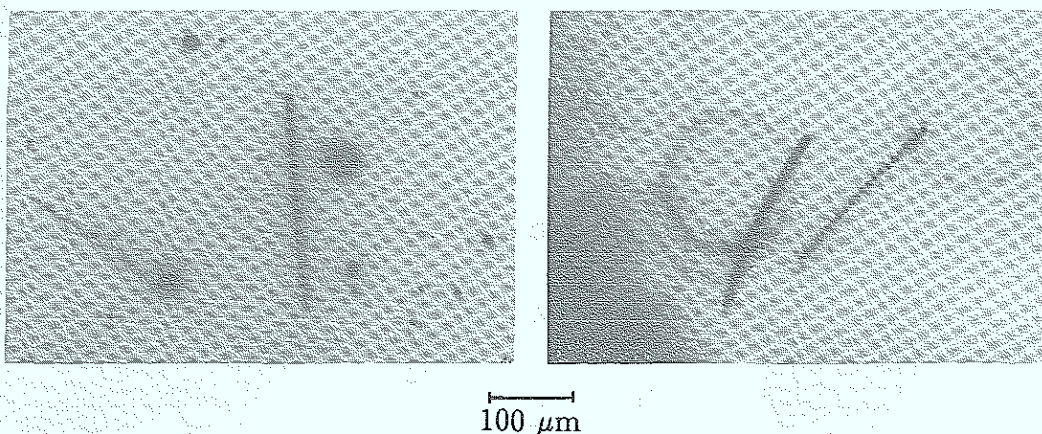


Fig. 78: Darkfield image of precipitates which are not associated with dislocations.

because the decoration precipitates at the dislocation are often too small to be seen in the darkfield image, as shown in figures 62c and 62i. If these features are associated with dislocations they appear to be disconnected from the rest of the dislocation network. Because of this observation we performed X-ray topography studies the results of which are presented in figures 79a-i.

Identical sample areas imaged by X-ray topography and IR-darkfield can be identified through the dislocation structure. Compare figure a with b, d with e and g with h. Each image pair shows the same dislocation structure with the exception of features which are marked by P. These features cannot be seen in X-ray topography (they remain also invisible for different imaging conditions). This means that the rows of precipitates (P) are not associated with dislocations. The same conclusion will be drawn from the results of polarisation microscopy. A possible mechanism is sketched in figure 80. As already shown in section 3.2.2 dislocations perform glide processes due thermal stresses during the cooling period of the crystal. Evidence was presented that this happens in a temperature range between 900 °C and 1000 °C. This is also the temperature regime in which the formation of As-precipitates takes place. Assuming a dislocation - as sketched in figure 80 - with decorated (D_1) and undecorated (D_2) segments moving from position (1) to position (2) would leave a row of precipitates in position (1) not associated with a dislocation.

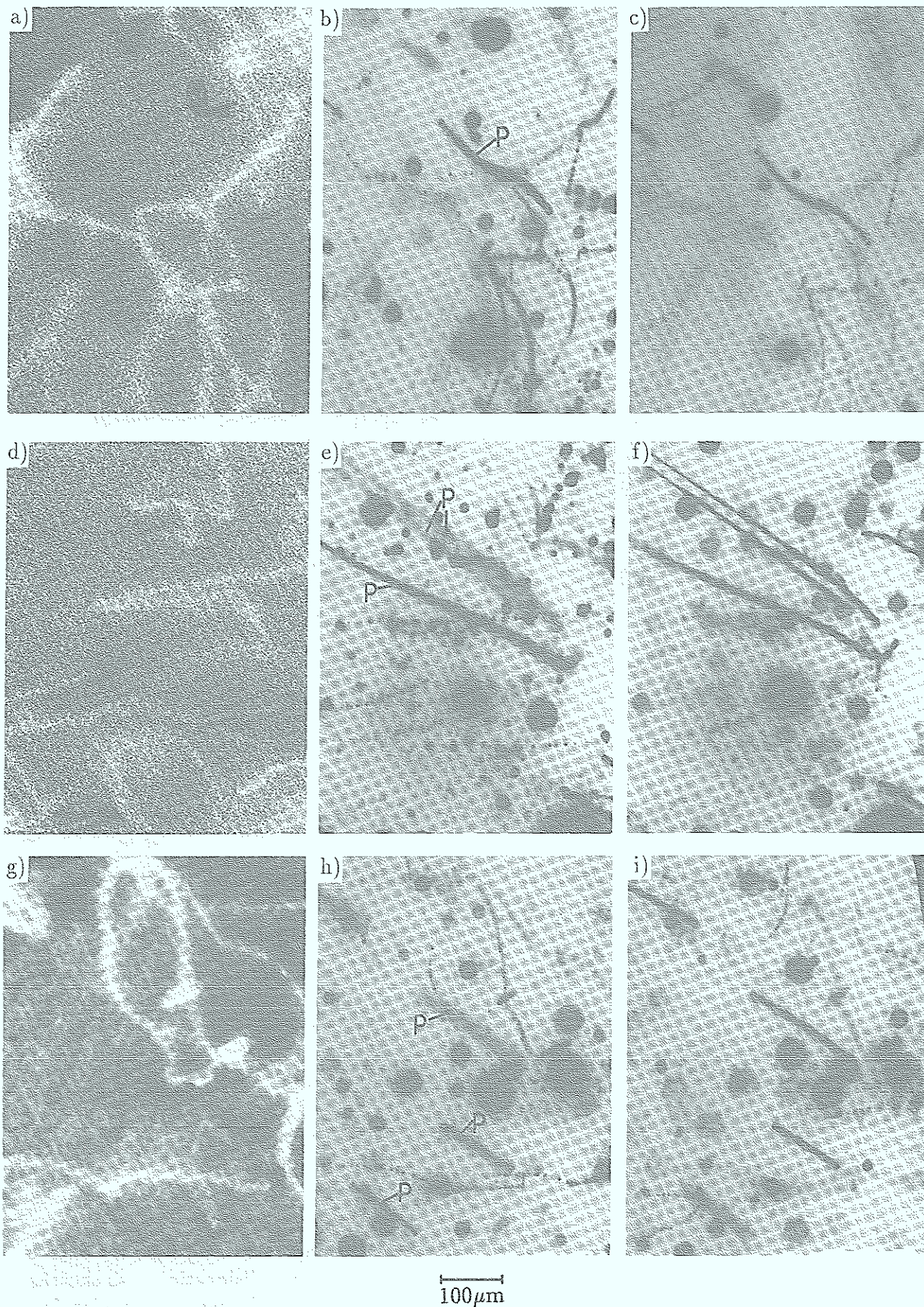
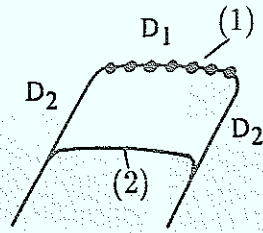


Fig. 79: Darkfield- (b, c, e, f, h, i) and X-ray topography images (a, d, g) of identical sample areas: (abc, def, ghi); X-ray topography was taken with $\text{MoK}\alpha_1$ radiation on a (220)-reflex. The IR-images bc, ef, hi show identical areas for different focussing conditions.

Fig. 80:



(v) *Other decoration features:*

- a) Very often the decoration of dislocations with precipitates extends in a planar way as shown in figure 81 and 82. The dislocation probably belong to the (111) [110] slip system with [110] and [112] line vectors, respectively. Planar extension of the decoration may be expected if the dislocations are subjected to glide or climb processes in a temperature range where the decoration precipitates are formed. Since the decoration often extends in a (110)-plane, which is not the slip plane for dislocations in figure 81, climb processes are probably more relevant. Photoetching results as shown in figure 81c reveal dislocation which are arching between precipitates acting as pinning points. Most of the precipitates are no longer connected to the dislocation, the existence of precipitates may only reflect earlier position of the dislocation. According to ref. [67] and [5] climb of the dislocation must be considered as the prime cause for formation of As-precipitates (see also section 3.2.1). Absorption of a Ga-vacancy at the dislocation initiates a positive climbing step which is accompanied by the release of an As-interstitial. The agglomeration of As-interstitials which stem from this reaction together with the absorption of Ga-vacancies from the matrix results in the formation of As-precipitates. The complementary mechanism of absorbing As-interstitials in a negative climbing step, associated with the release of Ga-vacancies would also lead to As-precipitation, but is less likely because positive climbing is dominant as shown in ref. [71]. From the result presented in figure 81b and 82b that As-precipitates can be also observed at dislocation (A) not subjected to climb, we must conclude that climb is not a necessary condition for As-precipitation; necessary defects - Ga-vacancies and As-interstitial - may be sufficiently present in the matrix¹³. It appears, however that more As-precipitates (per dislocation line length) are found for those dislocation which participate in climb actions, i.e. climb may help to form As-precipitates but is not a necessary condition. It is not clear why sometimes only one of two adjacent (less than $\approx 10 \mu\text{m}$ apart) dislocation (A, B) or only a part of a dislocation is subject to climb while the other remains unaffected. This observation makes local fluctuations (as suggested in ref. [71]) in the defect concentration (V_{Ga} , As_i) as a possible cause very unlikely. Differences in the microstructure of dislocations, e.g. jog densities may be a more likely reason for the differences in climb.
- b) "Arrowhead"-feature. Feature which are similar to an arrowhead have often been observed. In many cases the arrowhead is connected to dislocation lines (straight or zigzag-shaped: figure 83a, b, c, d) sometimes however, it appears

¹³This is also confirmed by the existence As-precipitates which form in the matrix during post growth annealing treatment [113] or in Si-doped material (see section 3.2.1)

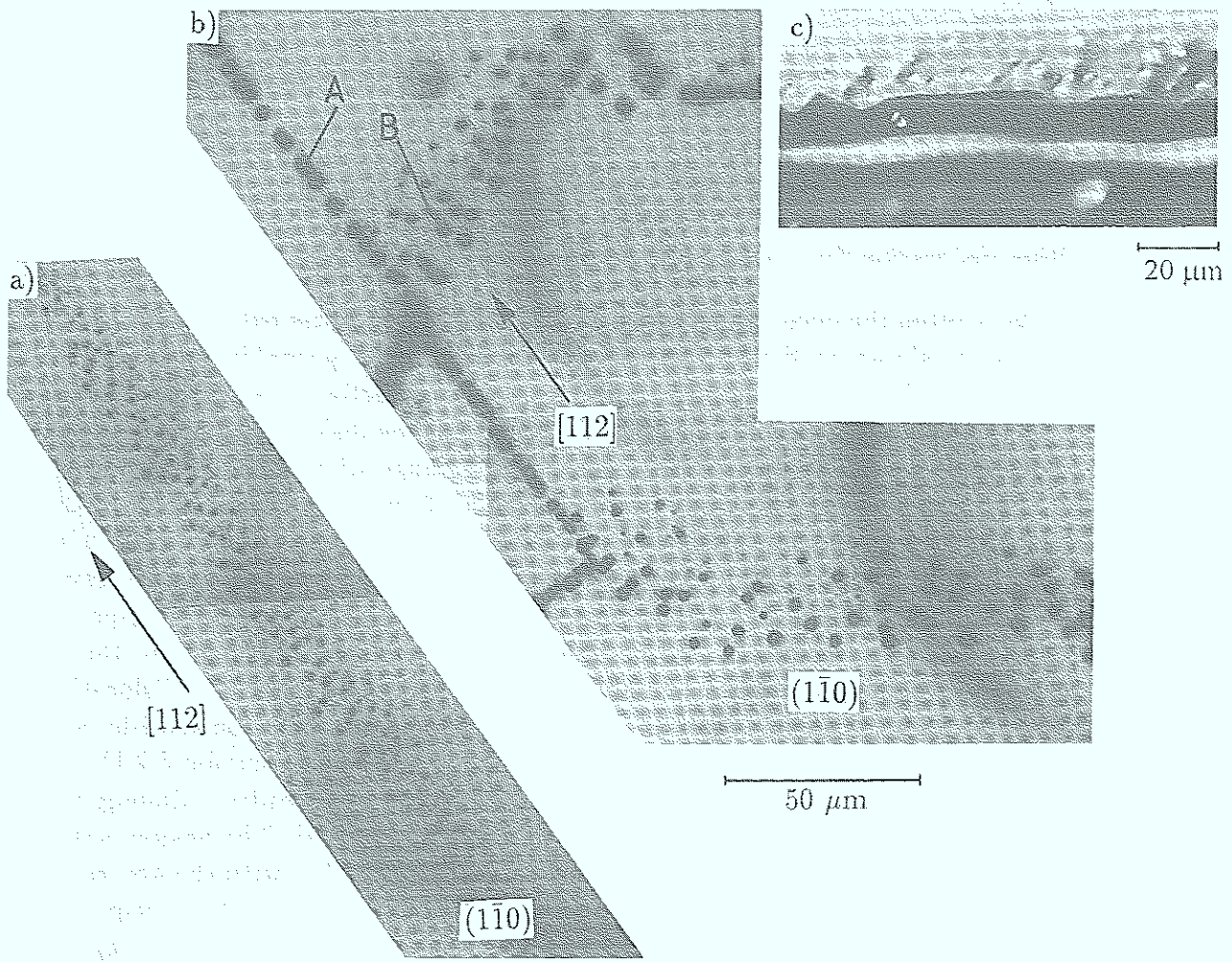


Fig. 81: a), b) Darkfield images of undoped VB-grown GaAs, c) DIC-image of a photoetched sample

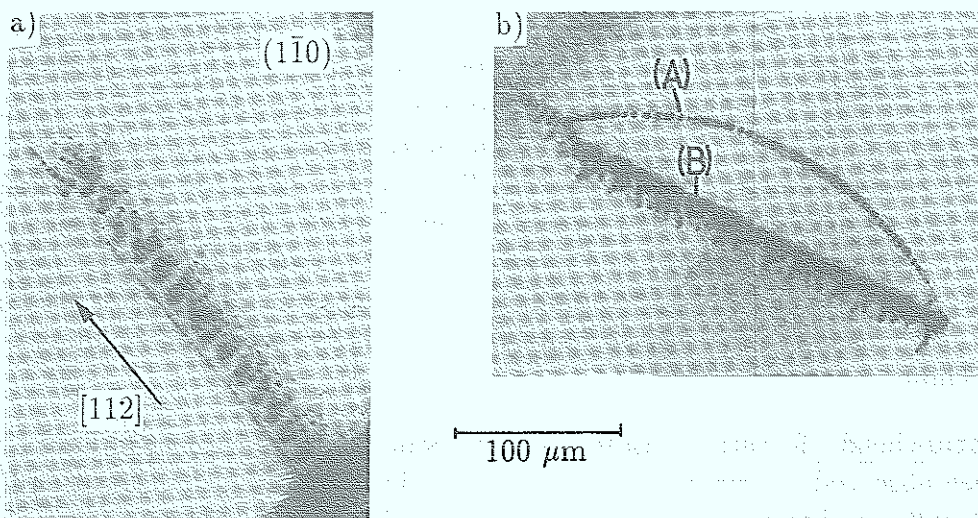


Fig. 82: Darkfield images of undoped VB-grown GaAs.

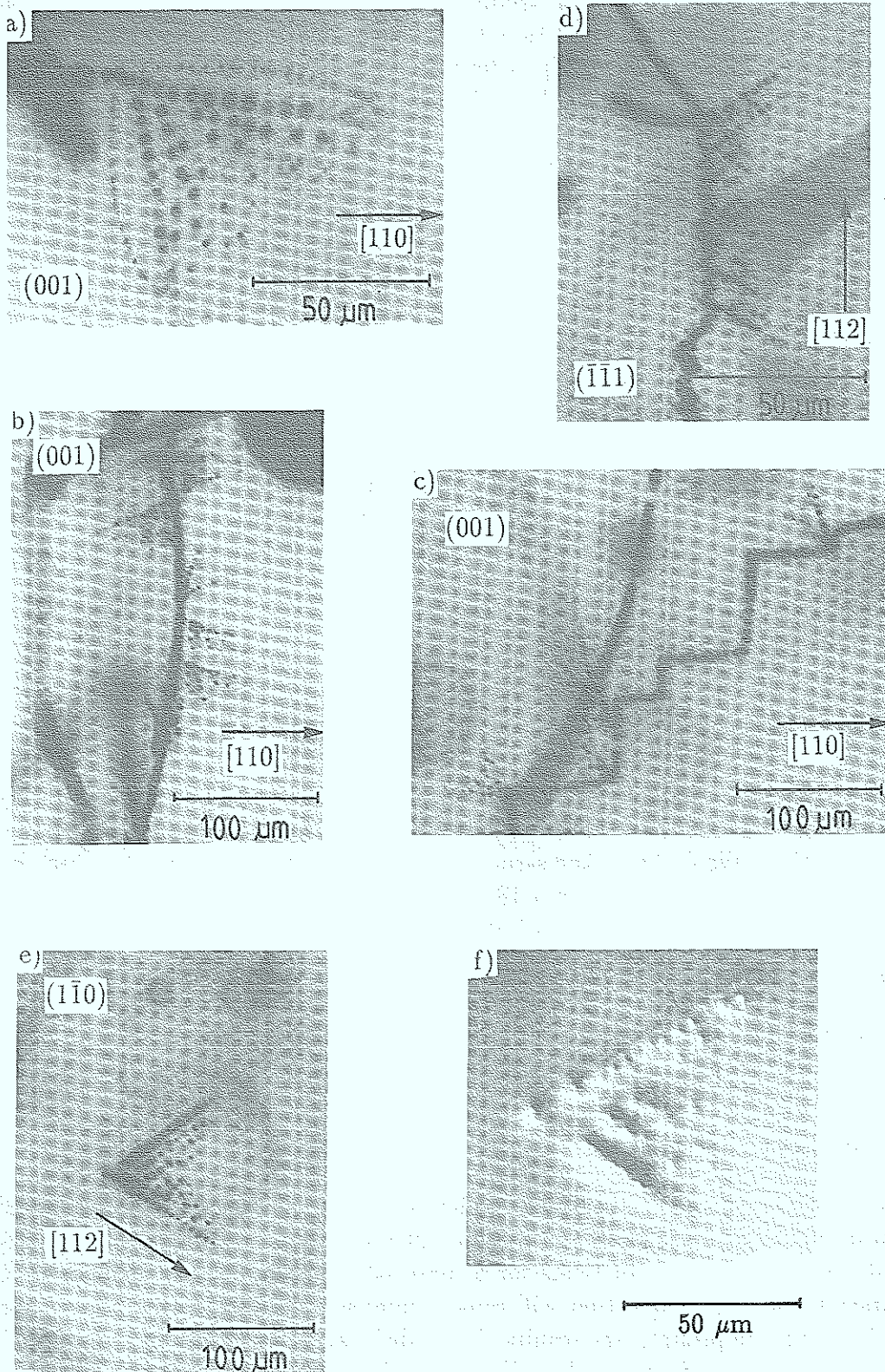


Fig. 83: Darkfield images of undoped as grown GaAs: a, b, c (001)-plane, d $\approx (111)$ -plane; e $\approx (110)$ -plane; f) DIC-image of a photoetched sample (110)-plane.

disconnected (e) or the related dislocation remains invisible, because it may not be decorated. The dislocation which is associated with the arrowhead can be resolved by photo-etching as shown in figure 83f. The dislocation forms a contour line around the triangular decorated area. A possible formation mechanism of this dislocation loop has been suggested in ref. [120]. As shown in figure 84 the loop is formed by cross-slip at a jog with both the jog and the Burgersvector of the dislocation sharing a common slip plane.

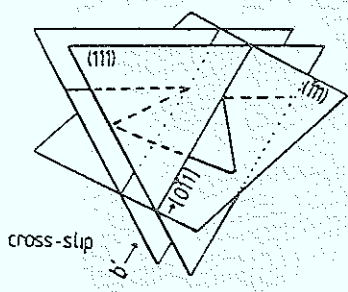


Fig. 84: Dislocation cross-slip for formation of an "arrow-head" loop.

Following this interpretation it is however, difficult to understand why the arrowhead feature is also observed in (110)-planes (e) and (100)-planes (a, b, c), respectively which are no slip-planes. These results rather point to climb as the underlying mechanism.

It should be noted that some of the planar feature shown in figure 82 may also be interpreted as a row of overlapping arrowheads.

3.3.2 Grown-in twins

For a long time twins have been one of the most intensely studied subject in crystal growth [see e.g. 121, 122, 123]. We are, however, still far from a complete understanding of twin formation. We do know the structure of twin boundaries in GaAs which has been identified (see e.g. [110]) as due to a 180° rotation about a (111)-axis. We also know growth conditions which favour twin formation such as

- low stacking fault material ($\text{InP} < \text{GaAs}$)
- large growth rate, large supercooling and facet areas
- impurity contamination (i.e. reduction of surface energy), stoichiometric effects
- fluctuations of the growth rate

These conditions can be qualitatively understood in terms of a "2"-dimensional nucleation on (111)-facets, (see [122]) but the question remains: why does a nucleation model describe the growth of twins for a material which is heavily dislocated (GaAs in contrast to Si)? This question will remain unanswered also in this paper. We will briefly discuss some preliminary results on the dislocation structure of twin boundaries and the interaction of matrix dislocations with the twin boundary.

Twinning occurs in crystals for which twin boundaries of good structural fit (i.e. low energy) are possible. We do not expect - in contrast e.g. to a small angle grain boundary - dislocations to be required to adjust the fit of the crystals on both side of the

boundary. (Twin boundaries can be observed in Si-crystals which are dislocation free.) In contrast, in InP [124] - studied by X-ray topography - a very high dislocation density has been observed on the twin boundaries. In the present paper we present results on the dislocation structure of twin boundaries for the first time for GaAs. The results have been obtained by IR-darkfield observations and by polarisation microscopy (see section 3.4). The images presented in figure 85 are taken from a crystal which contains twin lamella as schematically shown in figure 85f. The projective image a) exhibits

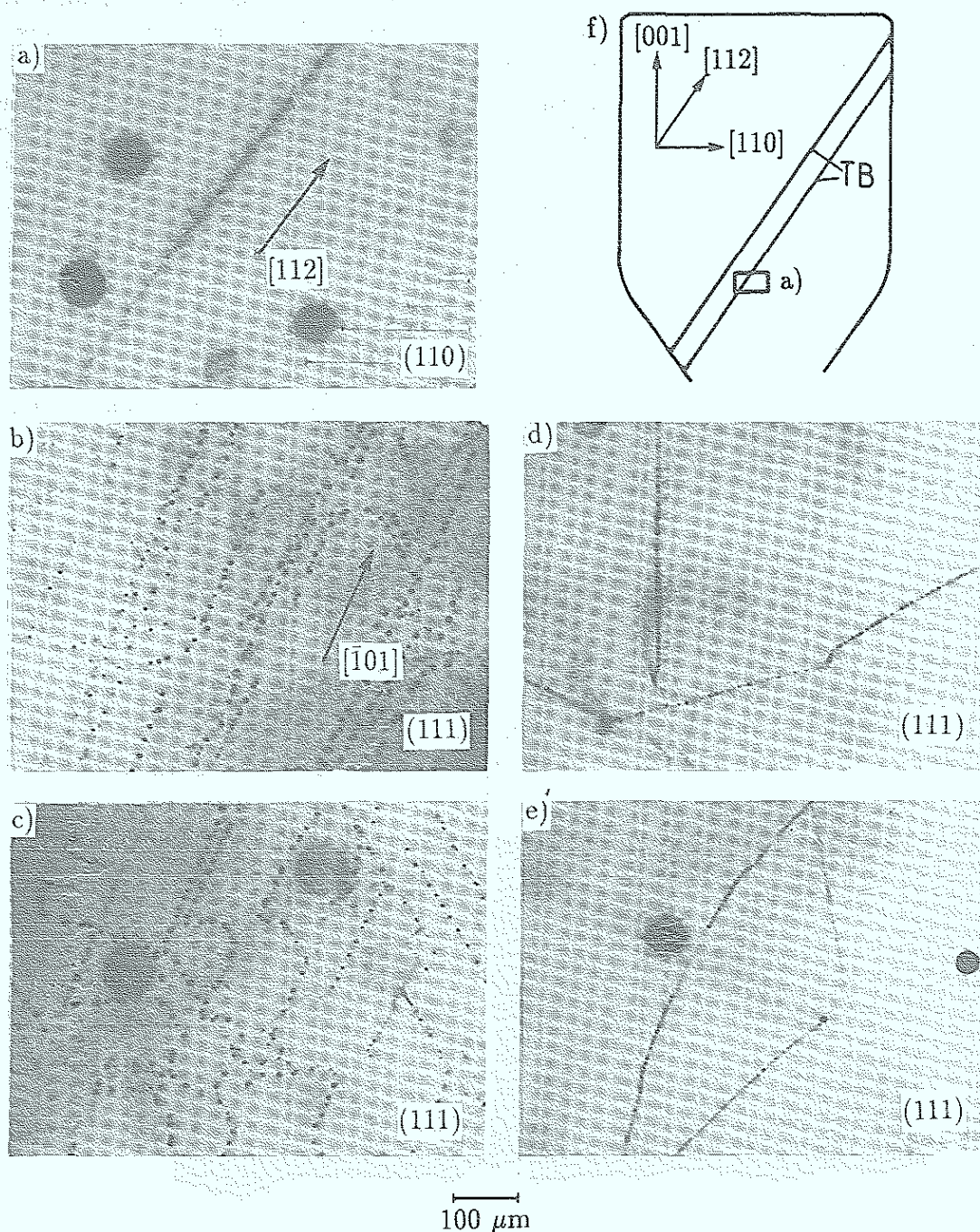


Fig. 85: Dislocation and decoration precipitates on twin boundaries

a) projection of a twin boundary, TB on a (110)-plane, b), c) perpendicular view on a twin boundary (111)-plane, d), e) dislocations in the matrix adjacent to the twin boundary, f) schematic axial cross-section of the VB-crystal from which the image a, b, c, d, e were taken.

a heavily decorated twin boundary. By preparing a sample with a surface parallel to the twin boundary one can show that the precipitates are in fact decorating straight dislocations lines mostly in $[110]$ -directions (see b and c). They are only formed on the twin boundary¹⁴. Focussing on a plane above or below the twin boundary (figure d and e) the dislocation structure resembles that of the normal crystal. Comparing figures b), c) and d), e) we also notice that the dislocation density on the twin boundary is much higher than in the surrounding. The reason for the high dislocation density is not clear; as already mentioned we do not expect dislocation to be necessary for fitting the twin and the crystal. We have also started to image the dislocation structure on twin boundaries by X-Ray-topography. An example is shown in figure 86. The twin boundary is slightly ($\approx 6^\circ$) tilted toward the image plane. The dislocation structure below the intersection line AA' is characterized by a high density of straight dislocation lines in $[110]$ -directions in agreement with the IR-microscopy results. Since the XRT-image is taken in reflection geometry only surface near dislocation can be seen. Above the intersection line AA' the image exhibits the dislocation structure in the matrix close to the twin boundary. In agreement with the IR-microscopy result a much lower dislocation density is observed. Our result also agree with observations by X-ray topography for InP [124]. In the latter work the Burgervectors were determined as parallel to $[112]$ -directions, i.e. the dislocations on the twin boundary are edge dislocation of a type which is not found in the crystal itself. The same conclusion will be drawn for GaAs from the polarisation microscopy results discussed in section 3.4. Since the Burgervectors of the twin boundary dislocations are parallel to shear displacement vectors $\frac{1}{6} a [112]$, which would form a stacking fault layer, it was suggested in ref. [124] that twin formation is strongly related to the presence of these dislocations. This conclusion is somewhat doubtful since twins can also be formed in dislocation free crystals [127]. An alternative explanation for the high concentration of dislocations may be a lower yield for shear on the twin boundary possibly due to change of the second nearest neighbour atom configuration across the twin boundary compared to that in the matrix. One may speculate that this could lower the Peierls potential on the twin boundary as compared to a normal (111) -slip-plane.

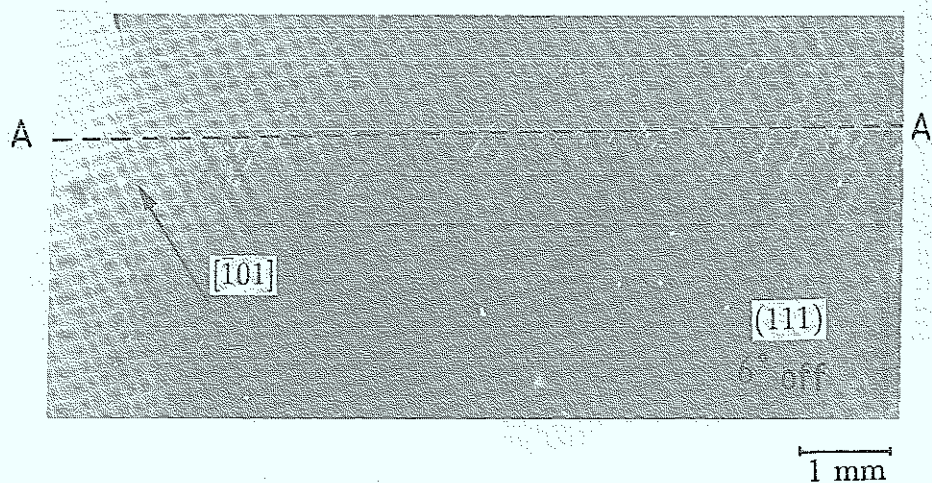


Fig. 86: X-ray topography in reflection intersecting the sample surface under 6° along the line AA'.

¹⁴It should be noted that the error margin for this result is the focal depth of the microscope $\approx \pm 5 \mu\text{m}$.

Another question how is the planar dislocation network on the twin boundary connected with the dislocation network in the matrix also remains unanswered. It seems that both networks are rather independent, i.e. interconnecting dislocation are only very rarely found. It is also interesting that no "crossing" of matrix dislocations through the twin boundary can be observed. This is in agreement with ref. [121]. H. Klapper showed that crossing of twin boundaries by dislocations only occurs in materials which form twins with quasi-parallel lattices on both sides of the boundary. For GaAs-requiring a 180° -rotation – the twin boundary acts as a source or a sink, respectively for dislocation. This is shown in figure 87. Another example are the $[001]$ -dislocation lines forming a small angle grain boundary in the crystal (see figure 88), which cannot be observed in the twin lamella, dislocations stop at the lower twin boundary (figure 88c). It is very interesting to note that from the top twin boundary $[001]$ -dislocation lines are emerging again to form a continuation of the small angle grain boundary (see illustration in figure 88a and darkfield image 88b), although the crystal below the twin lamella is at no time during the crystal growth connected to those parts above the lamella¹⁵ except through the twin lamella itself. Since the small angle grain boundary does not exist in the twin lamella as such it may be present e.g. as a dislocation network connected at the top and bottom of the twin lamella to the small angle grain boundary but spreading out within the twin. Further experiments are necessary for a better understanding of the interaction of matrix dislocations with twin boundaries and the dislocation structure on the boundary itself.

The fact that dislocation crossing of a twin boundary is unlikely – i.e. the twin boundary acts as a barrier for gliding dislocation, could help to understand the formation of a $\sim [111]$ b $\sim [112]$ dislocation on the twin boundary. Dislocation loops lying on (111) -glide planes which intersect the twin boundary may generate dislocations along the intersection lines ($[110]$ -directions) when expanding on their original glide plane as a result of thermal stresses, because the expansion is stopped along the intersection line of the glide plane and the twin boundary.

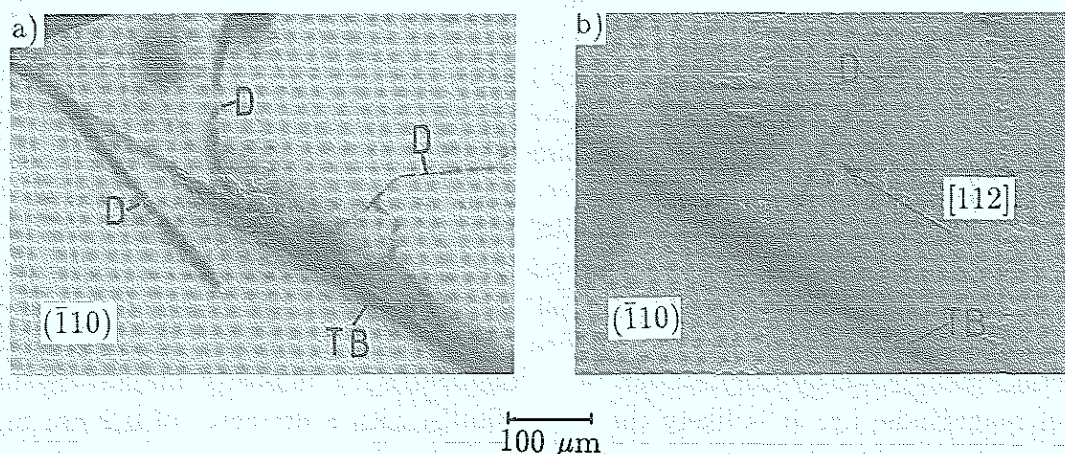


Fig. 87: Darkfield image of undoped GaAs containing a twin boundary, TB, which acts as a sink or source, resp. for dislocations, D of the adjacent matrix.

¹⁵Note that the twin lamella extends from one side of the crystal to the other.

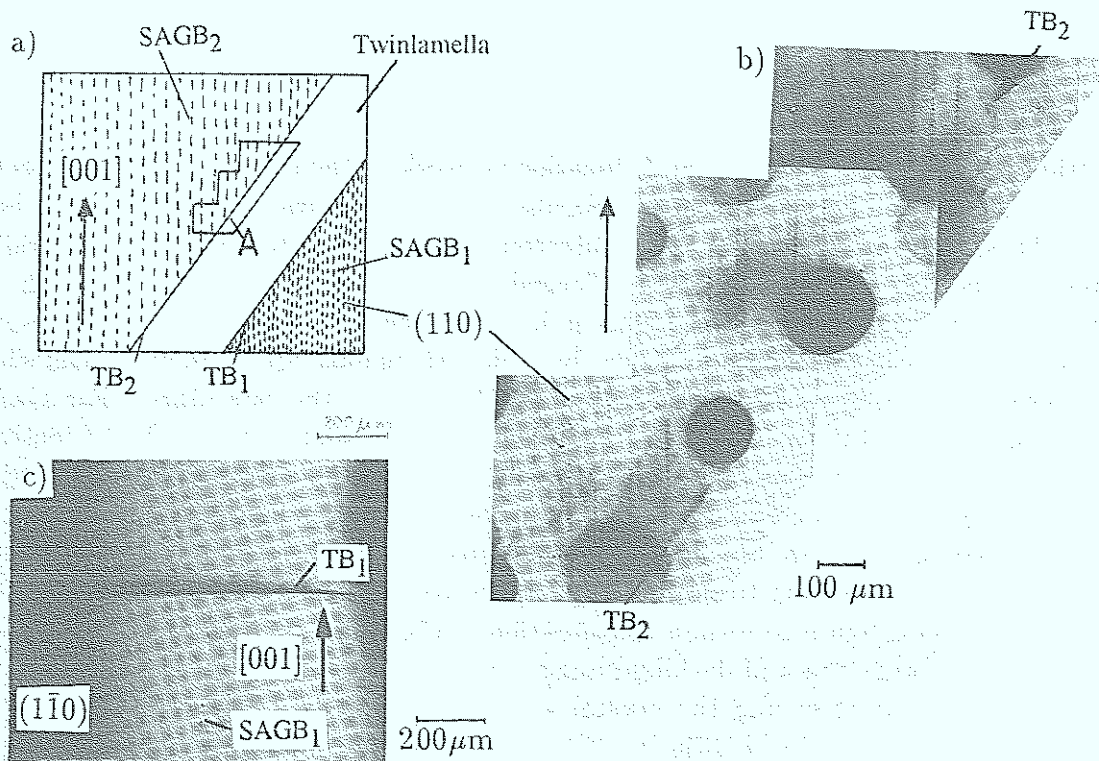


Fig. 88: a) Schematic (110)-cross-section through a crystal which contains a twin lamella and a small angle grain boundary above and below the twin lamella. b) Darkfield image of area A. c) (110)-cross-section: DIC-image of the photoetched surface showing the lower twin boundary, TB, and the lower small angle grain boundary, SAGB₁¹⁶

3.3.3 Influence of Stoichiometry on As-precipitation

Stoichiometry dependent effects can be studied in one single crystal because due to macrosegregation the composition along the growth axis changes over a large range. The data presented in this section have been obtained from a undoped crystal which was grown from an initial melt composition of $\frac{[Ga]}{[As]} \approx 1.01$ increasing during the growth by macrosegregation to 1.25. At this point constitutional supercooling generated cell formation due to the large excess of Ga (area (b) of figure 89f). At the seed end of the crystal the size and distribution of the As-precipitates are quite similar to those typically observed in crystals grown from a stoichiometric melt composition (see figure 67 and 68). The average size and number of precipitates decreases continuously further up the crystal. This qualitative decrease, however must be weighted by the fact that the scattering intensity of precipitates (as shown in chapter 2) depends very strongly on its diameter ($I_s \sim d^6$). We do not yet know the resolution of the darkfield technique with regard to the size of precipitates. Calibration by TEM-studies show that precipitates with a diameter of $\approx 0.3 \mu\text{m}$ can be nicely imaged. Decreasing the size of the precipitate by only 30 % lowers the scattering intensity already by one order of magnitude, i.e. it is likely that precipitates with a diameter of $0.2 \mu\text{m}$ may

¹⁶The dislocation density below the twin lamella is much higher than above. As a result individual dislocation on the one hand cannot be resolved in a darkfield image below the lamella and on the other the SAGB₂ is not seen on the photoetched surface above the lamella because the dislocation density is too low.

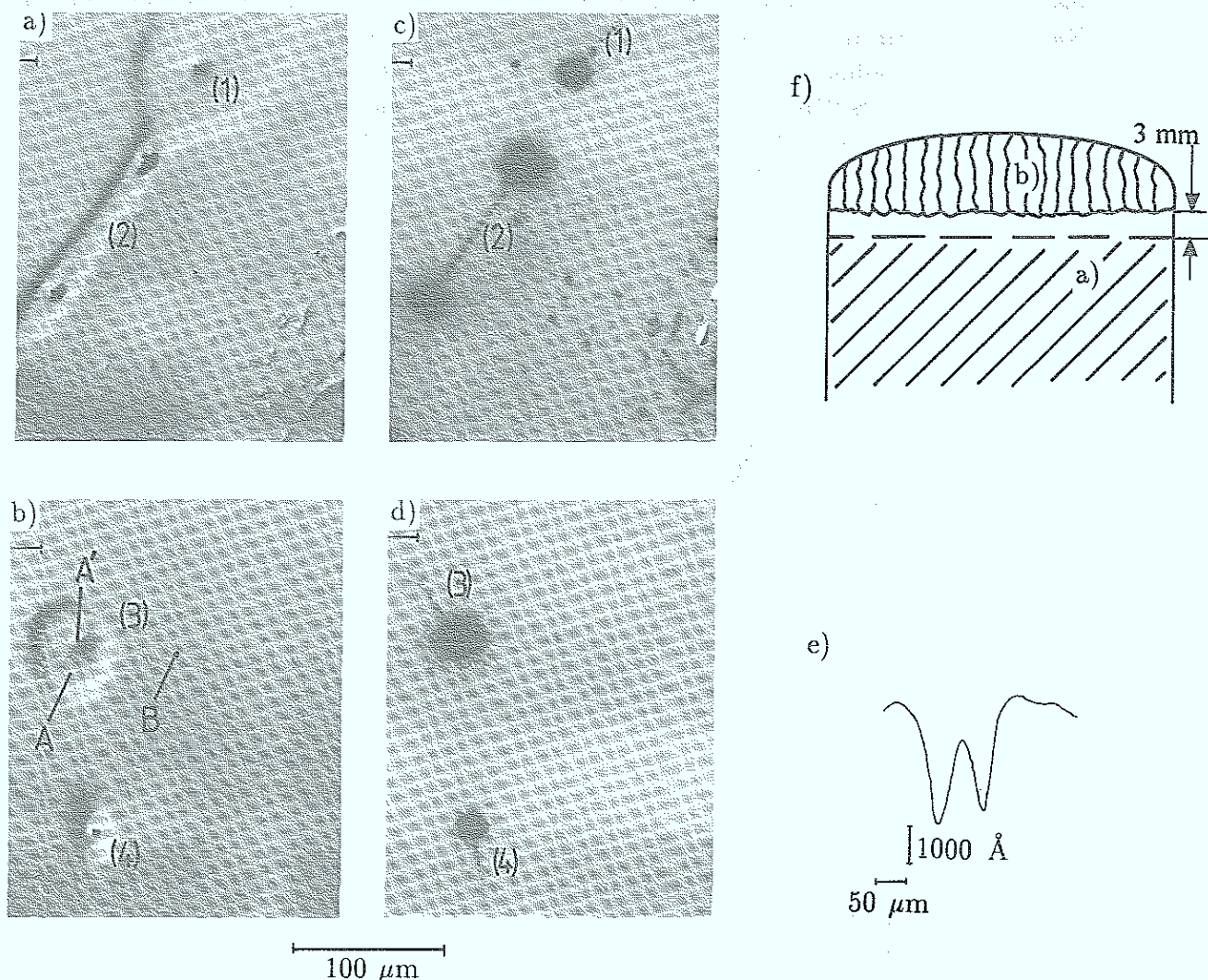


Fig. 89: a), b) DIC-images of photoetched surface in region A. c), d) Darkfield image of identical areas shown in a, b). e) Photo-etching profile observed in region A of the crystal around dislocations.

not be visible any more by this technique or in other words the strong reduction in the number of visible precipitate along the growth axis may strongly exaggerate the real situation. Still precipitates can be resolved even in the tail end very close a) to the onset of constitutional supercooling. In this area photo-etching profiles are found which are typical for material grown from Ga-rich melts (see also section 3.1). The mechanism underlying the increased etch rate (region A) is not yet clear and will be subject of further investigations. It has been speculated [9] that native acceptors e.g. Ga-antisites may play a role for increasing the etching rate. This assumption is not consistent with the fact that As-precipitates are formed under the same conditions i.e. the surrounding (region A) of dislocations (1, 2, 3, 4) – decorated with As-precipitates – shall be dominated by Ga-antisites. Assuming that the As-precipitation is enhanced by the absorption of Ga-vacancies at the dislocations and the associated release of As-interstitials (see section 3.3.1 (iv)) we would expect rather As-antisites to be formed in the surrounding of the dislocation. These arguments are based on the assumption that the precipitates detected by the darkfield technique are of arsenic nature. It has

been shown in ref. [125] that As-decoration precipitates can be detected in GaAs by Ramanscattering technique. In the presence of a As-precipitates close to the sample surface the TO-phonon mode of hexagonal As can be found in the Ramanscattering spectrum $TO_{As} : \approx 200 \text{ cm}^{-1}$). The spectra shown in figure 90 have been obtained from sample regions comparable to those (A, B) indicated in figure 89; the result in figure 90 indeed confirms that the precipitates in crystal regions grown from melt, which is highly rich in Ga, are still of arsenic nature.

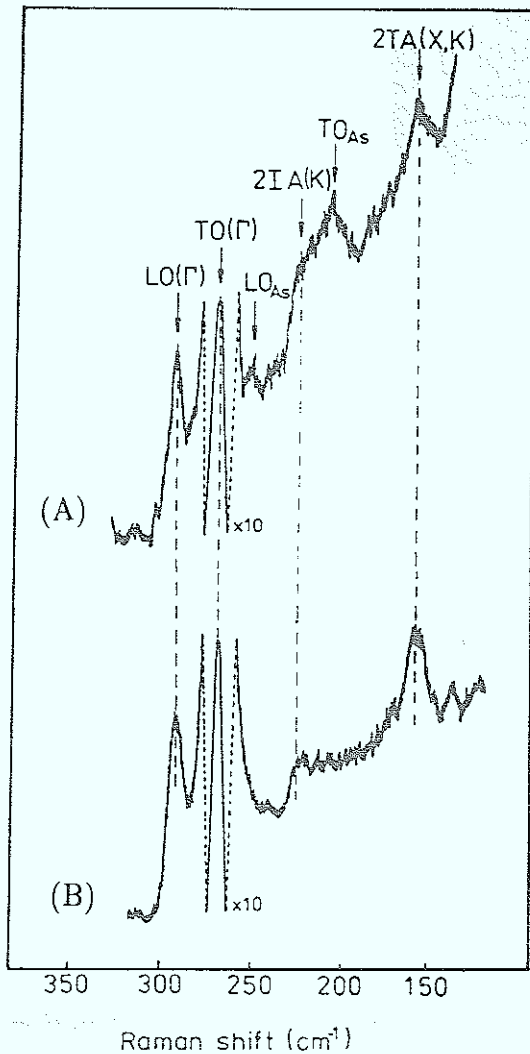


Fig. 90: Ramanscattering spectra taken at sample areas comparable to A and B in figure 89.

It should be noted that the result of As-precipitates being the dominant precipitates even for GaAs which is grown from a Ga-rich melt ($Ga/As = 1.25$) has also been shown for LEC-material (slightly n-type doped) [68]. The size and number of As-precipitates decreases with increasing content of Ga in the melt.

Similar to crystals grown from stoichiometric melts As-precipitates grow further upon post growth annealing treatment at $950 \text{ }^\circ\text{C}$ also for crystals grown from Ga-rich melts. During this annealing treatment As-precipitates grow to a visible size even close (see figure 91) to the area where constitution supercooling commences; i.e. As-precipitates are formed in the material which has been grown for a melt with about 25 % more Ga than As. This result indicates that stoichiometric (50 % Ga, 50 % As) GaAs can only be grown from a melt with $\frac{[Ga]}{[As]} \gtrsim 1.2$. The growth of such crystal however, will be strongly hampered by the destabilizing effects of constitutional supercooling.

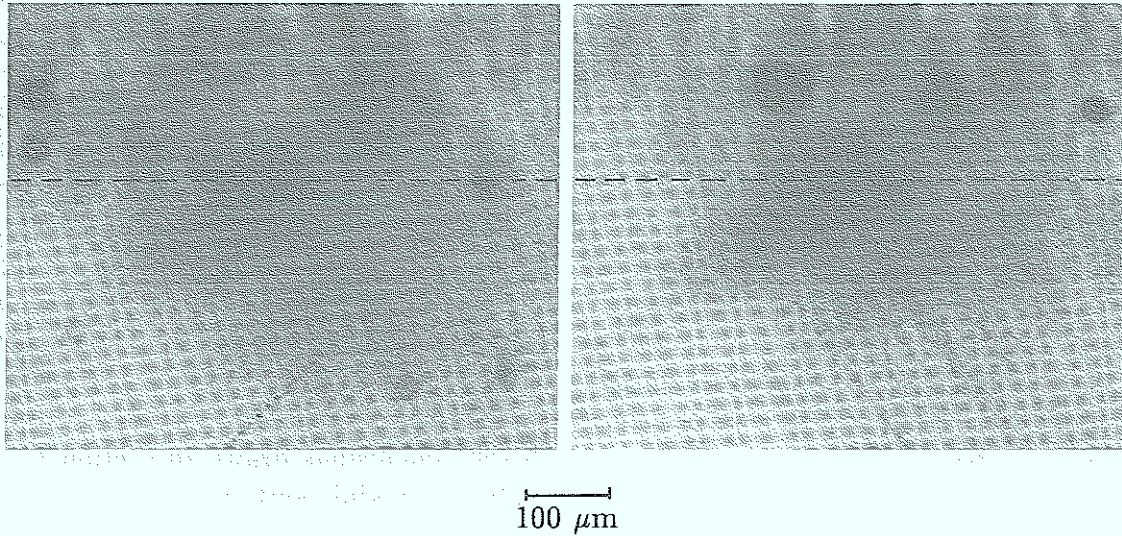


Fig. 91: Darkfield image of a “Ga-rich” material after post growth annealing at 950 °C for 20 h. The dashed lines indicates the beginning of cell formation due to constitutional supercooling.

3.4 Application of polarized light

Polarization microscopy providing birefringence contrast between crossed polarizers should be able to reveal the stress field of dislocations and to determine the type of the dislocation by using simple extinction rules. Unfortunately the interpretation of the image contrast is often not straightforward, particularly if the dislocations are viewed from the side (as in this paper). Also it is yet not understood why no screw dislocations have been identified in III-V-crystals (with possibly one exception [17] and why dislocations observed by this technique often seem to be terminated within the crystal.

The interpretation of birefringence images is complicated through the influence of decoration (As-precipitates or “Cottrell” atmospheres) of the dislocations and the strong effect of background stresses. Theoretical calculations by Tanner [29] showed that decoration may change the extinction rules impeding the discrimination between different types of dislocations. There is strong theoretical and experimental evidence [17, 19, 27] that background strains ($\gtrsim 10^{-6}$ [19]) affect the contrast of dislocations and that these strains are present in all samples which are thicker than about 1 μm [28]. There are also some controversial theoretical results about the dependence of the image contrast of a dislocation on its depth within the crystal. In contrast to Tanner [29] from calculations of Löscke et al. [27] we expect the birefringence image to be independent of the position of the dislocation. The difference between the two results are probably due to different assumptions regarding the long range stress of dislocations.

In the following we will discuss birefringence images for undoped and doped VB-crystals and compare these results with the different contrast interpretations found in the literature. We will also briefly study the “pseudo”decoration precipitates which have been discussed in section 3.3.1). In the second part we will present some images of dislocations in doped crystals obtained by differential interference contrast.

3.4.1 Birefringence images:

The birefringence contrast of dislocations viewed from the side is similar to that shown in figure 92a, 93a, 94a, 95b, 96a and 99a, c, i.e. the dislocation line becomes visible by a bright to dark contrast transition perpendicular to the dislocation. This type of contrast has also been observed ref. [11, 15, 23, 30]. The position of the dislocation can be found by comparing the birefringence image with a dark field image (upper half of figure 92a, 93b, 96b, 99b, d) or a phase contrast image (figure 94b). The birefringence contrast is largest when the dislocation line is oriented to the crossed polarizer and analyzer at 45° and there is no contrast at 0° as shown in figure 92. Such an extinction rule is expected for edge dislocation since for this defect the normal modes are linearly polarized [16] at 0° and 90° , respectively to the dislocation line. Löscke et al. [27] showed that the bright dark structure perpendicular to the dislocation can be observed if the light beam is parallel or tilted but not perpendicular to the slip plane and if background stresses are superimposed. The small angle grain boundary shown in figure 92 consists out of edge dislocations with a Burgersvector probably normal to the sample surface (110). This is consistent with the conclusions drawn in section 3.3.2, i.e. the dislocations must be attributed to a (110) [110] glide system.

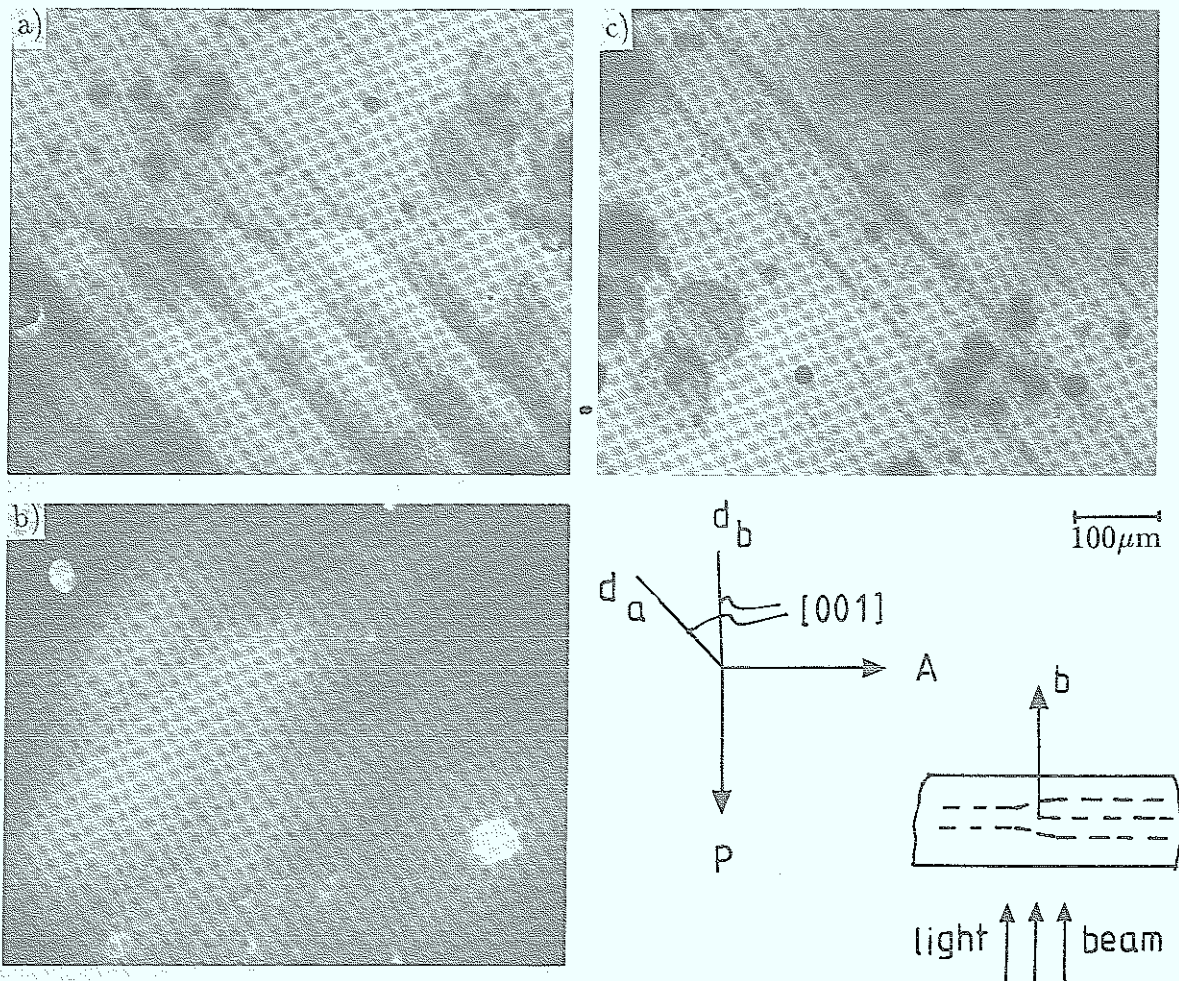


Fig. 92: Comparison of birefringence - and darkfield images of the identical sample area:

- a) birefringence-image of a small angle grain boundary. For a direct comparison the upper part of the dark field image (c) has been overlaid
- b) birefringence image taken with the dislocation line almost parallel to the direction of polarisation
- c) darkfield image.

As shown by Tanner [29] the discrimination between different types of dislocations by extinction rules may be difficult if the stress field around the dislocation is determined by decorating defects. Since the dislocation shown in figure 92 are indeed decorated with arsenic precipitates it is important to find out whether their stress field is dominating the birefringence contrast. From the birefringence image of dislocations under high magnification we find that the structure of the contrast – i.e. dark bright contrast normal to the dislocation line – is the same at, as well as between adjacent precipitates indicating that they do not determine the contrast. The image shows that the dislocation line is not straight, it exhibits arches between the precipitates which seem to act as pinning point against any motion of the dislocation. From the previous arguments it is clear that the image plane is not identical with the slip plane of the dislocation, i.e. the formation of arches is very likely due to climbing processes. It should be noted that the result in figure 93 also proves high magnification birefringences contrast an excellent technique to reveal details of the dislocation lines. A comparable technique – X-ray-topography – cannot offer a similar resolution.

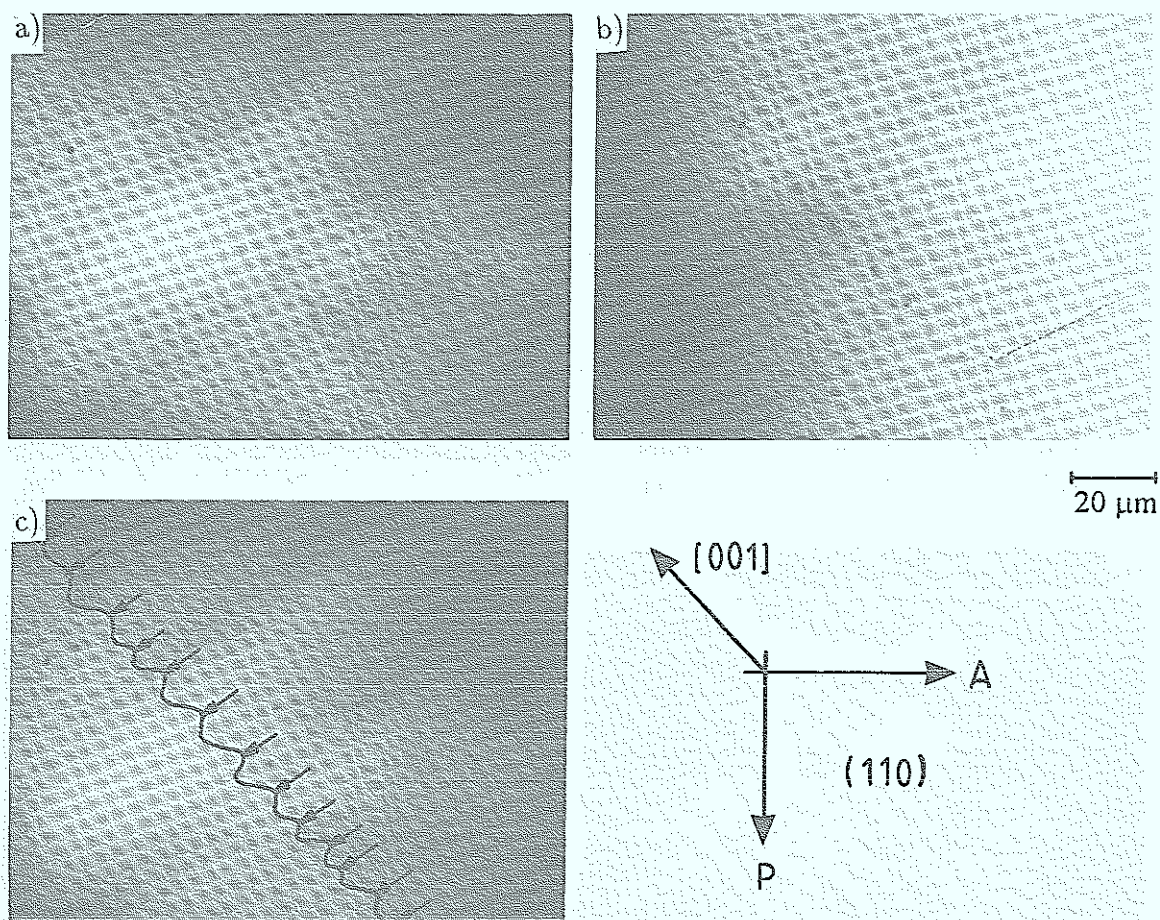


Fig. 93: Comparison of birefringence - and darkfield images of dislocation shown in figure 92 at five times higher magnification.

- a) birefringency
- b) darkfield
- c) identical to a) the weak contrast of the dislocation (precipitates) has been elucidated by the solid line (arrows)

Birefringence images for dislocation with a different “decoration” is shown in figure 94 for a Te-doped sample. As discussed in section 3.1 the zone around the dislocation is characterized by a decrease of the free carrier concentration (figure 94b: Phase contrast) and no precipitates along the dislocation have been found. In spite of a completely

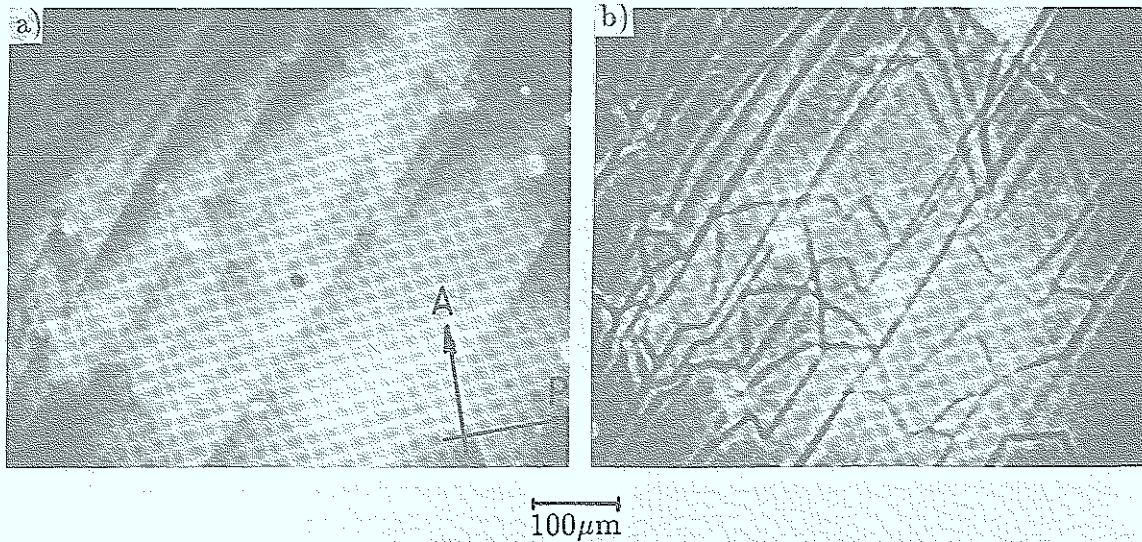


Fig. 94: Comparison of birefringence and phase-contrast images of identical sample areas in Te-doped GaAs.

different type of decoration the same birefringence contrast – i.e. bright dark normal to the dislocation line – is observed. This indicates that decorations of dislocations characteristic for GaAs is not important for the formation of the birefringence contrast. It appears that the stress field of the dislocation itself together with background stresses are the dominating factors. Variations in the free carrier concentration or in the number of doping defects do not seem to generate large stress field. This is also apparent from the results in figure 95. Phase contrast (a) which is sensitive to changes in the refractive

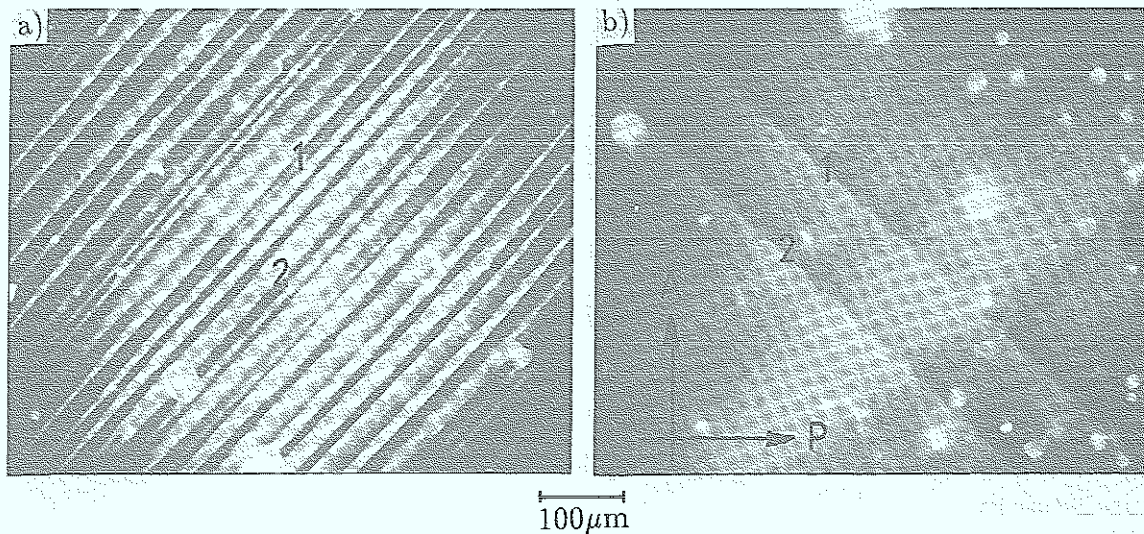


Fig. 95: Comparison of birefringence and phase contrast images for growth striation and dislocations in Si-doped LEC-GaAs.

index and free carrier concentration (see section 3.1.2) clearly reveals growth striations and the bright Cottrell atmospheres (increased free carrier concentration) of the two dislocations (1) and (2). In the birefringence image (b) growth striations are almost invisible, dislocation however, though also associated with variations in free carrier concentration are clearly visible, i.e. the birefringence contrast of the dislocation cannot be caused by the decorating "Cottrell" atmosphere.

Another example showing that the decoration of dislocations is not dominating the birefringence contrast is presented in figure 96. It compares a darkfield – and a birefringence image of dislocations which exhibit almost no decorations (1), (2) and (3) but a strong birefringence contrast on the one hand and dislocation (4) strongly decorated but almost invisible in the birefringence image on the other.

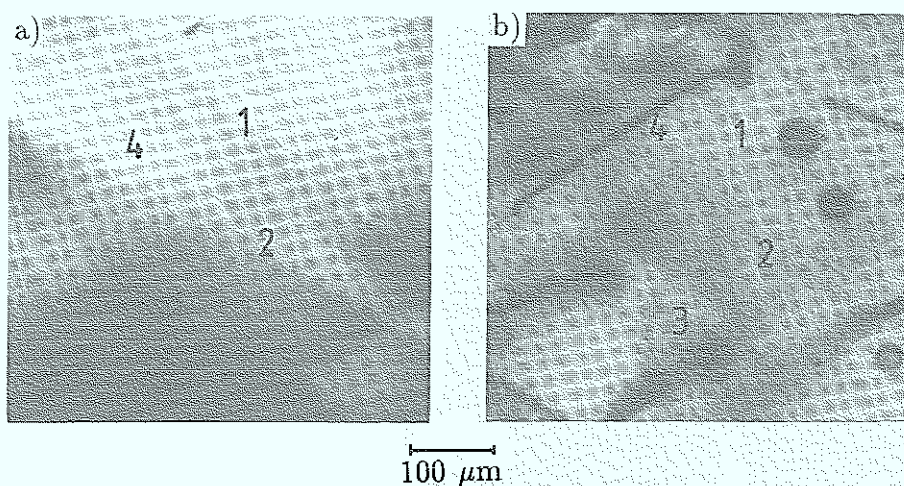


Fig. 96: Comparison of birefringence – and darkfield images for identical sample areas containing dislocations with a different degree of decoration.

The birefringence contrast of edge dislocations which are embedded in background stresses and which are viewed perpendicular to their slip plane (figure 97) appear as bright lines. When rotating the crossed polarizer/analyzer system they become dark lines. This follows from theoretical calculations by Löschke et al. [27]. Dislocations on twin boundaries which have been discussed in section 3.3.2 show exactly this type of contrast as shown in figure 97 and 98. The sample in figure 97a contains a twin boundary which is tilted by 6° against the surface of the sample as indicated in figure 97c. Since the sample is about $300 \mu\text{m}$ thick the dislocation structure in figure 97a extends over a distance of 3 mm. The dislocations appear as mostly bright (1) but in some cases also as dark (2) lines (due to an opposite sign of the dislocation?). The dislocations are oriented in $[110]$ -direction. By rotating (see figure 98) the crossed polarizer/analyzer system (or the sample) bright (dark) lines appear dark (bright). The contrast disappears if the dislocation line is parallel to the polarizer/analyzer system. This result shown in figure 97 and 98 cannot be understood, if we assume that the birefringence contrast is determined by the stress field of As-precipitates which

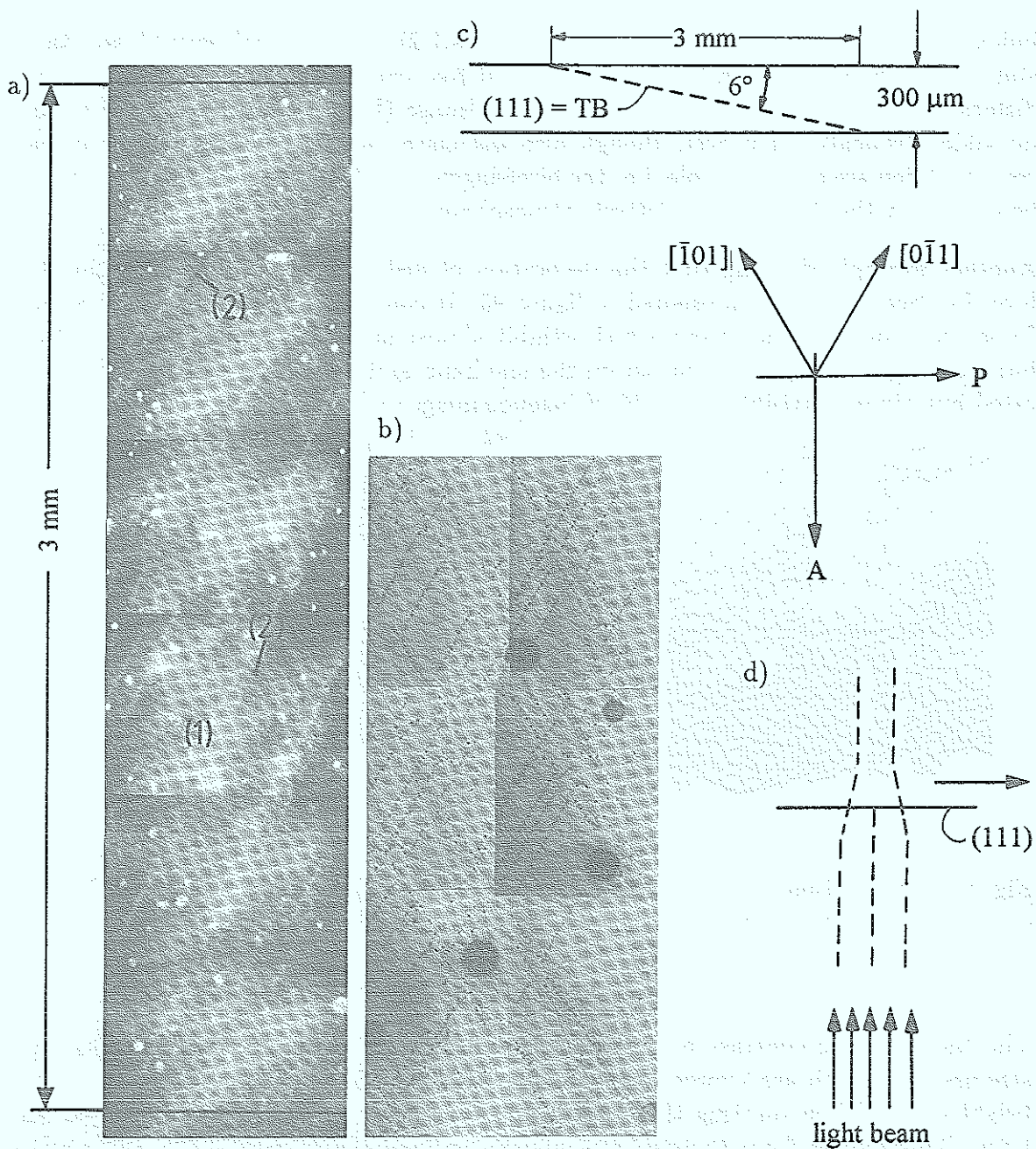


Fig. 97: a) Birefringence image of the dislocation structure found on twin boundaries
 b) DF
 c) cross-section of the sample containing a twin boundary
 d) orientation of the light beam with regard to the slip plane of the dislocation.

are decorating the dislocation of twin boundaries as demonstrated in figure 97b. We therefore conclude that those dislocation have edge character with a Burgersvector parallel to the twin boundary. Because the dislocation line has a $[110]$ -direction, the Burgersvector becomes parallel to $[112]$ in agreement with the conclusions already drawn in section 3.3.2.

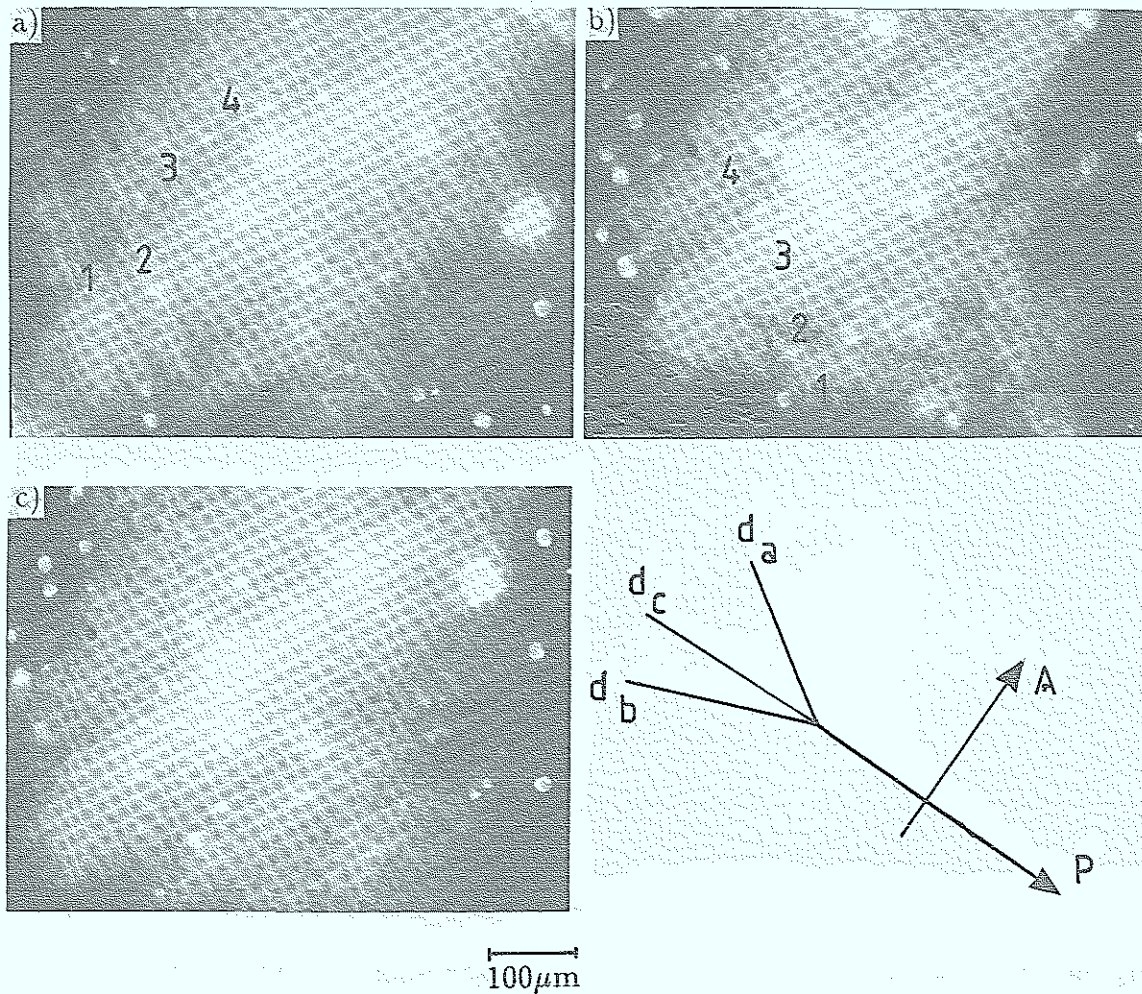


Fig. 98: Dependence of the contrast of dislocation shown in figure 97 on the orientation of the dislocation with respect to the crossed polarizers.

In section 3.3.1 we discussed decoration features (“pseudo decoration”) which appear rather disconnected from the rest of the dislocation network. By comparing IR- with X-ray topography images of identical areas we were able to show that these features were not associated with dislocations. This is confirmed by the result of figure 99 which compares the dislocation structure seen in darkfield images (b, d) with birefringence images (a, c). The latter do not show any stress field around the “pseudo decoration” precipitates, A. In figure c, individual precipitates of (A) can be seen, because they are probably very large and generate an absorption or diffraction image; birefringence contrast, however are not associated with (A).

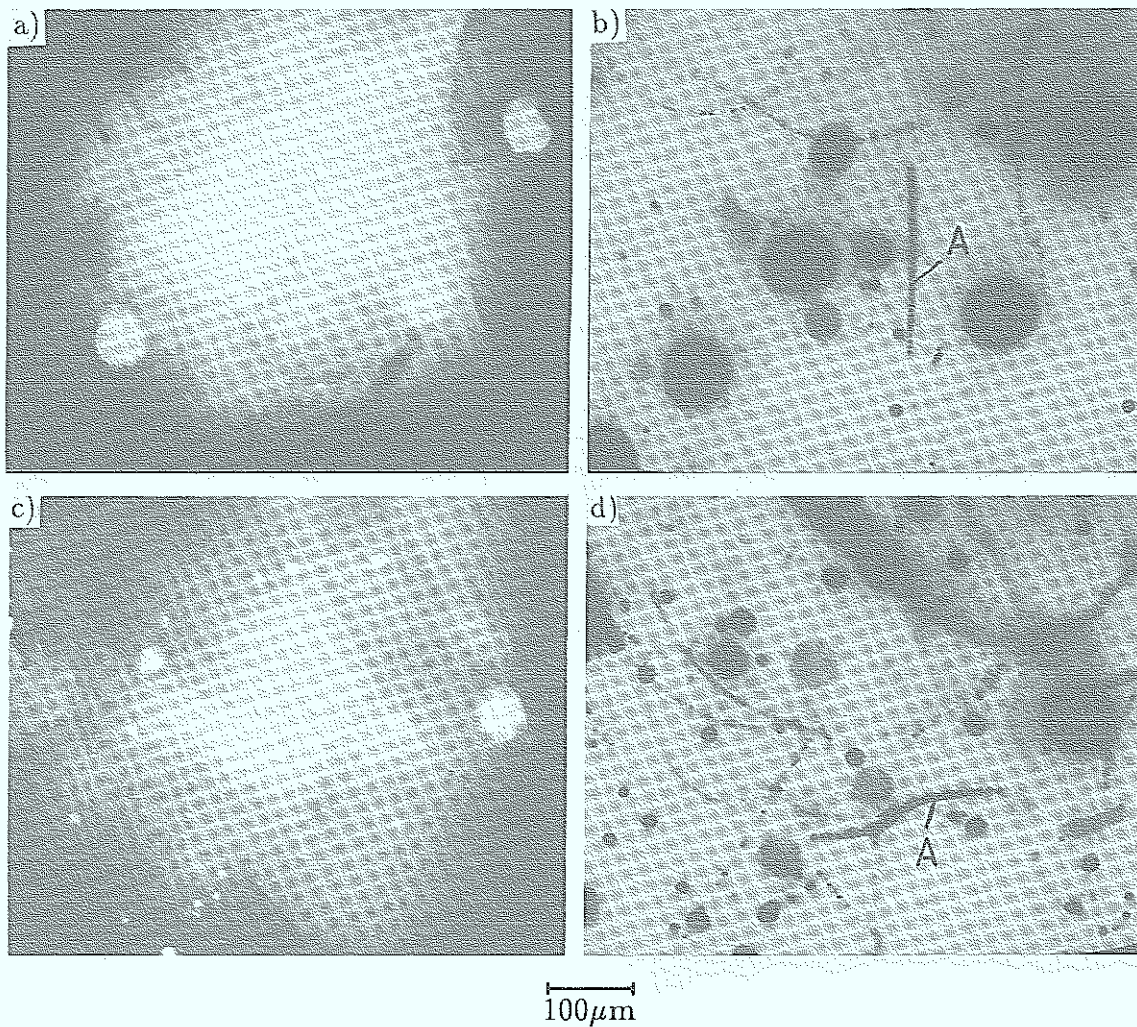


Fig. 99: Comparison of birefringence – and darkfield images for identical sample areas which contain “pseudo decoration” features (see discussion in sectin 3.3.1).

3.4.2 Differential interference contrast, DIC (Transmission):

As shown in section 2.2 differential interference contrast provides images of surface reliefs giving a 3-dimensional impression. This is due to the fact that a ridge or a hillock on the surface appears bright on one side and dark on the other (shadow). We will show that this technique can also be used to image “Cottrell” atmosphere located within a transparent crystal. As discussed in section 3.1 we may consider a “Cottrell” atmosphere as a cylindrical zone around a dislocation which is characterized by a refractive index which differs by Δn from that in the matrix. The optical path difference (see figure 100) of two interfering light waves which pass through the sample in a distance Δx is given by $\Delta = 2 \Delta n \cdot dD/dx \cdot \Delta x$. The qualitative variation of Δ across the atmosphere is plotted in figure 100b for $\Delta n > 0$ (Te-doped GaAs) and

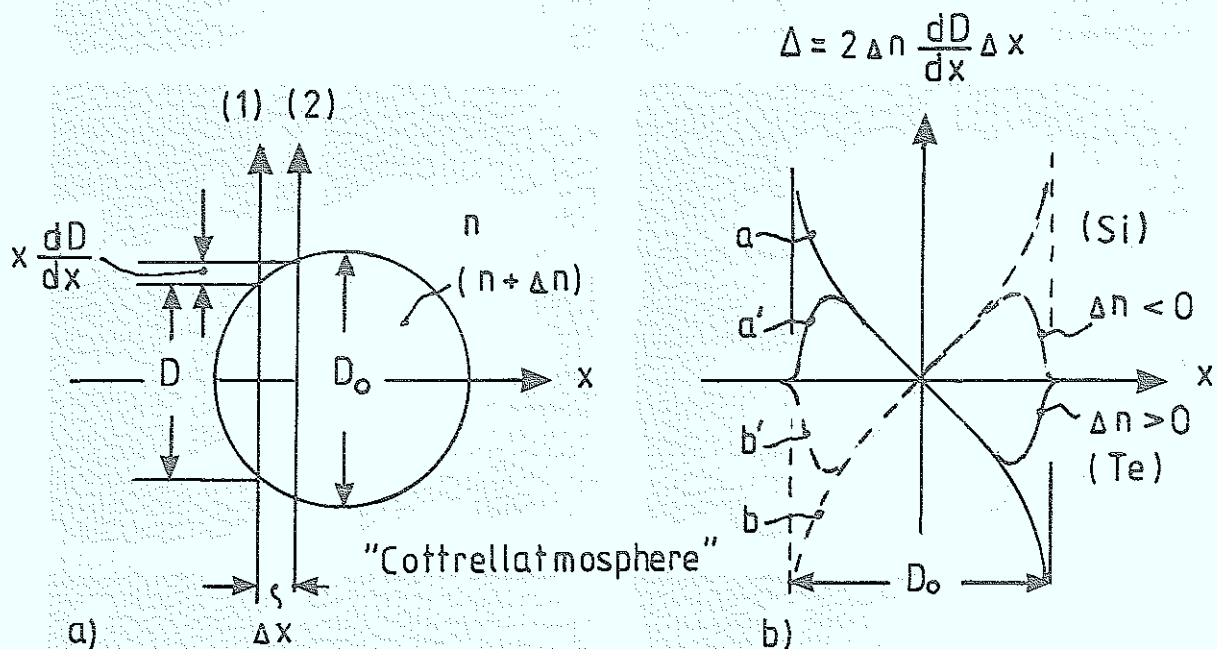


Fig. 100: Illustration of the differential phase developing in a "Cottrell" atmosphere: Δ is the optical path different between the interfering light waves (1) and (2).

$\Delta n < 0$ (Si-doped GaAs). Since Δn is not constant across the Cottrell atmosphere but decreases with increasing distance from the dislocation ($\Delta n \approx 0$ at $x = D_0/2$) the optical path difference can rather be described by the curves (a') and (b') than by (a) and (b) resp. Because the image contrast is proportional to Δ we expect to find a bright-dark¹⁷ contrast (ridge) for Te-doped GaAs and a dark-bright contrast (dip) for Si-doped material. This is confirmed by the experimental results shown in figure 101b) and e). The phase microscopy images (figure 101a) and d)) on the other hand exhibit a bright (dark) contrast for Si (Te) across the whole diameter, D_0 of the "Cottrell" atmosphere.¹⁸ It is obvious from figure 12. in section 2.2. that the maximum contrast is obtained if the dislocation (1) (2) (3) are perpendicularly oriented to the plane in which mode M_1 and M_2 are propagating. In figure 101c) and f) the Cottrell atmosphere of dislocation (1) (2) (3) are almost invisible because they are nearly parallel to the plane (M_1, M_2).

¹⁷It should be noted that the bright-dark (or dark-bright resp.) contrast can be reversed by readjusting the Wollaston prism.

¹⁸If Halo effects are neglected (see section 3.1).

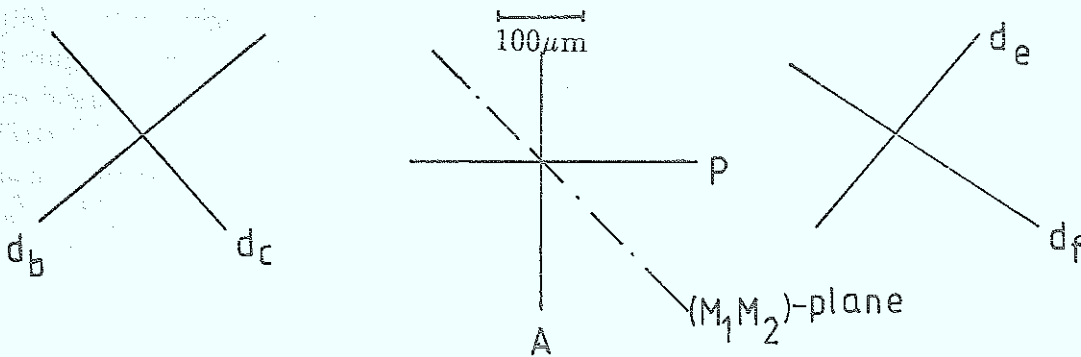
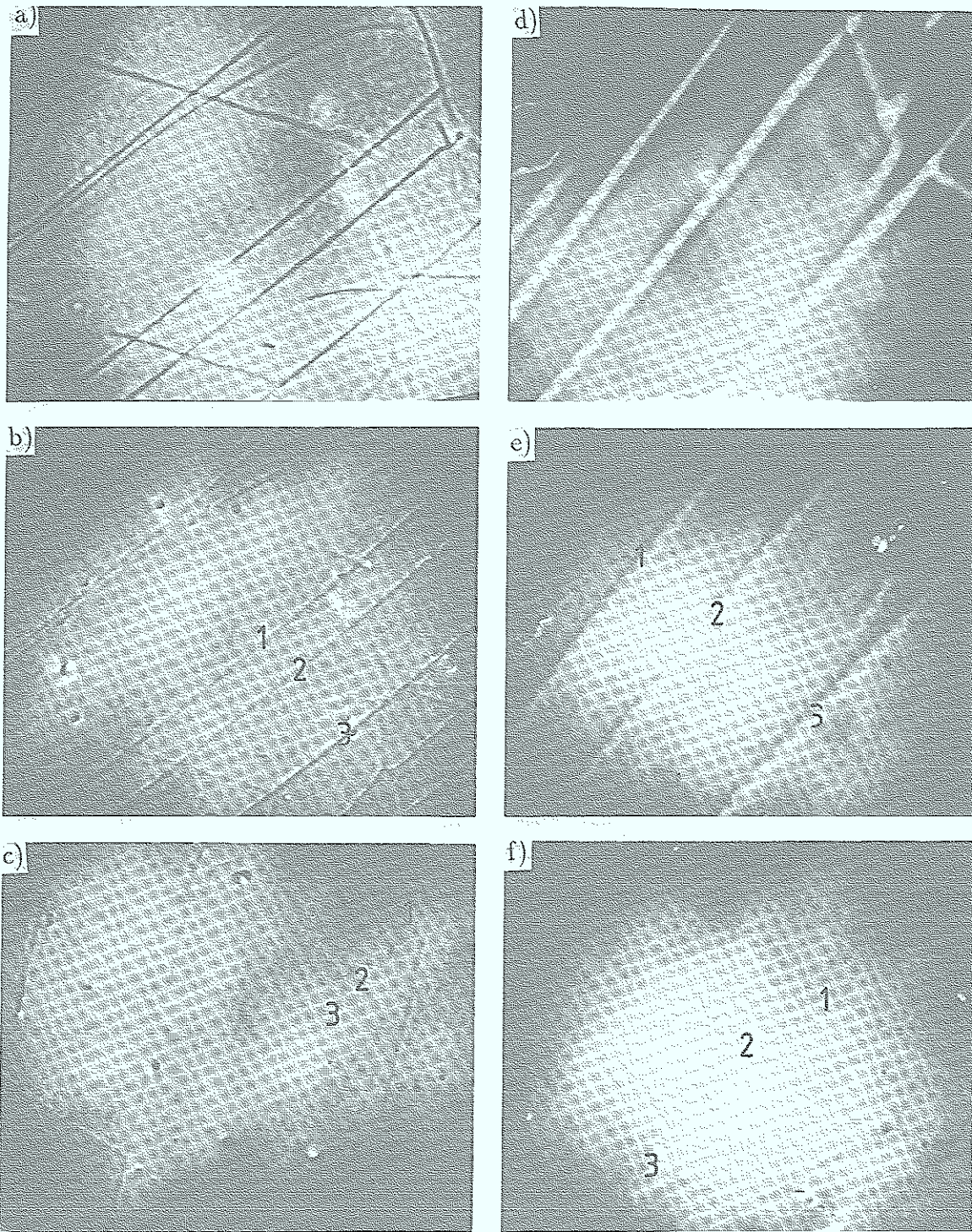


Fig. 101: Comparison of phase microscopy- and DIC-images of Te(a,b,c)- and Si(d,e,f)-doped GaAs:

a), d) Phase microscopy

b), e) DIC-image: the dislocation (1), (2) and (3) are oriented almost perpendicularly to the plane $(M_1 M_2)$

c), f) DIC-image: the dislocation (1), (2) and (3) are almost parallel to $(M_1 M_2)$

4. Conclusions

As a major result of the present work we find phase and differential interference microscopy a simple but effective technique for studying inhomogeneities of free carrier concentration, $\Delta n = \Delta(N_D - N_A)$. Performing a careful analysis employing bright field-, phase- and "Schlieren" contrast we conclude that the NIR-image contrast is due to variations in the refractive index whereas absorption and refraction effect are negligible. Inhomogeneities in the refractive index are attributed to variation of the free carrier concentration, $\Delta n = \Delta(N_D - N_A)$. This agrees with the measured dependence of the refractive index, n on the doping (n-type) concentration and can be theoretically related through the "Kramer-Kronig"-relation to the fundamental absorption process and in particular to interconduction band transitions. Even details such as the improved phase contrast for smaller wavelength can be understood in terms of this model.

Phase microscopy appears as an analyzing technique complementary to photoetching, EBIC and Ramanscattering which are also sensitive to variation in \bar{n} and $N_D - N_A$, respectively. They are, however only surface technique, whereas phase microscopy can also resolve microdefects in the bulk of the sample. This is particular important for annealing studies when identical sample areas shall be compared before and after the annealing treatment. This is not possible for the sample surface which is damaged during the annealing due to evaporation of arsenic at high temperatures. Employing phase microscopy annealing effects have been studied for Si-doped GaAs grown by VB-technique. This material exhibits an increased free carrier concentration around dislocations, which has also been observed by photoetching, EBIC and Ramanscattering. Since the increase of \bar{n} has been attributed to Si-gettering, due to the interaction of Si with the dislocation, it is associated with the term Cottrellatmosphere. Annealing of Si-doped GaAs at 950 °C results in a growth of the Cottrellatmosphere. The growth rate can be attributed to a diffusion process. This result and the very low diffusion constant for Si in GaAs found in this work and in so-called δ -doping experiments are not consistent with Si-gettering forming a Cottrellatmosphere. Also general arguments are presented indicating that the interaction energy between Si and the dislocation is too small to explain the large extension of the Cottrellatmosphere. For these reasons it appears that the term Cottrellatmosphere is misleading and that this atmosphere ought to be rather attributed to a transformation of acceptors into donors. A tentative mechanism is discussed which is based on the assumption that $\text{Si}_{\text{Ga}}\text{V}_{\text{Ga}}$ -complexes are present in the material. There is evidence in the literature that this complex can dissociate above 900 °C; i.e. the Ga-vacancy can perform a hindered diffusion and if it encounters a dislocation it can either contribute to formation of As-precipitates or react with the dislocation resulting in a climbing step and the emission of an As-interstitial. Electrically the defect reaction would transform a $\text{Si}_{\text{Ga}}\text{V}_{\text{Ga}}$ -complex (neutral or acceptor) into a Si_{Ga} -donor. The proposed model would explain why As-precipitates can be formed at dislocations as well as in the matrix and that both types of precipitates are associated with a zone of increased donor concentration. However in agreement with the model such a zone may also be formed without As-precipitates because of the possible reaction of the Ga-vacancy with the dislocation.

Annealing results at higher (>950 °C) temperatures or for GaAs doped with Te are not well understood and require more experiments. Phase microscopy has also been employed for studying glide processes and growth striations. Glide processes become visible because when unlocking a dislocation from its original position the "Cottrell" atmosphere is left behind as a "fingerprint". Inhomogeneities of the doping concentration caused by growth striation are visible by phase microscopy, however their investigation is complicated by the fact that refraction effects cannot be completely neglected particularly for thicker samples. Annealing of growth striation in Si-doped GaAs has been used to study the diffusion of Si which is still controversial in literature. Similar to so-called δ -doping experiments the Si-concentration in our sample is sufficiently low to avoid the Si-diffusion being determined by the migration of Si-pairs ($\text{Si}_{\text{Ga}} - \text{Si}_{\text{As}}$). The present work confirms the low values of the diffusion constant measured by Schubert et al employing δ -doping.

Phase microscopy cannot be used for undoped GaAs since it is only sensitive to variations in the free carrier concentration which are larger than $\simeq 5 \cdot 10^{+16} \text{ cm}^{-3}$. Undoped GaAs is characterized by the presence of precipitates decorating the dislocation. Calibration measurements by TEM which are currently being performed, indicate that precipitates larger than $\approx 0.2 \mu\text{m}$ in diameter become visible in darkfield contrast due to the scattered light. Since the distance between individual decoration precipitates is typically $2 - 10 \mu\text{m}$ the configuration of the dislocation lines is also revealed by darkfield images. This means that darkfield images can provide information about the dislocation structure and precipitation effects:

- (i) Although darkfield images do not allow to determine Burgersvectors of dislocation they provide evidence that the majority of dislocations belong to the (111) [110]-slipsystem with line vectors $\vec{u} = [110]$ and particular [112]. We also observe dislocation of the (110) [110] slipsystem with a [100] linevector and sometimes dislocation of the (113) [110] slipsystem with $\vec{u} = [112]$.

It is interesting that on twin boundaries a dislocation type (111) [112], $\vec{u} = [110]$ is observed which is not present elsewhere in the material. The density of dislocation on twin boundaries is much higher than in the adjacent matrix. It appears that the twin boundary acts as a source or sink for dislocations. It is not clear whether the twin boundary dislocations are related to the formation of twins and how they are interconnected with the dislocation network of the crystal.

- (ii) Dislocation cell structure as well as lineage is observed in VB-crystals. Some evidence is presented against interpreting cell structure as due to constitutional supercooling effects. Lineage has been recently associated with the formation of sessile [110]-dislocations. The present results, however indicate that lineage should be attributed to polygonisation of dislocations.
- (iii) From the configuration of dislocation lines and by comparing decoration features with the associated dislocation (revealed by photoetching) it becomes clear that climbing processes of dislocations play an important role. It should be noted, however that for several decoration features it is not clear whether they are due to climb or glide processes.
- (iv) Due to macrosegregation the stoichiometry of the melt can vary during the growth of one crystal over a large range (e.g. $1.01 < \text{Ga/As} < 1.25$). In agreement with

the literature we find that even for the most Ga-rich melt the crystal still contains As-precipitates, which grow in number and size upon annealing at 950 °C. This indicates that As-rich crystals can be grown from a highly Ga-rich melt ($Ga/As = 1.25$).

- (v) In agreement with the literature we find that As-precipitates grow during annealing at 950 °C and can be dissolved above 1100 °C. During a subsequent annealing treatment at 950 °C the dislocation are decorated again by As-precipitates. It is interesting to note that for Si-doped GaAs the growth at 950 °C as well as the dissolution of As-precipitates at 1100 °C is much more sluggish than for undoped GaAs.

The results of birefringence images of dislocations clearly show that the contrast is dominated by the stress field of the dislocation and by background stresses. The influence of decorating defects (As-precipitates and "Cottrell" atmosphere) on the other hand can be neglected. Birefringence images at high magnifications are an excellent technique to reveal the dislocation line in great detail. The dislocations typical for twin boundaries could be identified as edge dislocations with the slip plane parallel to the twin boundary i.e. \vec{b} has a $[112]$ -direction.

For the first time differential interference contrast in transmission mode was employed to image dislocations. It appears that this technique can provide similar information as phase microscopy.

References

- [1] R. Naeven, Ph.D.-thesis, RWTH Aachen, 1993
- [2] H. Alexander, *Radiation Effects and Defects in Solids* **111**, **112**, 1 (1989)
- [3] M. Althaus, to be published
- [4] I. Yonega and K. Sumino, *J. Appl. Phys.* **62** (4), 1212 (1987)
- [5] M.R. Brozel, S. Clark and D.J. Stirland, *Semiinsulating Materials*, Eds. H. Kukimoto and S. Miyazawa, Ohmska, Tokyo 1986, p. 133
- [6] Y. Fujisaki, Y. Takano *Proc. of 5th Conf. on Semi-insulating III-V Materials*, Malmö, Sweden 1988, p. 247
- [7] P.H.L. Notten, J.E.A.M. van den Meerakker and J.J. Kelly eds. *Etching of III-V Semiconductors: an Electrochemical Approach* (Elsevier, Oxford, 1991)
- [8] R.N. Thomas, S.Mc. Guigan, G.W. Eldridge and D.L. Barrett, *Proc. of the IEEE* **76**, 778 (1988)
- [9] J.L. Weyher, C. Frigeri and P.J. Van der Wel, *J. Cryst. Growth* **103**, 46 (1990)
- [10] O. Pätzold, G. Irmer and J. Monecke, *Cryst. Res. Technol.* **27**, K11 (1992)
- [11] K. Löschke, *phys. stat. sol. (a)* **90**, 573 (1985)
- [12] A.F. Witt (private communication)
- [13] W.L. Bond and J. Andrus, *Phys. Rev.* **101**, 1211 (1956)
- [14] V.I. Nikitenko and L.M. Dedukh, *phys. stat. sol. (a)* **3**, 383 (1970)
- [15] J.W. Matthews, E. Klokholm, V. Sadagopan, T.S. Plaskett and E. Mendel, *Acta Met.* **21**, 203 (1973)
- [16] D.J. Fathers and B.K. Tanner, *Phil. Mag.* **28**, 749 (1973)
- [17] B.K. Tanner and D.J. Fathers, *Phil. Mag.* **29**, 1091 (1974)
- [18] U. Alter, W. Melle, K. Meyer, R. Töpfer, *Kristall und Technik* **10**, 263 (1975)
- [19] D.A. Jenkins and J.J. Hun, *Phil. Mag.* **33**, 173 (1976)
- [20] J.W. Matthews and T.S. Plaskett, *Phil. Mag.* **33**, 73 (1976)
- [21] J.W. Matthews and T.S. Plaskett, *phys. stat sol. (a)* **37**, 499 (1976)
- [22] J.W. Matthews, T.S. Plaskett and S.E. Blum, *J. Cryst. Growth* **42**, 621 (1977)
- [23] D.A. Jenkins, T.S. Plaskett and P. Chandhari, *Phil. Mag. A* **39**, 237 (1979)
- [24] K. Löschke, V. Gottschalch, K. Jacobs and A. Tempel, *Kristall und Technik* **14**, 887 (1979)
- [25] H. Booyens and J.H. Basson, *J. Appl. Phys.* **51**, 4368 (1980)
- [26] H. Booyens, J.H. Basson, and M.B. Small, *J. Appl. Phys.* **52**, 4112 (1981)
- [27] P. Paufler and K. Löschke, *Phil Mag.* **47**, 79 (1983)
- [28] K. Löschke and P. Paufler, *Phil Mag.* **46**, 699 (1982)
- [29] B.K. Tanner, *Phil. Mag. A* **49**, 435 (1984)
- [30] C.Z. Ge, N. Ming, and D. Feng, *Phil. Mag. A* **53**, 285 (1986)
- [31] S.S. Jiang, A.R. Lang and B.K. Tanner, *Phil. Mag. A* **56**, 367 (1987)
- [32] N. Ming and C.Z. Ge, *J. Cryst. Growth* **99**, 1309 (1990)
- [33] Z. Laczik, P. Török, G.R. Booker and R. Falster, *Inst. Phys. Conf.* **117**, 785 (1991)
- [34] A. Altmann, Ph.D Thesis RWTH Aachen, 1994
- [35] P.C. Montgomery, J.P. Fillard, *Electronics Letters* **25**, 89 (1989)
- [36] J.S. Blakemore, *J. Appl. Phys.* **53** (10) R145 (1982)
- [37] E. Haga, K. Kimura, *J. Phys. Soc. Japan.* **19**, 1596 (1964)
- [38] H.Ch. Alt and G. Packeisen, *J. Appl. Phys.* **60** (8), 2954 (1986)

- [39] D.J. Stirland, M.R. Brozel and I. Grant, *Appl. Phys. Lett.* **46** (11), 1066 (1985).
- [40] D.J. Carlson, A.F. Witt, *J. of Cryst. Growth* **108**, 508 (1991)
- [41] H. Beyer, *Phasenkontrastverfahren*, Leipzig 1965
- [42] A.H. Bennett, H. Osterberg, H. Jupnik and O.W. Richards, *Phase microscopy*, John Wiley & Son, Inc., New York, 1951
- [43] M. Born and E. Wolf, *Principles of Optics* (Pergamon, Oxford, 1970), p. 424
- [44] P. Schloßmacher, RWTH Aachen, 1991
- [45] A.G. Cullis, P.D. Augustus and D.J. Stirland, *J. Appl. Phys.* **51** (5), 2556 (1980)
- [46] K. Lösckke, and A. Tempel, *Kristall und Technik* **15**, 55 (1980)
- [47] T. Ogawa, DRIP, J.P. Fillard, ed., (Elsevier, Amsterdam; 1985) p. 1
- [48] P. Gall, J.P. Fillard, M. Castagne, J.L. Weyher and J. Bonnafe, *J. Appl. Phys.* **64** (10), 5161 (1988)
- [49] L. Bergmann and C. Schaefer, *Lehrbuch der Experimentalphysik III*, Berlin 159, p. 308
- [50] J.L. Weyher, private communication
- [51] H. Leancy, *J. Appl. Phys.* **53** (6), R51 (1982)
- [52] C. Frigeri, *Inst. Phys. Conf.* **87**, 745 (1987)
- [53] E.P. Visser, P. van der Wel, J.L. Weyher, and L.J Giling, *J. Appl. Phys.* **68** (8), 4242 (1990)
- [54] H.H. Hopkins, *Le contraste de phase et le contraste par interference*, *Revue D'Optique*, 1952 (Paris) M. Francou ed., p. 142
- [55] A. Castaldini, A. Cavallini, B. Fraboni, B. Mendez and J. Pigueras, *Proc. of DRIP 5*, Santander (1993), to be published
- [56] Y.M. Chu, D.B. Darby and G.R. Booker, *Inst. Phys. Confer. Ser. No. 60*, Section 7, p. 331 (1981)
- [57] P.W. Hutchinson and P.S. Dobson, *Phil. Mag.* **30**, 65 (1974)
- [58] Ch. Kittel, *Introduction to Sol. State Phys.* 3rd Ed. 1966, p. 227
- [59] G. Schöck in *Dislocations in Solids*, Vol. 3, ed. by F.R.N. Nabarro (1980), p. 127
- [60] *Handbuch der Physik*, S. Flügge ed. Vol. 25/2a (1967) p. 29
- [61] F. Stern, *Phys. Rev.* **133** (6A), 1653 (1964)
- [62] D.D. Sell, H.C. Casey and K.W. Wecht, *J. Appl. Phys.* **45** (6), 2650 (1974)
- [63] E. Burstein: *Phys. Rev.* **93**, 663 (1954)
- [64] J. Zoroofchi and J.K. Butler, *J. Appl. Phys.* **44**, 3697 (1973)
- [65] R. Bullough and R.C. Newman, *Proc. R. Soc. A* **246**, 427 (1959)
- [66] F.R.N. Nabarro, *Theory of Crystal Dislocations*, Oxford 1967, Chapter 6.2 Dislocation Locking
- [67] E.R. Weber, U. Kaufmann, J. Windscheif and J. Schneider, *J. Appl. Phys.* **53** (3), 6140 (1982)
- [68] R. Fornari, C. Frigeri and R. Gleichmann, *J. Electron. Mater.* **18**, 185 (1989)
- [69] K. Terashima, S. Washizuka, J. Nishio, A. Okada, S. Yasuami and M. Watanabe, *Inst. Phys. Conf. No. 79*, 37 (1985)
- [70] H. Wenzl et al. private communication
- [71] P. Wurzinger, H. Oppolzer, P. Pongratz and P. Shalicky, *J. Cryst. Growth* **110**, 769 (1991)

- [72] C. Frigeri, O. Breitenstein, R. Fomari, R. Gleichmann, E. Gombia and R. Mosca, *Microsc. Semicond. Mater. Conf.*, Oxford, 1989
- [73] D.J. Stirland, P. Gall, M.R. Brozel, L. Breivik, G.M. Williams, A.G. Gillis and J.P. Fillard, *Inst. Phys. Conf. Ser.* **112**, 55 (1990)
- [74] F. Bartels, H.J. Clemens and W. Mönsh, *Physica* **117B & 118B**, 801 (1983)
- [75] A. Ourmazd, M. Scheffler, M. Heinemann, and J.L. Rouviere, *J. Mater. Educ.* **14**, 193 (1992)
- [76] J.K. Kung, W.G. Spitzer, *J. Appl. Phys.* **45** (10), 4477 (1974)
- [77] V. Swaminathan and S.M. Copley, *J. Appl. Phys.* **47** (10) 4405 (1976)
- [78] H. Ono and R.C. Newman, *J. Appl. Phys.* **66** (1), 141 (1989).
- [79] S.Y. Chiang and G.L. Pearson, *J. Appl. Phys.* **46a**, 2986 (1975)
- [80] T. Inada, Y. Otoki, K. Okata, S. Taharasako and S. Kuma, *J. Cryst. Growth* **96**, 327 (1989)
- [81] Y. Otoki, M. Watanabe, T. Inada and S. Kuma, *J. Cryst. Growth* **103**, 85 (1990)
- [82] E. Molva, Ph. Bunod, A. Chabli, A. Lombardot, S. Dubois and F. Bertin, *J. Cryst. Growth* **103**, 91 (1990)
- [83] C. Frigeri and J.L. Weyher, *J. Appl. Phys.* **65** (12) 4646 (1989)
- [84] J. Hornstra, *J. Phys. Chem. Solids* **5**, 129 (1958)
- [85] J.L. Weyher, J. van de Ven, *J. Cryst. Growth* **78**, 197 (1986)
- [86] K.H. Kuesters, B.C. Cooman and C.B. Carter, *Phil. Mag. A* **53**, 141 (1986)
- [87] I. Yonenaga and K. Sumino, *J. Cryst. Growth* **126**, 19 (1993)
- [88] J.L. Weyher, P.J. van der Wel, G. Frigero and C. Mucchino, 6th Conf. Semiinsulating III-V Mat., Toronto, Canada (1990), p. 161
- [89] K.A. Pandelisev, R.P. Bult and D. Fuschi, *ibid.* p. 167
- [90] C. Frigeri, *Proc. of Microsc. Semicond. Mater. Conf.*, Oxford (1987) p. 745
- [91] M.R. Brozel, *DRIP II*, 225 (1987)
- [92] J. Donecker, *phys. stat. sol. (a)* **127**, 275 (1991)
- [93] R.L. Barns, *J. Electronic Material* **18**, 703 (1989)
- [94] P. Franzosi and G. Salviati, *Mat. Chemistry and Physics* **9**, 321 (1983)
- [95] P. Paufler, G. Wagner, K. Grosse, *Cryst. Res. Technol.* **28**, 2 (1993) p. 199–207
- [96] M.P. Scott, *DRIP I*, 41 (1985)
- [97] A. Zrenner, F. Koch and K. Ploog, *Inst. Phys. Conf.* **91**, 171 (1987)
- [98] E.F. Schubert, T.H. Chiu, J.E. Cunningham, B. Tell and J.B. Stark, *J. Electron. Mater.* **17**, 527 (1988)
- [99] INSPEC, *The Institution of Electrical Engineers, Properties of Gallium Arsenide*, 2nd Ed., 1990, p. 347
- [100] T.H. Chin, J.E. Cunningham, B. Tell, E.F. Schubert, *J. Appl. Phys.* **64** (3), 1578–80 (1988)
- [101] E.F. Schubert, C.W. Tu, R.F. Kopf, J.M. Kuo, L.M. Lunardi, *Appl. Phys. Lett.* **54** (25), 2592–4 (1989)
- [102] R.B. Beall, J.B. Clegg, J.J. Harris, *Semicond. Sci. Technol.* **3** (6), 612–15 (1988)
- [103] D.G. Deppe, N. Holonyak, Jr., F.A. Sish, J.E. Baker, *Appl. Phys. Lett.* **50** (15), 998–1000 (1987)
- [104] J. Maguire, R. Murray, R.C. Newman, R.B. Beall, J.J. Harris, *Appl. Phys. Lett.* **50** (9), 516–18 (1987)
- [105] M.E. Greiner, J.F. Gibbons, *Appl. Phys. Lett.* **44** (8), 750–2 (1984)

- [106] L.J. Vieland, *J. Phys. Chem. Solids* **21**, 318 (1961)
- [107] G.R. Antell, *Solid-State Electron.* **8**, 943 (1965)
- [108] P.S. Dobson, P.F. Fewster, D.T.J. Hurle, P.W. Hutchinson, J.B. Mullins, B.W. Strangham and A.F.W. Willoughby, *Inst. Phys. Conf. Ser.* **45**, 163 (1979)
- [109] J.C. Brice, *Crystal Growth Processes*, Blackie & Son Ltd. (1986)
- [110] H. Meschede, *Diplomarbeit*, RWTH Aachen 1992
- [111] T. Figielski in *Defects in Crystals* (World Scientific, 1988) p. 379
- [112] A.F. Ponce, *Inst. Phys. Conf.* **87**, 154 (1988)
- [113] D.J. Stirland, *Int. Phys. Conf.* **117**, 327 (1991)
- [114] G.G. Kirkpatrick, R.T. Chen, D.E. Holmes, D.M. Asbeck, K.R. Elliot, R.D. Fairma and J.R. Oliver; *Semiconductors and Semimetals Vol. 20*, R.K. Willardson and A.C. Beer (Acad. Press, Orlando, FL 1984) p. 159
- [115] K. Yamada, H. Kohda, H. Nakanishi and K. Hoshikawa, *J. Cryst. Growth* **78**, 36 (1986)
- [116] H. Ono, *J. Cryst. Growth* **89**, 209 (1988)
- [117] J.L. Weyher, *Proc. 1984 Meeting on "Carratterizzazione Analitico-Strutturale di Materiali e Dispositivi per l'Elettronica a Stato Solido"* Eds. S. Carra, G. Ghezzi, P.G. Merli and C. Paovici (Techniografica, Parma 1984) p. 1
- [118] F.L. Vogel, *Acta Met.* **3**, 245 (1955)
- [119] H.P. Scott, S.S. Laderman and A.G. Elliot, *Appl. Phys. Lett* **47**, 12 (1985)
- [120] P. Kidd, D.J. Stirland and G.R. Booker, *Inst. Phys. Conf.* **117**, 357 (1991)
- [121] H. Klapper, *Progr. Crystal Growth and Charact.* **14**, 367 (1987)
- [122] W.A. Tiller, *The science of crystallization: macroscopic phenomena and defect generation*, Cambridge Univ. Res., p. 413
- [123] D.T.J. Hurle, *Sir Th. Frank 80th Birthday Tribute*, Ed. R.G. Chambers etc., Pubs: A. Hilger 1991, p. 188
- [124] S. Tohuo and A. Katsui, *J. Cryst. Growth* **74**, 362 (1986)
- [125] O. Pätzold, G. Irmer and J. Monecke, *Crystal Res. Technol.* **27**, K73 (1992)
- [126] C. Frigeri, O. Breitenstein, R. Fonari, R. Gleichmann, E. Gombia and R. Mosca, *Microsc. Semicond. Mater. Conf.*, Oxford (1998)
- [127] W. Zulehner, private communication

The first part of the document discusses the importance of maintaining accurate records of all transactions. It emphasizes that every entry should be supported by a valid receipt or invoice. This ensures transparency and allows for easy verification of the data.

In the second section, the author outlines the various methods used to collect and analyze the data. This includes both manual data entry and the use of specialized software tools. The goal is to ensure that the data is both accurate and easy to interpret.

The third part of the document provides a detailed breakdown of the results. It shows that there has been a significant increase in sales over the period covered by the report. This is attributed to several factors, including improved marketing strategies and better customer service.

Finally, the document concludes with a series of recommendations for future actions. These include continuing to invest in marketing, improving operational efficiency, and maintaining the high standards of data accuracy that have been established.

11/11/2023

11/11/2023

11/11/2023 11:11:11 AM

Jül-2939

Juli 1994

ISSN 0944-2952